This is to certify that the
dissertation entitled

ELECTRONIC STRUCTURE AND THERMOELECTRIC
PROPERTIES OF NARROW BAND GAP CHALCOGENIDES

presented by

DANIEL BILC

has been accepted towards fulfillment
of the requirements for the

Ph.D. degree in Physics and Astronomy

Subhendra D. Mahanti
Major Professor's Signature

05/31/05
Date

ELECTRONIC STRUCTURE AND THERMOELECTRIC PROPERTIES OF NARROW BAND GAP CHALCOGENIDES

By

Daniel Bilc

A DISSERTATION

Submitted to
Michigan State University
in partial fulfillment of the requirements
for the degree of

DOCTOR OF PHILOSOPHY

Department of Physics and Astronomy

2005

ABSTRACT

ELECTRONIC STRUCTURE AND THERMOELECTRIC PROPERTIES OF NARROW BAND GAP CHALCOGENIDES

By

Daniel Bilc

In recent years there have been a revival of interest in discovering and understanding the physical properties of novel thermoelectric (TE) systems with high figure of merit. These systems are primarily narrow band gap semiconductors. In this thesis, electronic structure calculations were carried out for several narrow band gap chalcogenide TE materials in order to understand their electronic and transport properties governing their TE characteristics. These calculations were performed within *ab initio* density functional theory (DFT) using full potential linearized augmented plane wave (FLAPW) method. Transport calculations were carried out using Boltzmann transport equations.

For the binary chalcogenides Bi_2Se_3 and Bi_2Te_3 I have studied the effect of quantum confinement (QC) created by the surfaces on their bulk electronic structure. In the presence of such confinement, surface states appear, which are a consequence of the strong influence of the interlayer bonding on the bulk electronic structure of these compounds. I find that in contrast to standard belief, there is an important covalent contribution to the interlayer bonding besides the Van der Waals contribution.

$(Bi_2Te_3)_m(Sb_2Te_3)_n$ superlattices (SL) show very good TE properties at room temperature. To see how the electronic structure of Bi_2Te_3 and Sb_2Te_3 are affected by the formation of SL, I have investigated the electronic properties of $(Bi_2Te_3)_m(Sb_2Te_3)_n$ SL

as compared to those of Bi_2Te_3 and Sb_2Te_3 bulk systems. We find that the formation of SL does not deteriorate the electronic transport properties along the cross plane direction.

Complex ternary $K_2Bi_8Se_{13}$ system shows great potential for superior TE performance. This compound forms in two distinct phases, α and β. The β-phase, which has two sites with K/Bi disorder, is a better TE. The calculations show that α-phase is an indirect band gap semiconductor. For the β-phase we find that the atoms at the "mixed sites" are very important in determining the electronic properties. The incorporation of the K/Bi mixed occupancy at the disordered sites is crucial for the semiconductor behavior. We also find a strong anisotropy in the hole and electron effective mass.

Complex quaternary $AgPb_mSbTe_{2+m}$ (LAST-m) systems are excellent high temperature TE. These systems form in the rocksalt structure similar to PbTe where Ag and Sb occupy Pb sites. There are clear experimental evidences that LAST-m systems exhibit microscopic inhomogeneities rich in Ag-Sb embedded into a PbTe matrix. Our calculations show that resonant states appear near the PbTe band gap. The common feature of all Ag-Sb arrangements is that they have a more enhanced density of states (DOS) near the gap as compared to PbTe. To see how these features in the DOS affect the transport properties I have carried out transport calculations in PbTe and LAST-m systems. The results for PbTe show that the temperature dependence of the effective mass m_d is very important in order to have good agreement with experiment. The LAST-m systems show an enhancement of the power factor ($S^2\sigma$) relative to PbTe. But this enhancement is not large enough to explain the experimentally observed *ZT*. This suggests that the reduction in the thermal conductivity caused by Ag-Sb nanostructures in PbTe matrix may be significant.

To my family and to Richi

ACKNOWLEDGMENTS

I would like to acknowledge the enormous support from my adviser, Professor S.D. Mahanti, and Professor M.G. Kanatzidis in Chemistry. I would like also to acknowledge Dr. Tim Hogan in Engineering for collaboration on the thermoelectricity project, Dr. S. Tessmer and Dr. S. Urazhdin for discussions and for providing the scanning tunneling microscopy experimental results. I would like to thank Dr. E. Quarez and Dr. K.F. Hsu in Chemistry for discussions on modeling the complex crystal structures. I would also like to acknowledge Professor P. Duxbury and Professor P. Danielewicz in Physics for the support as members of my committee.

Finally, I would like to greatly acknowledge funding form the Office of Naval Research (Contract No. N00014-02-1-0867 MURI program) and DARPA (Contract No. N00014-01-1-0728).

Table of Contents

List of Tables

List of Figures

Chapter 1

Introduction

Thermoelectricity is an old field, which was discovered back in 1821 by Seebeck. Unfortunately this field was obscured by Seebeck's own misjudgment trying to relate the appearance of magnetization as a result of an applied temperature gradient. For more than one century the field of thermoelectrics did not advance until the 1950s when the first revival took place. [33] During the 1950s the basic science of thermoelectricty became well established, the role of doped semiconductors as good thermoelectric materials was accepted, the thermoelectric material Bi_2Te_3 was discovered, and the thermoelectric industry was launched. Over the next three decades 1960-1990 the thermoelectrics industry grew slowly but continuously. [14] In the 1990s, a second revival occurred in the field of thermolelectrics, when new theoretical concepts were introduced and new materials using these concepts were synthesized. [14]

Thermoelectric materials can be used for both refrigeration or power generation. For refrigeration one maintains a temperature gradient using an applied electric current or, con-

versely for power generation an electric current is generated from an applied temperature gradient. The devices built with these thermoelectric materials have no moving parts, produce no waste products to be released into the environment, and are scalable to any size. The thermoelectric devices have been used in space missions, laboratory equipment, and medical applications, for which the cost and the efficiency were not as important as the energy availability, and the reliability. The problem using thermoelectric devices on a wide scale is that their coefficient of performance for refrigeration (efficiency for power generation) is much lower than that of current technologies. [13, 56, 93]

The performance of a thermoelectric device can be described by the dimensionless thermoelectric figure of merit, ZT:

$$ZT = \frac{S^2\sigma}{\kappa}T, \tag{1.1}$$

where S is the Seebeck coefficient (thermopower), σ is the electrical conductivity, κ is the thermal conductivity, and T is the operating temperature. There are two contributions to κ, κ_{ph} from phonons and κ_{el} from electrons. Over the three decades spanning 1960-1990, the highest values of ZT were found to be $\sim$1 in binary chalcogenides, specifically Bi_2Te_3, PbTe, Sb_2Te_3 and their alloys. These are doped narrow band-gap semiconductors having a large Seebeck coefficient and electrical conductivity but a low thermal conductivity. [35] To make thermoelectric devices competitive with the existing technologies for cooling and power generation, ZT values of 3-4 are required. [13, 56, 93] Since the quantities S, σ, and κ for conventional 3D systems are inter-related, it is very difficult to control these variables independently so that ZT values could be increased.

Several attempts have been made to improve *ZT* by making novel materials using concepts such as quantum confinement [27] (QC) and phonon glass electron crystal [86] (PGEC). Within the QC picture, first proposed by Hicks *et. al.* [27], new physical phenomena are introduced and new opportunities arise to independently vary S, σ, and κ as the dimensionality is decreased from 3D crystalline solids to 2D (quantum wells) , 1D (quantum wires), and 0D (quantum dots). Model calculations predict an increase in *ZT* for a two dimensional layer having thickness smaller than about 300Å (for example an idealized Bi_2Te_3-multiple quantum well structure) due to enhanced power factor PF ($PF=S^2\sigma$). Even larger power factor enhancement can occur in one-dimensional quantum wires. [14]

Harman *et. al.* have reported *ZT* values of 0.9 at 300K and 2.0 at 550K in $PbSe_{0.98}Te_{0.02}$/PbTe quantum dot structures . [25] They believe that the increase in the *ZT* values are due to QC effects, which enhance the power factor PF. However, no theoretical calculations have been performed for these quantum dot structures to support the QC picture and the enhancement in the *ZT* may also originate from a strong reduction of the phonon thermal conductivity κ_{ph}.

In contrast to the QC idea, within PGEC picture one uses superlattice (SL) structures consisting of two materials both having favorable S and σ (such that electronic properties are not affected by the SL structure), but reduces κ_{ph} by engineering the phonon band structure in a suitably chosen transport direction. *ZT* values of $\sim$2.4 and $\sim$1.4 have been achieved in p-type Bi_2Te_3/ Sb_2Te_3 and n-type Bi_2Te_3/$Bi_2Te_{2.83}Se_{0.17}$ SL thin films at 300K. [98] Other classes of systems which support the PGEC picture are skutterudites and clatharates. These systems have cage-like structures and contain weakly bonded atoms

called "rattlers", which have been studied to reduce the phonon thermal conductivity κ_{ph} without drastically affecting their thermopower S and electrical conductivity σ. A *ZT* value of ~1.35 was reported for the skutterudite $CeFe_{3.5}Co_{0.5}Sb_{12}$ at ~900K. [19]

A third approach where both the QC and PGEC ideas have been exploited to certain extent is to chemically synthesize new ternary and quaternary narrow band gap semiconductors containing Bi, Te, Se atoms with different arrangements of Bi-Te-Se blocks which are referred to as different quantum architectures. [36] These complex chalcogenides with their large unit cells contain also "rattlers" atoms. [35] Some examples of such systems are $BaBiTe_3$, $CsBi_4Te_6$, $AgPb_mSbTe_{2+m}$ (LAST-m) etc. In particular $CsBi_4Te_6$ [10] has been found to be the best bulk thermoelectric at low temperature (*ZT*~0.8 at 225K) and LAST-m systems have been found to be the best bulk thermoelectrics at high temperatures (*ZT*~1.2 for LAST-12 and ~2.2 for LAST-18 at 800K). [30]

Electronic structure calculations can serve an important role in determining which materials will prove useful for thermoelectric applications. The *ZT* values depend on band structure parameters such as the band gap, effective mass and its anisotropy, degeneracy of the band extrema, carrier mobility, and the total thermal conductivity (electron plus lattice) of the physical system. The importance of anisotropic effective mass was nicely brought out by Hicks and Dresselhaus [27] through a parameter *B* given by:

$$B = \frac{1}{3\pi^2}\left[\frac{2k_BT}{\hbar^2}\right]^{\frac{3}{2}}\left(\frac{m_e^3}{\lambda_{xx}\lambda_{yy}\lambda_{zz}}\right)^{\frac{1}{2}}\frac{\gamma k_BT\mu_{zz}}{e\kappa_{ph}} \tag{1.2}$$

$$\lambda_{ij} = \frac{m_e}{m_{ij}}; i,j = x,y,z \tag{1.3}$$

where λ_{xx}, λ_{yy} and λ_{zz} are the effective mass parameters along principal symmetry directions of a lattice (inversely proportional to the effective mass), m_e is the free electron mass, γ is the degeneracy of the electron or hole pockets, μ_{zz} is the mobility along the current flow (chosen to be the z-axis) which is proportional with λ_{zz}, k_B is the Boltzmann constant and κ_{ph} is the lattice thermal conductivity. *B* is a material parameter and for a fixed value of *B* one can maximize *ZT* by changing the carrier concentration. This optimized value of *ZT* increases monotonically with *B*. As can be seen from Eq. 1.2 the *B* factor in addition to depending on mobility and κ_{ph}, is directly proportional to the fraction $R=[\lambda_{zz}/(\lambda_{xx}\lambda_{yy})]^{1/2}$ which is a measure of the electronic structure anisotropy. A large value of R is necessary for large *ZT* in anisotropic systems.

In recent years *ab initio* electronic structure calculations using density functional theory (within local density or generalized gradient approximations, LDA [42] or GGA [70]) have been extremely successful in unravelling the electronic structure of many narrow band gap semiconductors with complex crystal structures. Examples are: skutterudites [65, 87], clatharates [7, 8], and ternary bismuth chalcogenide systems ($BaBiTe_3$ [50] and $CsBi_4Te_6$ [51]). In certain cases they have even been able to predict the band gaps and effective masses quantitatively in spite of the limitations of LDA and GGA. [2] Although the fundamental reason for this is not known, the subtle nature of the origin of gap formation (i.e. hybridization, spin-orbit interaction) in these compounds may be responsible for the above mentioned quantitative agreement. [50, 51] Even in systems where the quantitative predictions of LDA/GGA are not that good, one has been able to understand the physics of gap formation, the nature of bonding, and the parentage of states contributing to

the transport properties of these narrow band gap semiconductors. [52] It is clear that *ab initio* electronic structure calculations are able to provide great insight about the physical properties of complex systems.

In this thesis I have studied the electronic structure and electronic transport properties of simple (binary) and complex (ternary and quaternary) chalcogenide systems. Many electronic structure calculations have been performed previously for the binary chalcogenides Bi_2Te_3 [62, 50, 102, 49, 81], Bi_2Se_3 [62, 49], Sb_2Te_3 [92, 66], Sb_2Se_3 [82, 66], PbTe [67, 60, 97, 99, 1, 47], PbSe [67, 60, 97, 99, 1, 47], and PbS. [67, 97, 99, 47] Since ZT can be enhanced through QC and SL structures, I have investigated the effect of QC created by the surfaces on the electronic structure of layered Bi_2Se_3 and Bi_2Te_3 (the impact of interlayer bonding on the electronic properties). Although in $(Bi_2Te_3)_m(Sb_2Te_3)_n$ SL [98] the PGEC effect is primarily responsible for the increase in ZT, it is important to know how the electronic properties of Bi_2Te_3 and Sb_2Te_3 are affected by the formation of SL. To answer this problem, I have investigated the electronic properties of $(Bi_2Te_3)_m(Sb_2Te_3)_n$ SL as compared to those of Bi_2Te_3 and Sb_2Te_3 bulk systems. The ternary $K_2Bi_8Se_{13}$ system shows potential for superior thermoelectric performance. This compound forms in two distinct phases, α and β. The β-phase, which has several sites with mixed K/Bi occupancy is a better thermoelectric. It has been found that β phase is a much better thermoelectric. Therefore, to gain a deeper understanding of the electronic structure of the promising thermoelectric $\beta-K_2Bi_8Se_{13}$, to see how the difference in the crystal structures of α and β phases shows up in their electronic structures, and the role of K/Bi mixing, I have carried out detailed electronic structure calculations in both phases of these compounds. The qua-

ternary LAST-m systems are the best known high temperature bulk thermoelectrics. These systems form in the rocksalt structure similar to PbTe where Ag and Sb occupy Pb sites. There are clear experimental evidence that LAST-m systems are not solid solutions between the $AgSbTe_2$ and PbTe but they exhibit microscopic inhomogeneities rich in Ag-Sb embedded into a PbTe matrix. To see the effect of Ag-Sb microscopic arrangements on the electronic structure and transport properties I have performed electronic structure and transport calculations in these complex systems.

Chapter 2

Electronic Structure Calculations Using Density Functional Theory (DFT)

The basis of electronic structure calculations lies in the nature of electrons in a solid. Electrons interact through long range Coulomb forces which makes it very difficult to describe them as distinct entities. However, the electrons in solids do not act as "bare" particles, rather they are screened out by positively charged polarization clouds. The electron and screening cloud form a "quasiparticle" which weakly interact with other quasiparticles in the solid. The weak interaction between quasiparticles allows for an effective single particle approximation, particularly for low energy properties where they can be treated as acting in the mean field of the other quasiparticles. Such an approximation is valid in a large class of solids (metals, semiconductors, and insulators) but not in solids with strong electron-electron interactions and weak screening (magnetic insulators). Within a single particle approximation electronic structure calculations involve solving the single particle

Dirac equation. When relativistic effects are not significant as in many solid state systems, one solves a single particle Schrodinger equation.

2.1 Full Relativistic Single Particle Dirac Equation

In the single particle description, one has to solve the Dirac equation for an electron because the full relativistic effects applied to electronic structure are included in this equation. [43] The Dirac Hamiltonian is given by:

$$H_D = c\alpha \cdot \mathbf{p} + (\beta - 1)mc^2 + V(\mathbf{r}) \quad , \tag{2.1}$$

where α and β are 4×4 matrices expressed as:

$$\alpha = \begin{pmatrix} 0 & \sigma \\ \sigma & 0 \end{pmatrix} \quad , \tag{2.2}$$

$$\beta = \begin{pmatrix} I & 0 \\ 0 & -I \end{pmatrix} \quad , \tag{2.3}$$

with σ_x, σ_y, and σ_z being the Pauli spin matrices. $\mathbf{p}$ is the four component momentum, m is the bare electron mass, c is the speed of light and $V(\mathbf{r})$ is the effective single particle potential. The eigen vectors Ψ of the Dirac Hamiltonian can be written as four component spinors consisting of the two two-component spinors: large component Φ and small component χ.

$$\Psi = \begin{pmatrix} \Phi \\ \\ \chi \end{pmatrix} \quad . \tag{2.4}$$

This gives a set of coupled equations for Φ and χ:

$$c(\sigma \cdot \mathbf{p})\chi = (\epsilon - V)\Phi \quad , \tag{2.5}$$

$$c(\sigma \cdot \mathbf{p})\Phi = (\epsilon - V + 2mc^2)\chi \quad . \tag{2.6}$$

Solving for Φ the above two equations give the equation for the large component Φ:

$$\frac{1}{2m}(\sigma \cdot \mathbf{p}) \left(1 + \frac{\epsilon - V}{2mc^2}\right)^{-1} (\sigma \cdot \mathbf{p})\Phi + V\Phi = \epsilon\Phi \quad . \tag{2.7}$$

2.2 Scalar Relativistic Approximation

Eq. 2.7 is the exact Dirac equation. This equation serves as the basis for relativistic electronic structure calculations. [78, 32, 18] However, for valence electrons, where the relativistic effects are not usually strong, one can make the following approximation:

$$\left(1 + \frac{\epsilon - V}{2mc^2}\right)^{-1} \cong \left(1 - \frac{\epsilon - V}{2mc^2}\right) \quad , \tag{2.8}$$

and using the identities:

$$\mathbf{p}V = V\mathbf{p} - i\hbar\nabla V \quad , \tag{2.9}$$

$$(\sigma \cdot \nabla V)(\sigma \cdot \mathbf{p}) = (\nabla V \cdot \mathbf{p}) + i\sigma \cdot [\nabla, \mathbf{p}] \quad , \tag{2.10}$$

the Dirac Eq. 2.7 can be written as a linear second-order differential equation in Φ. This is given by:

$$\left[\left(1 - \frac{\epsilon - V}{2mc^2}\right)\frac{\mathbf{p}^2}{2m} + V\right]\Phi - \frac{\hbar^2}{4m^2c^2}(\nabla V \nabla \Phi) + \frac{\hbar^2}{4m^2c^2}\left(\sigma\left[\nabla V, \mathbf{p}\right]\Phi\right) = \epsilon\Phi \quad . \tag{2.11}$$

For a spherically symmetric potential $V(r)$ the Eq. 2.11 can be simplified further:

$$\left[\frac{\mathbf{p}^2}{2m} + V - \frac{\mathbf{p}^4}{8m^3c^2} - \frac{\hbar^2}{4m^2c^2}\frac{dV}{dr}\frac{\partial}{\partial r} + \frac{1}{2m^2c^2}\frac{dV}{dr}\frac{1}{r}(\mathbf{l}\cdot\mathbf{s})\right]\Phi = \epsilon\Phi \quad , \tag{2.12}$$

where the first two terms are the nonrelativistic Schroedinger Hamiltonian, the third is the mass velocity term, the fourth is the Darwin term, and the last term is the spin-orbit interaction (SOI). Due to the SOI term, **j=l+s** is the good quantum number. The four-component function is now written as:

$$\Psi = \begin{pmatrix} \Phi \\ \\ \chi \end{pmatrix} = \begin{pmatrix} g(r)\mathcal{Y}_{jl}^{jz} \\ \\ if(r)\mathcal{Y}_{jl'}^{jz} \end{pmatrix} \quad , \tag{2.13}$$

where g and f are the radial functions, $Y_{jl}^{j_z}$ is the r-independent eigen function of j^2, j_z, l^2, and s^2 formed by the combination of the Pauli spinor with the spherical harmonics.

In practice one first solves Eq. 2.12 without the last term [43], which reduces to:

$$\left[\frac{\mathbf{p}^2}{2m} + V - \frac{\mathbf{p}^4}{8m^3c^2} - \frac{\hbar^2}{4m^2c^2}\frac{dV}{dr}\frac{\partial}{\partial r}\right]\tilde{\Phi} = \epsilon\tilde{\Phi} \quad . \tag{2.14}$$

Eq. 2.14 is called the scalar relativistic Schroedinger equation. Since there is no spin-orbit coupling in Eq. 2.14, **l** and **s** are still good quantum numbers. However, the spin-orbit effects are important, especially for heavier elements. The four-component wave function $\tilde{\Psi}$ is expressed in terms of radial functions ($\tilde{f}(r)$ and $\tilde{g}(r)$) and spherical harmonics, Y_{lm} as:

$$\tilde{\Psi} = \begin{pmatrix} \tilde{\Phi} \\ \\ \tilde{\chi} \end{pmatrix} = \begin{pmatrix} \tilde{g}(r)Y_{lm} \\ \\ -i\tilde{f}(r)Y_{lm} \end{pmatrix} \chi_s \quad . \tag{2.15}$$

The scalar relativistic Eq. 2.14 is solved with this choice of $\tilde{\Phi}$. The functions $\tilde{\Psi}$ are not eigen functions of the Dirac Hamiltonian H_D and their deviation from eigen functions is used to define the spin-orbit Hamiltonian H_{so}:

$$H_D\tilde{\Psi} = \epsilon\tilde{\Psi} + H_{so}\tilde{\Psi} \quad . \tag{2.16}$$

In the basis set of functions $\tilde{\Phi}$, H_{so} has the form:

$$H_{so} = \frac{\hbar}{2Mc^2}\frac{dV}{dr}\frac{1}{r}\begin{pmatrix} l\cdot s & 0 \\ 0 & 0 \end{pmatrix} \quad , \tag{2.17}$$

where M is the relativistic mass given by:

$$M = m + \frac{\epsilon - V}{2c^2} \quad . \tag{2.18}$$

To include SOI, one method is to double the entire basis set to accommodate H_{so}. This approach is usually computationally expensive. The second variational method is an alternative, which does not require the doubling of basis set. The spin up and down states are considered separately using the eigenvectors of the scalar relativistic calculation for a finite number of states near the Fermi energy. This reduces the number of basis sets involved in the calculation in the presence of SOI. The spin up and down states can be expressed as:

$$\tilde{\Psi}^{\uparrow} = \begin{pmatrix} g^{\uparrow}(r)Y_{lm} \\ -if^{\uparrow}(r)Y_{lm} \end{pmatrix}\chi_{\uparrow} \quad , \chi_{\uparrow} = \begin{pmatrix} 1 \\ 0 \end{pmatrix} \quad , \tag{2.19}$$

$$\tilde{\Psi}^{\downarrow} = \begin{pmatrix} g^{\downarrow}(r)Y_{lm} \\ -if^{\downarrow}(r)Y_{lm} \end{pmatrix}\chi_{\downarrow} \quad , \chi_{\downarrow} = \begin{pmatrix} 0 \\ 1 \end{pmatrix} \quad . \tag{2.20}$$

The states given in Eqs. 2.19, and 2.20 are used as new basis set for the expansion of the wave function Φ in Eq. 2.12. The total Hamiltonian including SOI can be solved with less computational effort since the number of $\tilde{\Psi}^{\uparrow}$ and $\tilde{\Psi}^{\downarrow}$ states are usually much less than in

the original eigenvalue problem. [43, 85].

2.3 Density Functional Theory (DFT)

A major theoretical and computational advance in electronic structure of solids was made by Hohenberg and Kohn [29] and later by Kohn and Sham [42] with the advent of density functional theory. This theory states that the ground state electronic properties of a solid are determined solely through its electronic density $\rho(\vec{r})$. Therein the key quantity is $\rho(\vec{r})$ in terms of which the total energy is:

$$E_{tot}\left(\rho(\vec{r})\right) = T_s\left(\rho(\vec{r})\right) + E_{ee}\left(\rho(\vec{r})\right) + E_{Ne}\left(\rho(\vec{r})\right) + E_{xc}\left(\rho(\vec{r})\right) + E_{NN} \quad , \qquad (2.21)$$

where T_s is the kinetic energy of the noninteracting particles having the same density $\rho(\vec{r})$, E_{ee} is the electron-electron repulsive Coulomb energy, E_{Ne} is the nuclear-electron attractive Coulomb energy, E_{xc} is the exchange-correlation energy and E_{NN} is the repulsive Coulomb energy of the fixed nuclei.

In local density approximation (LDA) [34], E_{xc} is expressed as a function of the local exchange-correlation energy density μ_{xc}:

$$E_{xc}^{LDA} = \int \mu_{xc}\left(\rho(\vec{r})\right)\rho(\vec{r})d^3\vec{r} \quad . \qquad (2.22)$$

This approximation is generalized for both the spin densities $\rho^{\uparrow}(\vec{r})$ and $\rho^{\downarrow}(\vec{r})$ in local spin density approximation (LSDA):

$$E_{xc}^{LSDA} = \int \mu_{xc}\left(\rho^{\uparrow}(\vec{r}), \rho^{\downarrow}(\vec{r})\right)\left[\rho^{\uparrow}(\vec{r}) + \rho^{\downarrow}(\vec{r})\right] d^3\vec{r} \quad . \tag{2.23}$$

Recent progress has been made going beyond LSDA by adding gradient terms of the electron density to E_{xc}. This has led to generalized gradient approximation (GGA) [71, 70]:

$$E_{xc}^{GGA} = \int \mu_{xc}\left(\rho^{\uparrow}(\vec{r}), \nabla\rho^{\uparrow}(\vec{r}), \rho^{\downarrow}(\vec{r}), \nabla\rho^{\downarrow}(\vec{r})\right)\left[\rho^{\uparrow}(\vec{r}) + \rho^{\downarrow}(\vec{r})\right] d^3\vec{r} \quad . \tag{2.24}$$

To solve the energy minimization problem Kohn and Sham proposed a method in which T_s is given by:

$$T_s = \sum_i^N \int \psi_i^{\star}(\vec{r})\left(-\frac{\hbar^2}{2m}\nabla^2\right)\psi_i(\vec{r})d^3\vec{r} \quad , \tag{2.25}$$

where the sum goes over the all occupied orbitals of an N-electron system. Minimization of the total energy E_{tot} with respect to charge density $\rho(\vec{r})$ leads to the Kohn-Sham single particle equations:

$$\left[-\frac{\hbar^2}{2m}\nabla^2 + V_C(\vec{r}) + V_{xc}\right]\psi_i(\vec{r}) = \epsilon_i\psi_i(\vec{r}) \quad , \tag{2.26}$$

where V_C is the classical Coulomb potential and V_{xc} is the exchange-correlation potential. V_C+V_{xc}=V_{eff} is an effective single particle potential. The single particle Kohn-Sham Eqs. 2.26 have to be solved self consistently with the condition:

$$\rho(\vec{r}) = \sum_{i}^{N} \mid \psi_i(\vec{r}) \mid^2 \quad . \tag{2.27}$$

For a generalization of Kohn-Sham equations to fully relativistic systems see [74, 73, 55].

It should be emphasized that the total energy E_{tot}:

$$E_{tot} \neq \sum_{i} \epsilon_i^{KS} \quad , \tag{2.28}$$

where ϵ_i^{KS} are the Kohn-Sham single particle eigen values. The corrections have to be made. [24]

ϵ_i^{KS} are not the true quasiparticle states seen in experiment. However, for broad band systems they provide a very good description except for band gaps and effective masses. [2]

2.4 Method of Calculation

Electronic structure calculations were performed using the self-consistent full-potential linearized augmented plane wave method (FLAPW) [85] within DFT [29, 42], using GGA of Perdew, Burke and Ernzerhof [70] for the exchange and correlation potential. Since most of the systems of our interest contain the heavy atom Bi relativistic effects are very important. Relativistic effects are marginally important for Sb and Te, and not important for Se. The way such effects are included in the electronic structure code used to obtain the electronic structure (WIEN97 and WIEN2K programs) [6] is discussed very briefly.

The core states are treated in a fully relativistic way (i.e. solving the Dirac Eq.2.7). [80] The valence and local orbitals, which are defined within the atomic spheres are first ob-

tained within scalar relativistic approximation (see section 2.2). This approximation does not include SOI but takes into account the effects of mass-velocity and Darwin corrections. [80] In the absence of SOI spin up and spin down eigen functions separate. In the presence of SOI, the spin up and spin down eigen functions mix and this is incorporated in a rather efficient way using a second variational method. [38, 54] In this method one takes advantage of the fact that SOI is usually small and only a smaller subset of basis functions obtained without SOI are used to obtain the eigen values and eigen functions in the presence of SOI.

An important parameter that goes into the electronic structure calculation in the FLAPW method is the value of the atomic radius of each component. For different multi-component systems the values of the atomic radii were chosen differently. In some cases the values of atomic radii were taken to be the same for all the atoms, and this value is chosen to fill the space between atoms. In other cases different values were chosen for different atoms. The number of the reciprocal $\vec{k}$ points used in the calculations of the self-consistent charge density were taken to be in the range 18 to 30. The number of plane waves used in the interstitial region is characterized by a parameter $RK_{max}=R_{ml}*K_{max}$, where R_{ml} is the smallest muffin tin radius and K_{max} is the maximum plane wave vector. Typically RK_{max} is chosen between 7 to 9, and for our calculations it was taken to be 8. Convergence of the self-consistent iterations was performed within 0.0001 Ry with a cutoff of -6.0 Ry between the valence and the core states.

Chapter 3

Surface States in Binary Semiconductors Bi_2Se_3 and Bi_2Te_3

3.1 General Introduction for Bi_2Se_3 and Bi_2Te_3

Among the best known bulk materials for room and high temperature thermoelectric applications are binary chalcogenides, specifically Bi_2Te_3, Sb_2Te_3, PbTe and their alloys. Bi_2Te_3, Bi_2Se_3, Sb_2Te_3, and Sb_2Se_3 are layered materials consisting of multiple "quintuple layers", with each "quintuple layer" containing five alternating atomic planes (see section 3.2). Inside a "quintuple layer" the interaction between atoms is of covalent type with covalent intralayer bonds, whereas the interaction between the "quintuple layers" is conventionally termed as Van der Waals-type with Van der Waals interlayer bonds. [91, 102] Because of such weak interlayer bonding, the effect of the surface on the electronic structure is expected to be small. Such an assumption is made in most interpretations of the

surface probes (e.g. electron tunneling and photoemission) of layered compounds. However, an increased attention has been recently given to the impact of the weak interlayer bonding on both bulk and surface electronic properties of layered materials. [102, 37] In a recent publication, [96] we have shown that surface electronic structure plays an important role in the observation of near-surface defects in Bi_2Se_3.

3.2 Crystal Structure of Bi_2Se_3 and Bi_2Te_3

The crystal structure of both Bi_2Te_3 and Bi_2Se_3 is rhombohedral with space group $D^5_{3d}(R\bar{3}m)$. [100] It can be represented as a stack of hexagonally arranged atomic planes, each consisting of only one type of atom. Five atomic planes are stacked in a close-packed *fcc* fashion in order (Fig. 3.1) Te1(Se1)-Bi-Te2(Se2)-Bi-Te1(Se1), in a quintuple layer. The proximity of the surface breaks the equivalence of the Te1(Se1) positions in a layer, so the Te3(Se3) notation was used for the third Te(Se) atomic plane from the surface. The hexagonal unit cell, shown in Fig. 3.1, spans three quintuple layers and contains 15 atoms.

To model the experimental scanning tunneling spectroscopy (STS) data (to be discussed in section 3.4, calculations in a slab geometry, [90] modeling the surface were performed. For band structure calculations for bulk Bi_2Se_3 and Bi_2Te_3, the hexagonal unit cell consisting of 3 quintuple layers was used, whereas to model the surface a repeating slab geometry was used, with slabs consisting of 3 to 12 quintuple layers separated by an increased distance **d**, as compared to the bulk crystal structure ($\sim$0.35nm). The calculated band structures did not exhibit significant variation with the separation larger than 0.4–0.5nm between the slabs; therefore the slab separation of **d**=0.7 nm was found sufficient for modeling the

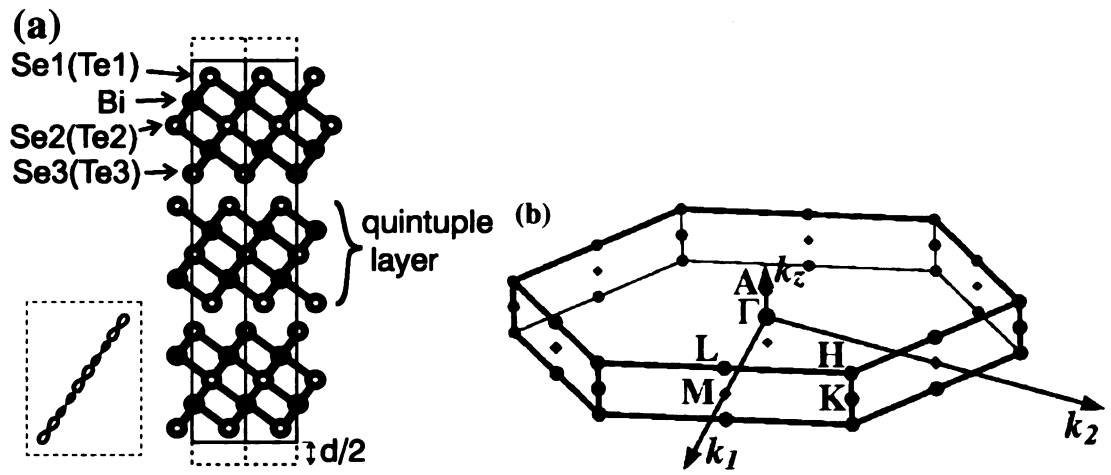

Figure 3.1: (a) Bi_2Se_3 (Bi_2Te_3) structure viewed parallel to the layers. 2x1x1 hexagonal unit cell is shown with a solid line. The unit cell used for slab calculations (for a 3-layer slab) is shown in dash. In a dashed frame one of the $pp\sigma$ bonded chains is plotted. (b) Hexagonal Brillouin zone of Bi_2Se_3 (Bi_2Te_3).

surface.

3.3 Electronic Structure of Bulk and Slab (to Model the Surface)

In Fig. 3.2 the calculated band structures of Bi_2Se_3 and Bi_2Te_3 both in the bulk and slab geometries are shown. Since the bulk unit cell spans 3 layers, the 3-layer thick slab geometry used in Fig. 3.2 gives the same number of bands as in the bulk calculations, which is convenient for a direct comparison. It can be presumed that due to the weak interlayer bonding the electronic states of the middle layer in a slab are close to the bulk states, and thus a 3-layer slab might be sufficient for modeling the surface electronic structure of a bulk sample. However, it is shown below that this conclusion can be accepted with certain limitations. Calculations of the bulk band structure, shown in Fig. 3.2(a),(c), yield a direct

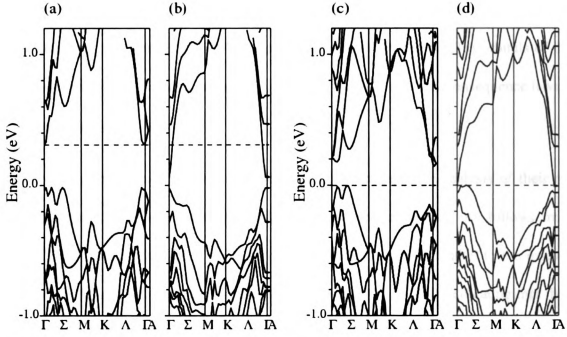

Figure 3.2: Calculated band structure: (a) bulk Bi_2Se_3, (b) 3-layer slab of Bi_2Se_3,(c) bulk Bi_2Te_3, (d) 3-layer slab of Bi_2Te_3. The experimental Fermi energies are shown as dashed lines; zero energy corresponds to the top of the valence band.

band gap of 0.3eV in Bi_2Se_3 and an indirect gap of 0.14eV in Bi_2Te_3 with degenerate valence band maximum. These are similar to the earlier calculations. [50, 91, 62, 102] Our calculations do not reproduce the six-fold degeneracy of the conduction band minimum seen experimentally in Bi_2Te_3. [39, 84, 40] This problem has been encountered in a number of earlier calculations. [50, 91, 62] However our more recent calculations reproduce the 6-fold degeneracy of the conduction band minimum when the $p_{1/2}$ relativistic local orbitals are incorporated in the LAPW basis. [59] Comparing the calculations of the bulk band structure (Fig. 3.2(a),(c)) with the slab (Fig. 3.2(b)(d)), one finds that there is a significant effect of the reduced interlayer bonding between the slabs both in Bi_2Se_3 and Bi_2Te_3. The most notable differences are lowering of the bulk conduction band states into the gap and a drastic restructuring of the valence band, with most of the high valence band (HVB)

states associated with surface Se1 (Te1) atoms lowered in energy as compared to the bulk band structure. The remaining HVB states are dominated by the Se (Te) orbitals of the atoms located in the quintuple layers away from the surface, and as a consequence have a small amplitude at the surface.

The nature of the surface states can be elucidated through the analysis of their orbital character in real space and dispersion in the reciprocal space. As follows from Fig. 3.2(b)(d), the in-gap states are highly dispersive in the plane parallel to the quintuple layers (ΓM and ΓK directions in the Brillouin zone, Fig. 3.1(b)), indicating that they originate from the strong in-plane hybridization of the surface atoms. Analysis of the orbital character of the in-gap states shows that they are dominated by the two atomic layers closest to the surface: Se1 and Bi in Bi_2Se_3, and Te1 and Bi in Bi_2Te_3. However, there are significant contributions from all the other atoms in the surface quintuple layer. The in-gap states do not exhibit dispersion in the direction perpendicular to the quintuple layers (the ΓA direction), which is consistent with the negligible interaction between the slabs. The analysis of the orbital character of the HVB for the bulk Bi_2Se_3(Bi_2Te_3) shows that they are dominated by Se(Te) states, which are antibonding in the sense of interlayer coupling. At the surface, the energy separation between the Se(Te) bonding and antibonding states is reduced as a consequence of the increase in energy of the valence band (VB) bonding states and decrease in energy of the HVB antibonding states. The lowering of the HVB at the surface is a robust effect which has been qualitatively understood in terms of a simple one-dimensional tight-bonding model. [96]

To follow the evolution of the electronic structure with the distance from the surface,

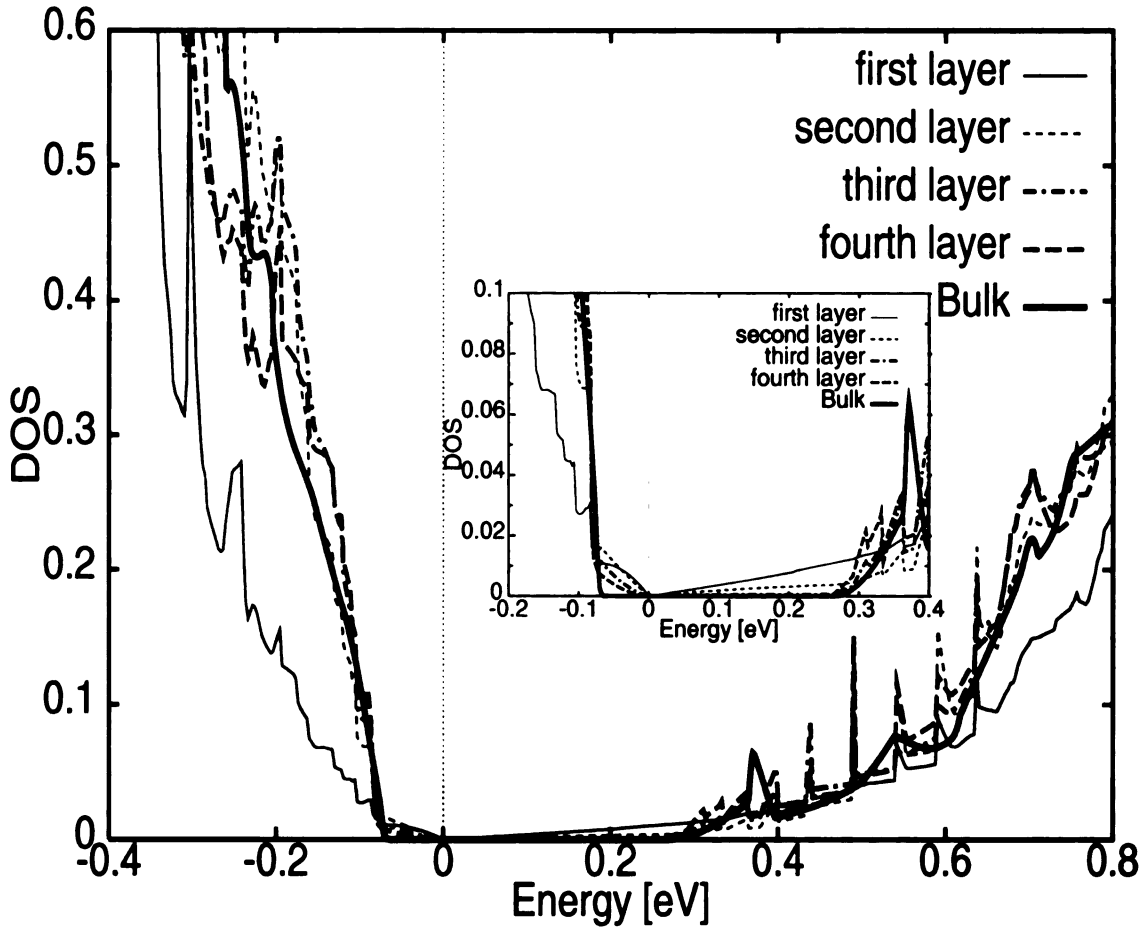

Figure 3.3: Partial DOS of Se1 in Bi_2Se_3 for various positions of the quintuple layers with respect to the surface in a 12-slab geometry.

in Fig. 3.3 we show the partial "atomic " density of states (DOS) of Se1 atoms for various quintuple layers as a function of their position relative to the surface in a 12 slab-geometry calculation. The in-gap states associated with the lowering of the bulk conduction band into the gap (the states between 0eV and 0.25eV) are mostly present in the first quintuple layer. There are also in-gap states associated with the restructuring of the HVB (the states between -0.07eV and 0eV, insert in Fig. 3.3). The bulk HVB states (below -0.07eV) are almost recovered by the Se1 at the second layer from the surface, while the surface Se1

contribution to the states near the top of the valence band (between -0.07eV and -0.3eV) is dramatically suppressed. This is consistent with the antibonding (in the sense of interlayer bonding) nature of the states near the top of the valence band, as found e.g. in tight-binding calculations. [96]

The sharp peaks, which are present in the DOS calculations in slab geometry, occur due to the saddle points, where the bands have no dispersion along the ΓA direction. According to Gofron and Dabrowsky, [23] such saddle points, which they called "extended" Van Hove singularities, yield a power law divergence in DOS. These are artifacts due to the approximation of the bulk sample terminated with a surface by a finite thickness slab. The number of peaks increases with the slab thickness due to the folding of the Brillouin zone along the ΓA direction, while their weight decreases. In the limit of an infinite slab, the DOS should become smooth. The deviation from the bulk DOS in the case of Se1 atoms located at second, third and fourth layer are particularly strong in the HVB between -0.3eV and -0.1eV and are due to these "extended" Van Hove singularities.

To see the effects of structural relaxation on the electronic states, we performed volume optimization (i.e. optimization with respect to scaling of the lattice constants), and force minimization for individual atomic sites up to 0.2mRy/nm for the 3-slab geometry. Optimization decreases the volume by 1% for Bi_2Se_3 and increases it by 4% for Bi_2Te_3. All the optimized bond distances, except for the interlayer bonds, are within 1 to 2.5% of their bulk values for both Bi_2Se_3 and Bi_2Te_3. The interlayer distances within the slabs increase by 7.9% and 5.5% in Bi_2Se_3 and Bi_2Te_3, respectively. The relaxation does not significantly change the effects of the surface on the electronic band structure. In Bi_2Se_3,

the lowering of the surface conduction band into the bulk gap is reduced from ~0.25eV in unrelaxed calculation to ~0.17eV after relaxation is performed, while the other changes in the band structure are insignificant. In Bi_2Te_3, the only significant effect of the relaxation is a slight upward shift of the highest valence band by ~0.03eV. The small effect of structural relaxation reflects the overall weakness of interlayer bonds, i.e. the relatively small structural perturbation introduced by the presence of the surface. However, locally the effect of surface is important, it gives rise to surface states.

3.4 Comparison with Scanning Tunneling Microscopy (STM) Results

Scanning tunneling microscopy (STM) is an imaging method with diverse possibilities for real space imaging on a scale which extends to atomic dimensions. [4] The underlying physical basis of the STM is electron tunneling. Electron tunneling occurs between two conductors (electrodes) separated by a sufficiently thin insulating layer or, in physical terms, potential barrier. The tunneling current I is a measure of the overlap of the wave functions of the two electrodes. Therefore, I is a function of the electrode separation and the nature of the states involved. In practice, the electronic images are obtained by recording dI/dV or dI/ds while scanning and controlling the tunneling distance s by keeping the average current constant, where V is the voltage across tunneling barrier. Because of the usually close relation of the tip-sample spacing at constant I with the topography, of dI/dV with the local density of states, and of dI/ds with the local barrier height (work function),

associated images are often referred to as topographical or STM images, spectroscopic or scanning tunneling spectroscopy (STS) images, and work-function profiles, respectively. The experimental results presented here were acquired by Sergei Urazhdin. [95]

An experimental STM topographic image of Bi_2Se_3 (0,0,1) surface is shown in Fig. 3.4(a). Fig. 3.4(b) shows a simulated topographic image of Bi_2Se_3 surface. It was obtained from theoretical calculations in a slab geometry by integrating the energy projected charge density in a range of 0.7 eV from the top of the valence band, at a plane 2.4 Å above the surface Se atoms. In both the experimental and simulated topographic images, the highest corrugations are identified with the surface Se atoms. Both images Fig. 3.4(a,b) reflect the 6-fold rotational symmetry of the surface Se plane. However, this 6-fold symmetry is broken by the Bi atoms in the underlying atomic plane. Bi atoms are positioned in the center of every other triangle formed by the neighboring surface Se atoms, lowering the rotational symmetry to 3-fold. In the simulated image (Fig. 3.4(b)), the darkest spots between Se atoms correspond to positions which are not occupied by Bi in the second atomic plane, while positions occupied by Bi yield less contrast. The experimental image Fig. 3.4(a) are interpreted similarly. The slight discrepancy between the shapes of the Se atomic corrugations is, in terms of the Fourier components of the topographic images, due to the higher harmonics, which are not manifested in the experiment.

The STS conductance spectrum gives information about local DOS. To simulate the experimental differential conductance spectra, the electronic charge density was calculated as a function of energy, $\rho(\vec{r},E)$, at a point located at 2.35 Å above the surface Se atom. This was done by calculating $\rho(\vec{r},E)$ for different values of E within an energy mesh of 20meV

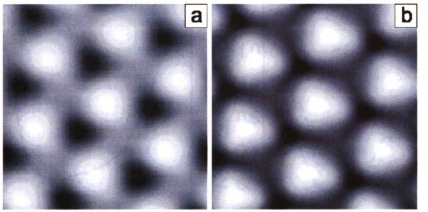

Figure 3.4: (a) 1.3×1.3 nm topographic image of Bi_2Se_3 surface acquired at a bias voltage -0.7 V. Black to white scale is 30 pm. Autocorrelation was used to enhance the image. (b) Calculated topography of Bi_2Se_3 at a bias voltage of -0.7 V.

and then averaging over five energy intervals. The theoretical conductance spectra was then obtained by multiplying $\rho(\vec{r}$,E) by a scale factor to give an overall fit to the experiment. To simulate the conductance spectra a very dense mesh of 961 irreducible $\vec{k}$ points in the k_z=0 plane of the Brillouin zone was required and in order to reduce the computational time we used the 3 slab-geometry (instead of 12 slab-geometry) to model the surface. The calculated and experimental conductance spectra of Bi_2Se_3 and Bi_2Te_3 are given in Fig. 3.5. The theoretical values were shifted in order to match the Fermi energies. The experimental conductance spectra show a finite DOS in the gap and a suppressed conduction in the HVB energy range. The calculated conductance spectra clearly show finite in-gap density of states in both Bi_2Se_3 and Bi_2Te_3. The overall agreement in Bi_2Se_3 is quite remarkable, while for Bi_2Te_3 the agreement is not as good.

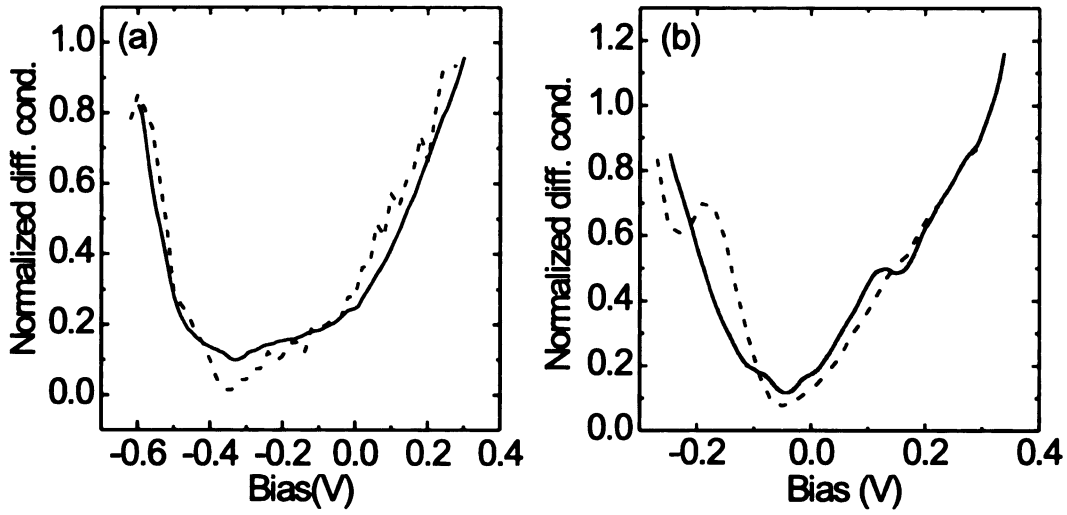

Figure 3.5: (a) Solid lines: near-gap tunneling differential conductance dI/dV_B spectrum of Bi_2Se_3, acquired directly with a lock-in detection technique at a temperature of 4.2 K. Dashed lines: theoretical curves, calculated for a 3 slab-geometry. The curves are normalized by the differential conductance at $V_B = 0.3$V. (b) Same as (a), for Bi_2Te_3.

3.5 Summary

Surface states appear in our theoretical calculations, in agreement with STS observations. Our calculations show that the surface states extend into the first quintuple layer with a decay length of about 1nm. These surface effects are complimentary to the strong influence of the inter(quintuple) layer bonding on the bulk electronic structure of these compounds, rendering the intuitive picture of layers weakly bonded with Van der Waals-type interaction inadequate. There is an important covalent contribution to the inter(quintuple) layer bonding. This can also be seen from the incomplete two-dimensional nature of Fermi surface in Bi_2Te_3, which reveals that the interlayer bonding is not only of Van der Waals-type (with a two-dimensional nature of Fermi surface), but is also covalent. [102] Our electronic structure calculations suggest that applications of low-dimensional (quantum confinement) narrow gap semiconductor structures [27] for thermoelectric devices where interface effects

play an important role cannot rely on the assumption that bulk-like electronic properties persist in low-dimensional structures.

Chapter 4

Electronic Structure of $(Bi_2Te_3)_m(Sb_2Te_3)_n$ Superlattice (SL)

4.1 General introduction for $(Bi_2Te_3)_m(Sb_2Te_3)_n$ SL

Following the phonon glass electron crystal (PGEC) concept to improve the efficiency of a thermoelectric material, great efforts have been made to synthesize SL systems with low temperature growth techniques such as molecular beam epitaxy (MBE) and chemical vapor deposition (CVD). As discussed in Chapter 1 according to PGEC concept, a high ZT value could be obtained in SL systems by introducing phonon scattering at the interface of SL systems and reducing κ_{ph}, provided one does not reduce the power factor PF ($S^2\sigma$) significantly.

$(Bi_2Te_3)_m(Sb_2Te_3)_n$ SL structures grown by chemical vapor deposition were found to be very good thermoelectric materials by Venkatasubramanian et al. [98], where room

temperature *ZT* values of ~2.4 and ~1.4 have been obtained in p-type Bi_2Te_3/Sb_2Te_3 and n-type $Bi_2Te_3/Bi_2Te_{2.83}Se_{0.17}$ SL thin films respectively. Unlike Bi_2Te_3 alloy systems where the charge and energy transport take place in planes parallel to the Van der Waals layers (defined as in-plane), in these SL systems charge transport takes place in a direction normal to this plane (defined as the cross-plane). For certain values of m and n, one finds a dramatic change in thermal conductivity which leads to an increased value of *ZT*. A fundamental question is how SL structures affect the electronic properties. Experimental value of the mobility anisotropy μ_{cp}/μ_{ip} was found to depend on the superlattice period and values of m and n. In Fig. 4.1, μ_{cp}/μ_{ip} is shown as functions of the thickness d of the Bi_2Te_3 and Sb_2Te_3 atomic layers. One "quintuple layer" (see section 4.2) consist of five atomic layers and has a thickness of ~10Å for both Bi_2Te_3 and Sb_2Te_3. In order to understand how band gap and effective mass anisotropy depend on these quantities I have carried out electronic structure calculations in bulk Bi_2Te_3 and Sb_2Te_3 and three SL systems, m=n=1 (11), m=1, n=2 (12), and m=2, n=4 (24).

4.2 Model Structures and Geometry optimizations for $(Bi_2Te_3)_m(Sb_2Te_3)_n$ SL

The SL structures consist of multiple "quintuple layer" of Bi_2Te_3 and Sb_2Te_3, with each "quintuple layer" containing 2 Bi/Sb and 3 Te atomic layers. As has been discussed in section 3.2 the crystal structure of Bi_2Te_3 and Sb_2Te_3 can be described in hexagonal symmetry with (P-3m1) space group and contains three "quintuple layers". Since experimental deter-

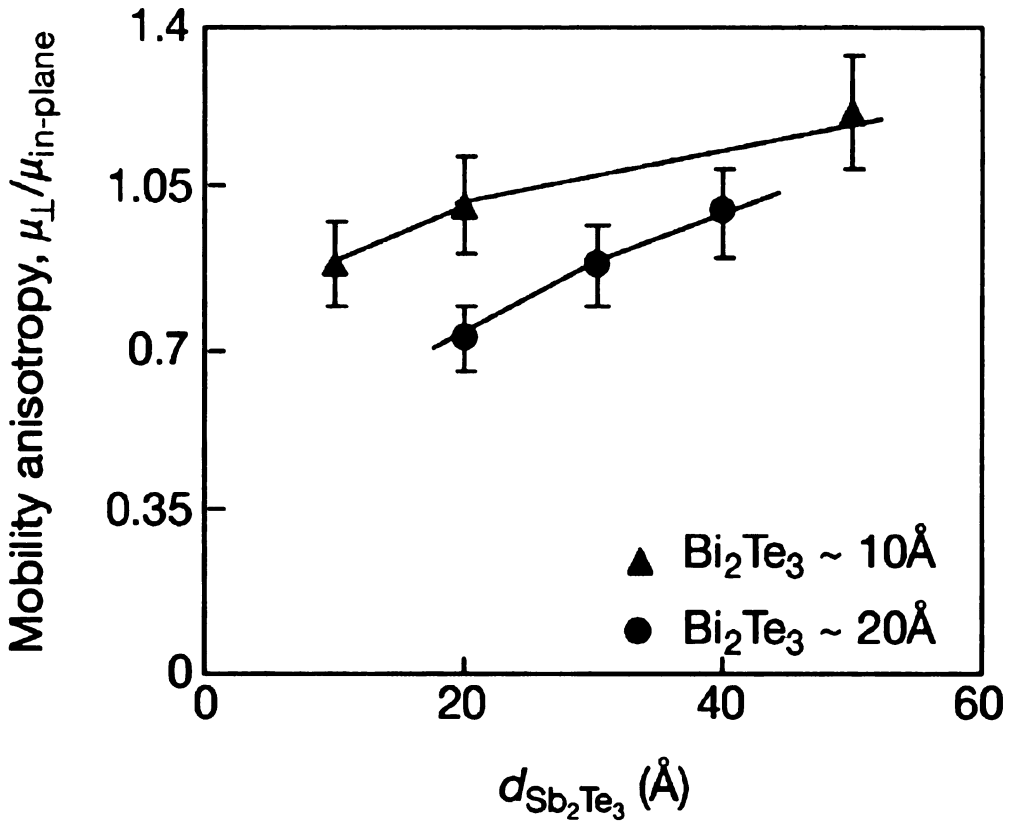

Figure 4.1: Hole mobility anisotropy in $(Bi_2Te_3)_m(Sb_2Te_3)_n$ SL. [98]

minations of the structures of $(Bi_2Te_3)_m(Sb_2Te_3)_n$ SL are not available, one has to assume some starting structures for electronic structure calculations. For (11) $Bi_2Te_3)_1(Sb_2Te_3)_1$ SL, a hexagonal structure with (P3m1) space group symmetry was used, with each unit cell containing one Bi_2Te_3 layer and one Sb_2Te_3 layer (Fig. 4.2(a)). The inversion symmetry of the bulk systems can not be preserved in this structure because there are only two "quintuple layers" in a unit cell. The (12) $Bi_2Te_3)_1(Sb_2Te_3)_2$ SL on the other hand has the same space group symmetry (P-3m1) as the bulk and the inversion symmetry is preserved (Fig. 4.2(b)).

The initial lattice parameters were taken as averages of bulk Bi_2Te_3 and Sb_2Te_3 lattice

parameters, which are $a_{(11)} = b_{(11)} = (a_B + a_S)/2$, $c_{(11)} = (c_B + c_S)/2$ for the (11) SL, $a_{(12)} = b_{(12)} = (a_B + a_S)/2$, $c_{(12)} = (c_B + 2c_S)/3$ for the (12) SL, and $a_{(24)} = a_{(12)}$, $c_{(24)} = 2c_{(12)}$ for the (24) SL (Fig. 4.2(c)). Here (a_B, c_B) and (a_S, c_S) are the lattice parameters of bulk Bi_2Te_3 and Sb_2Te_3 respectively. For each SL structure, the initial atomic coordinates in the "quintuple layers" are assumed to take the same fractions as in the bulk Sb_2Te_3. In bulk Bi_2Te_3 and Sb_2Te_3 two different types of Te atoms exist. The Te atom lying in the Van der Waals gap and bonded to one layer of Bi(Sb) atoms and one layer of Te atoms is Te1, and the Te atom which is bonded to two layers of Bi(Sb) atoms is Te2. So in the initial structure, the Bi-Te1 and Bi-Te2 bond lengths are assumed equal to the Sb-Te1 and Sb-Te2 bond lengths respectively. The SL geometries were then optimized starting from the initial lattice structures. As a first step, global lattice parameter optimizations (volume and c/a ratio) are performed, and then the internal atomic coordinates are relaxed until the forces on the atoms are below 1.0 mRy/a.u. = 0.0136 eV/Å.

For bulk Bi_2Te_3 and Sb_2Te_3, only volume optimizations were performed. The values of optimal volume V_{opt} correspond to 4% and 6% increase compared to the experimental values V_{exp} for Bi_2Te_3 and Sb_2Te_3 respectively. The internal atomic coordinates are then relaxed while keeping V_{opt} and $(c/a)_{opt}$ ratios fixed. The fractional changes of the atomic positions from their initial values are found to be rather small. The starting values (which are the experimental values) of the Te1-Bi, Te2-Bi, and Te1-Te1 bond lengths in Bi_2Te_3 are 3.117Å, 3.227Å, and 3.572Å respectively. The volume optimization increases these values to 3.158Å, 3.269Å, and 3.619Å. In Sb_2Te_3, the starting values of the Te1-Sb, Te2-Sb, and Te1-Te1 bond lengths are 2.974Å, 3.168Å, and 3.75Å, whereas the corresponding

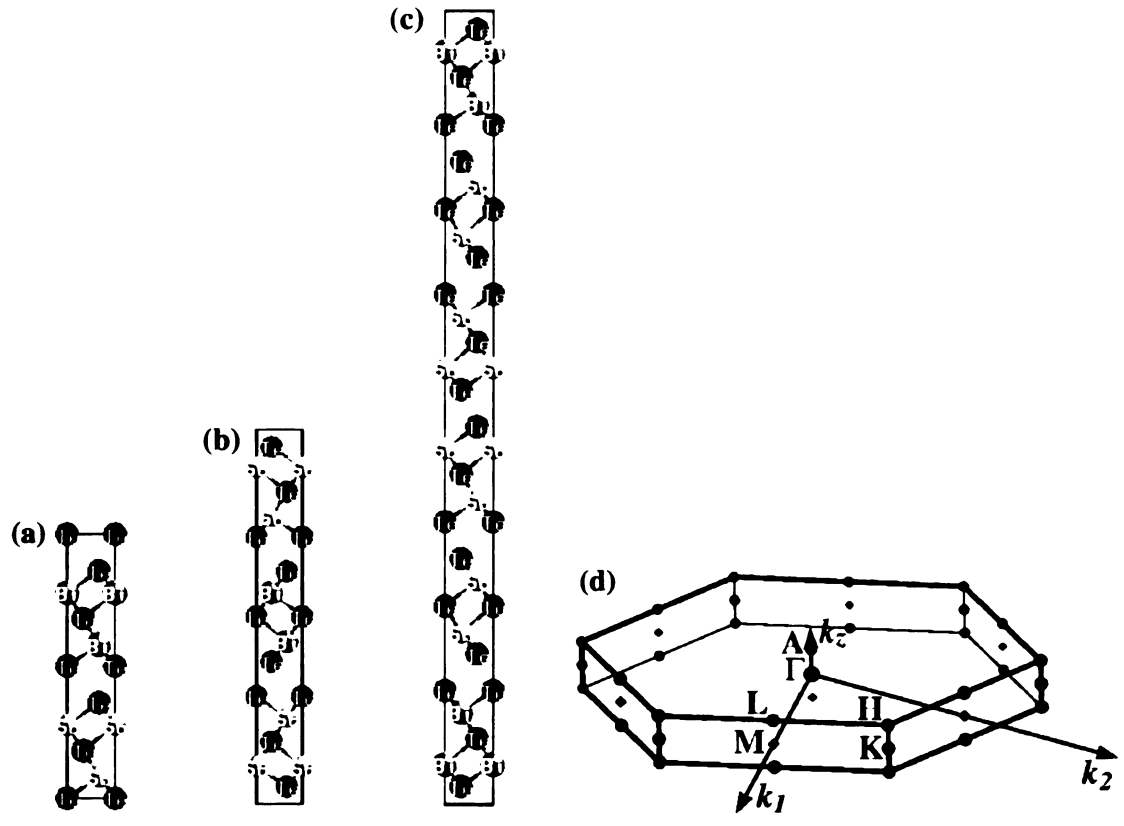

Figure 4.2: Models for $(Bi_2Te_3)_m(Sb_2Te_3)_n$ SL structures of (a) (11), (b) (12), and (c) (24). Hexagonal Brillowin zone (d).

values after volume optimization are 3.032Å, 3.23Å, 3.823Å. The effect of relaxation is to increase all the bond lengths; the amount of increase range from 0.04-0.07Å, the largest relaxation takes place for Te1-Te1 bond length in Sb_2Te_3.

For the (11) SL, V_{opt} and $(c/a)_{opt}$ ratio are 6.95% and 1.0% larger than their initial values. For the (12) SL, the V_{opt} and $(c/a)_{opt}$ ratio are 6.0% and 0.5% larger than the initial ones. The volume increase for the SL are found to be larger than in the bulk Sb_2Te_3 and Bi_2Te_3, indicating more relaxation effects for SL. In (11)SL after volume and internal (atomic) optimizations the Te1-Sb, Te1-Bi, Te2-Sb, Te2-Bi and Te1-Te1 bond lengths are 3.039Å, 3.072Å, 3.196Å, 3.278Å, and 3.979Å, whereas the corresponding values for

(12)SL are 3.04Å, 3.081Å, 3.202Å, 3.274Å, and 3.9Å. There is very good agreement between the bond lengths of the (11) and (12)SL after optimizations. As expected there are differences between bulk and SL structure bond lengths with the largest difference of ~0.08Å.

4.3 Electronic Structure of $(Bi_2Te_3)_m(Sb_2Te_3)_n$SL

Electronic transport properties of doped semiconductors depend sensitively on the nature of energy states which are close to the chemical potential (~0.2eV above and below the chemical potential). Therefore the details of the band structure (positions of the band extrema, degeneracy of local minima and maxima and dispersion of the bands) near the energy gap are very important in electronic transport. The valence band maximum (VBM) in bulk Bi_2Te_3, bulk Sb_2Te_3 and (11), (12) SL is six-fold degenerate and is located in the MΓA plane, but the position of VBM in this plane and the energy dispersion near VBM are different in bulk and SL systems (Fig. 4.3). Along ΓK direction the valence band of (11)SL has an energy dispersion which is very different than that of bulk Bi_2Te_3 and Sb_2Te_3, with a second VBM which may also contribute to transport. This suggests that by creating $(Bi_2Te_3)_m(Sb_2Te_3)_n$ SL one can not only engineer the hole effective mass and hole mobility anisotropy of the bulk Bi_2Te_3 and Sb_2Te_3 without changing the degeneracy factor, but also can introduce additional near by energy maxima (local) which can contribute to transport.

The conduction band minimum (CBM) in bulk Bi_2Te_3 before volume optimization is six-fold degenerate, being located in the MΓA plane. It is necessary to include relativistic

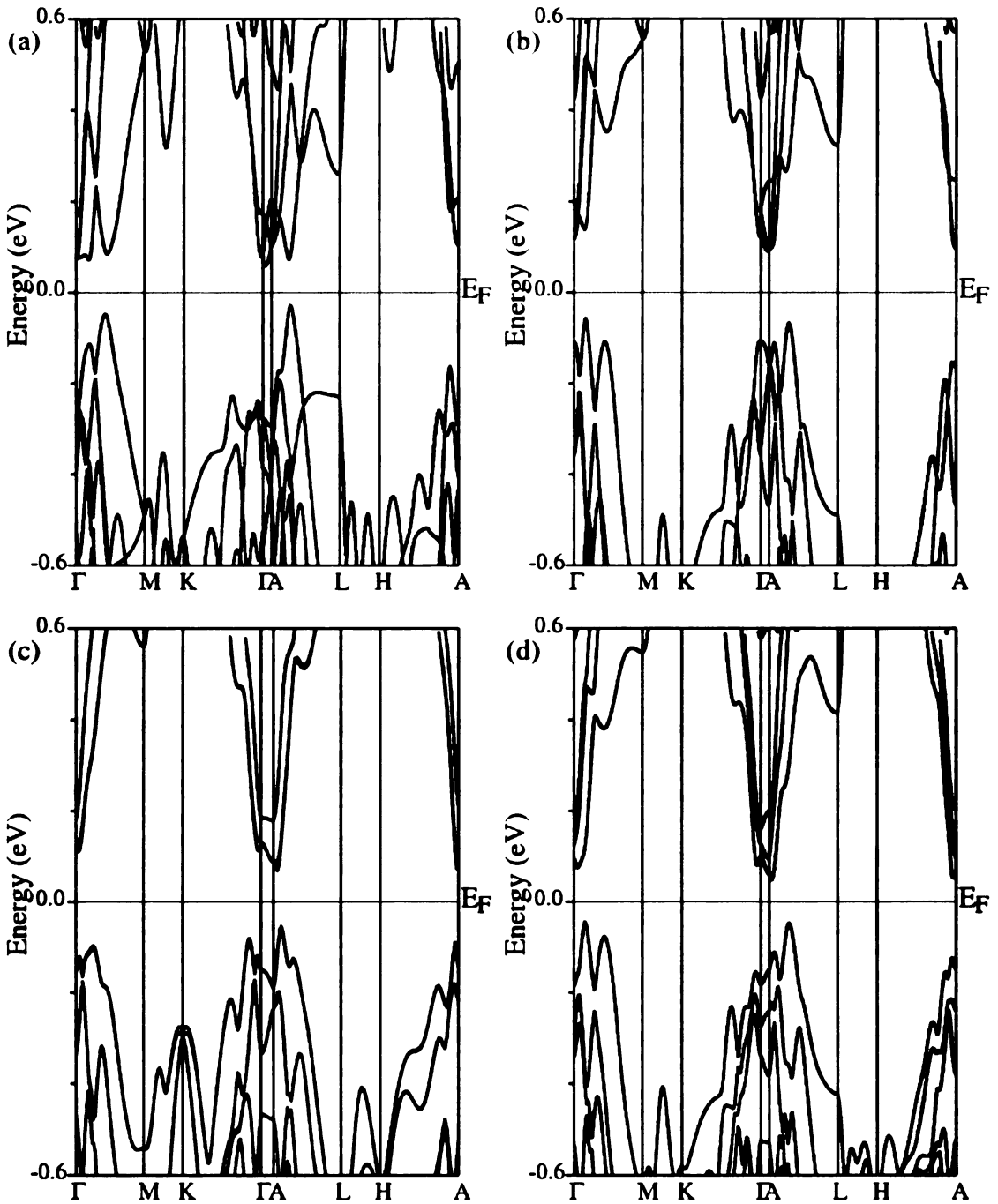

Figure 4.3: Band structure of (a) bulk Bi_2Te_3, (b) bulk Sb_2Te_3, (c) (11) SL, and (d) (12) SL.

$p_{1/2}$ local orbitals to get this minimum. [48] However after volume optimization this minimum is shifted up in energy and a new CBM appears along the ΓA direction and is two-fold degenerate (Fig. 4.3(a)). According to the Haas-van Alphen experiments, both VBM and CBM in Bi_2Te_3 are six-fold degenerate, [39, 84, 40]. It has proved to be extremely difficult to reproduce the six-fold degeneracy of the CBM because the details of the electronic structure seem to be extremely sensitive to the calculation procedure, and only two published result has been able to reproduce the six-fold degeneracy of CBM under restricted conditions. [102, 48] The CBM in Sb_2Te_3 is located along the ΓA direction and is two-fold degenerate (Fig. 4.3(b)), whereas the CBM in both (11) and (12) SL is located in the MΓA plane with six-fold degeneracy (Fig. 4.3(c),(d)). We were not able to find Haas-van Alphen experiments for Sb_2Te_3, in order to compare with our theoretical results. Large degeneracy factors significantly enhance the thermopower for a given concentration since the concentration for each electron or hole pocked is reduced and the thermopower increases with decreasing concentration. [57] The dispersions of the energy bands near CBM in both the SL are very similar, suggesting that the electron effective mass and electron mobility anisotropy may not be too sensitive to the detail characteristics of $(Bi_2Te_3)_m(Sb_2Te_3)_n$ SL systems.

4.4 Effective Masses in Bluk Bi_2Te_3, Sb_2Te_3 and $(Bi_2Te_3)_m(Sb_2Te_3)_n$ SL

The carrier effective masses, which determine the transport properties and the B factor (see Eq. 1.2), were calculated after obtaining the VBM and CBM positions in the MΓA plane of the Brillouin zone. This plane is one of the three reflection planes, which in real space coincides with yz plane where z-axis is the trigonal axis and y is the bisectrix axis. The cross section of electron and hole pockets in yz plane are ellipses whose major axes make an angle θ with the y-axis. Therefore the energies near the band extrema can be fitted using the Eq. 4.1:

$$\frac{2m_e}{\hbar^2}\epsilon_{\vec{k}} = \frac{m_e}{m_{xx}}k_x^2 + \frac{m_e}{m_{yy}}k_y^2 + \frac{m_e}{m_{zz}}k_z^2 + \frac{m_e}{m_{yz}}k_y k_z \tag{4.1}$$

where m_{ii} are the effective masses, k_i is the magnitude of the reciprocal space vector along the i-th orthogonal direction (i=x,y,z) and m_e is the free electron mass. The cross term m_e/m_{yz} is smaller than m_e/m_{yy} and m_e/m_{zz} for bulk Bi_2Te_3 and Sb_2Te_3. We did not calculate this term since we are interested only in the effective mass along the orthogonal directions. Since the energy band gaps are larger than 0.1eV, we expect Eq. 4.1 to give a reasonable estimation of the effective mass near the band extrema. The hole effective masses for bulk Bi_2Te_3, Sb_2Te_3 and SL before and after volume optimizations are given in Table 4.1. The effect of the volume optimizations is to increase the hole effective masses by no more than 0.1% in Bi_2Te_3 and 0.2% in Sb_2Te_3. The effect of the global and internal optimizations on the (11)SL is to increase the effective masses by ~0.4% (except for m_{yy}

which is decreased by $\sim$0.7%), whereas for the (12)SL, the effective masses increase by 0.4-0.5%. As expected, the effects of the relaxations on the (11) and (12)SL are more important than in the bulk Bi_2Te_3 and Sb_2Te_3, because for the SL we started from average structures for the SL. The values of the direct and indirect energy gaps are also shown in Table 4.1. The theoretical values of the energy gaps for bulk systems are smaller than those given by experiments due to the GGA(LDA) problem of underestimating the gap values. [2] The value of the indirect gap in Bi_2Te_3 is $\sim$0.06eV and the corresponding experimental value is 0.15eV, whereas in Sb_2Te_3 the indirect gap is $\sim$0.12eV and the corresponding experimental value is 0.3eV. The values of the indirect gap in (11), (12), and (24)SL are $\sim$0.06, $\sim$0.07, and $\sim$0.03 respectively. Although band gaps have not been experimentally measured in SL systems, we expect the experimental band gaps to be a factor of 2 larger than our calculated values within GGA. For Bi_2Te_3 the experimental hole effective masses are also given for comparison. [39, 40] The main discrepancy is for m_{xx}, the theoretical value is a factor of 2 smaller than experiment.

To estimate the carrier mobility ratio and compare with experiment [98], a simplified assumption is made, namely the relaxation time is assumed to be isotropic. The carrier mobility ratio in this case is equal to the ratio of the inverse effective masses. We define the anisotropy of cross-plane mobility to in-plane mobility as:

$$\frac{\mu_{cp}}{\mu_{ip}} = \frac{\frac{1}{m_{zz}}}{\frac{1}{2}(\frac{1}{m_{xx}} + \frac{1}{m_{yy}})} \tag{4.2}$$

The results of mobility anisotropy ratio for the VBM are also given in Table 4.1. The calculated values of the mobility ratio for Bi_2Te_3 and Sb_2Te_3 obtained after volume relaxation

Table 4.1: Valence band maximum VBM hole effective masses and mobility anisotropy.

	$\frac{m_{xx}}{m_e}$	$\frac{m_{yy}}{m_e}$	$\frac{m_{zz}}{m_e}$	$\frac{\mu_{cp}}{\mu_{ip}}$	$\frac{\mu_{cp}}{\mu_{ip}}$ exp.	**Direct gap(eV)**	**Indirect gap(eV)**
Bi_2Te_3	0.016	0.173	0.117	0.25		0.124	0.059
Bi_2Te_3 global optimized	0.016	0.189	0.128	0.23		0.122	0.059
Bi_2Te_3 exp. [39, 40]	0.031	0.208	0.111	0.49	0.33 [12]	0.22 [91]	0.15 [91]
Sb_2Te_3	0.036	0.094	0.067	0.78		0.134	0.091
Sb_2Te_3 global optimized	0.041	0.112	0.082	0.73		0.178	0.119
Sb_2Te_3 exp.	—	—	—		0.5 [31]		0.3 [5]
(11)SL	0.06	0.177	0.074	1.21			0.083
(11)SL global optimized	0.059	0.142	0.092	0.91			0.083
(11)SL internally optimized	0.085	0.106	0.104	0.91	0.88 [98]		0.056
(12)SL	0.029	0.106	0.074	0.62			0.027
(12)SL global optimized	0.039	0.129	0.094	0.64			0.045
(12)SL internally optimized	0.042	0.148	0.11	0.6	1.02 [98]		0.067
(24)SL	0.031	0.112	0.061	0.8	0.98 [98]		0.026

are 0.23 and 0.73, whereas the measured experimental values are 0.33 and 0.5 respectively. For the (11), (12), and (24)SL the calculated values are 0.91, 0.6, and 0.8 and the corresponding measured values are 0.88, 1.02, and 0.98. The differences in the calculated and measured experimental values may be because of the errors in values of the effective masses given by GGA calculations or also to the simplified assumption of the isotropic relaxation time used to obtain Eq. 4.2.

The results for the CBM are given in Table 4.2. As in the case of the VBM the effect of the lattice relaxation is to increase the electron effective mass. The volume optimization

Table 4.2: Conduction band minimum CBM electron effective masses and mobility anisotropy.

	$\frac{m_{xx}}{m_e}$	$\frac{m_{yy}}{m_e}$	$\frac{m_{zz}}{m_e}$	$\frac{\mu_{cp}}{\mu_{ip}}$	$\frac{\mu_{cp}}{\mu_{ip}}$ exp.	**Direct gap(eV)**	**Indirect gap(eV)**
Bi_2Te_3	0.017	0.153	0.143	0.21		0.116	0.059
Bi_2Te_3 global optimized	0.017	0.167	0.145	0.21		0.108	0.059
Bi_2Te_3 exp. [39, 40]	0.021	0.169	0.105	0.36	0.29 [44]	0.22 [91]	0.15 [91]
Sb_2Te_3	0.145	0.436	0.287	0.76			0.091
Sb_2Te_3 global optimized	0.148	0.53	0.354	0.65			0.119
Sb_2Te_3 exp.	—	—	—				0.3 [5]
(11)SL	0.067	0.105	0.337	0.24			0.083
(11)SL global optimized	0.132	0.119	0.471	0.27			0.083
(11)SL internally optimized	0.238	0.138	0.662	0.26			0.056
(12)SL	0.08	0.108	0.34	0.27		0.116	0.027
(12)SL global optimized	0.082	0.119	0.479	0.2		0.121	0.045
(12)SL internally optimized	0.119	0.143	0.512	0.25		0.166	0.067
(24)SL	0.474	0.431	6.27	0.07			0.026

increases the electron effective masses in Bi_2Te_3 and Sb_2Te_3 by no more than 0.1% and 0.2% respectively. The maximum increase in the values of the effective masses introduced by global and internal optimizations in the (11) and (12)SL are 2.6% and 0.5% respectively. The calculated values for the mobility ratio in Bi_2Te_3 and Sb_2Te_3 are 0.21 and 0.65, whereas in the (11) and (12)SL these values are 0.26 and 0.25. As anticipated from the band structure results (conduction band energy dispersion), in contrast to the hole mobility, the electron mobility ratio is less sensitive to different $(Bi_2Te_3)_m(Sb_2Te_3)_n$ SL.

4.5 Summary

Electronic structure calculations in different SL's show that both VBM and CBM are six-fold degenerate. This large degeneracy significantly increases the figure of merit *ZT*. [57] The effect of lattice relaxation is to increase the values of the effective masses and energy gaps. The calculated values of the hole mobility ratio μ_{cp}/μ_{ip} in the SL are in good agreement with the measured experimental values. [98] The values for (11) and (24)SL are close to unity and they are higher than those of the bulk Bi_2Te_3 and Sb_2Te_3. Our calculations show that the hole mobility ratio is very sensitive to the different types of SL, suggesting that the valence band can be engineered through $(Bi_2Te_3)_m(Sb_2Te_3)_n$ SL structures. On the other hand, the values of the electron mobility ratio in SL are in between the values of the bulk Bi_2Te_3 and Sb_2Te_3 and they are less sensitive to the different types of SL, suggesting that electron mobility ratio may not be engineered very easily through $(Bi_2Te_3)_m(Sb_2Te_3)_n$ SL structures. Our calculations indicate that the formation of SL structures does not deteriorate the electronic contribution to ZT (compared to bulk). Thus the large values of observed *ZT* come from reduced phonon thermal conductivity.

Chapter 5

Electronic Structure of Complex Ternary System $K_2Bi_8Se_{13}$

5.1 General Introduction for $K_2Bi_8Se_{13}$

In the previous chapter, I discussed the idea of constructing superlattices of different periods to enhance the thermoelectric figure of merit *ZT*. Another approach to increase *ZT*, which has been very successful, is to chemically synthesize new complex (ternary and quaternary) narrow band gap semiconductors containing Bi, Te, Se atoms with different arrangements of Bi-Te-Se blocks referred as quantum architectures. These complex chalcogenides with their large unit cells containing weakly bonded atoms called "rattlers", have been studied to reduce the phonon thermal conductivity κ_{ph} without drastically affecting their power factor PF ($S^2\sigma$). [35]

The *ZT* values of a thermoelectric material increase monotonically with the dimension-

less parameter B described in Chapter 1 and given in Eq. 1.3. B is directly proportional to the anisotropy factor $R=[\lambda_{zz}/(\lambda_{xx}\lambda_{yy})]^{1/2}$, of the effective mass parameters and to the degeneracy γ of the electron or hole pockets. These have to be maximized in order to have high B values and consequently high ZT. In a solid it is very difficult to maximize both the degeneracy γ and R, because γ can have high values in systems with high symmetries (i.e. cubic, hexagonal), whereas R can be maximized in systems with low symmetries (i.e. triclinic, monoclinic). Several new ternary compounds with low symmetry have been synthesized with a view to increase ZT. One such compound is $CsBi_4Te_6$ which is the best known thermoelectric for T<200K. [10]

Another promising complex chalcogenide with low symmetry is $K_2Bi_8Se_{13}$, where one tries to achieve large R, has been synthesized recently and its thermoelectric properties have been investigated. [9] This compound occurs in two distinct phases denoted as $\alpha-K_2Bi_8Se_{13}$ and $\beta-K_2Bi_8Se_{13}$. These two phases represent an example where similar buildings blocks combine to give compounds with the same stoichiometry but different architectures. Whereas the α-phase is a wide band gap semiconductor (band gap $\sim$0.76eV) and not a good thermoelectric, the β-phase is a narrow gap semiconductor and shows great promise for room and high temperature thermoelectric. One of the fascinating characteristics of the complex Bi-chalcogen systems is that they are either charge compensated (Bi is 3+ and X=Se/Te are 2-) or contain electron or hole-doped Bi/Te frameworks. However the systems are highly inhomogeneous with regards to the local Bi-X, Bi-Bi, and X-X bondings (can be covalent, ionic or van der Waals). This feature shows up directly in their crystal structures and local coordination. For example in $BaBiTe_3$ we have covalent Te-Te

bonds [11] and in $CsBi_4Te_6$ we have covalent Bi-Bi bonds. [10] The latter is in fact quite unusual for Bi-chalcogen systems. The differences in local bonding and coordination from one atom to another in the unit cell give rise to dramatic differences in the nature of the states near the top of the valence band and bottom of the conductions bands, states responsible for charge and energy transport in thermoelectric materials. As a result these complex Bi-chalcogen systems show a wide range of thermoelectric behavior. [10, 11] Electronic structure calculations in $CsBi_4Te_6$ and $BaBiTe_3$ have been performed earlier by Larson *et. al.*. In this thesis I focus on $K_2Bi_8Se_{13}$, trying to understand the difference in electronic structure of the α- and β- phases.

5.2 Crystal Structure of $K_2Bi_8Se_{13}$

$K_2Bi_8Se_{13}$ forms in two distinct phases, $\alpha-K_2Bi_8Se_{13}$ (triclinic with space group P-1) and $\beta-K_2Bi_8Se_{13}$ (monoclinic with space group P 2_1/m). [9] The α-phase contains Bi_2Te_3-, CdI_2- and Sb_2Se_3-type rod fragments parallel to the c-axis (Fig. 5.1) whereas the β-phase possesses an architecture made up of Bi_2Te_3-, CdI_2-, and NaCl-type rod fragments (Fig. 5.2). The CdI_2-type and Bi_2Te_3-type rods in α- and β- phases are arranged side by side to form layers perpendicular to the y-axis with tunnels filled along the c-axis with K^+ cations. Whereas in the β-phase the NaCl-type rod fragments connect the layers to build a 3-dimensional framework, in the α-phase the small Sb_2Se_3-type rod fragments make a weaker connection between the layers. The inclusion of alkali atoms stabilizes the covalent bonding in the Bi-chalcogen framework. The width of the Bi_2Te_3- and NaCl-type rods in the β-phase is three Bi polyhedra, while the width of CdI_2-type rod is only two Bi

polyhedra. The dimensions of these building blocks define the structural characteristics of each structure type in these materials. Overall, the β-phase is slightly more dense than the α-phase, because in the latter 25% of the Bi atoms are found in a trigonal pyramidal geometry, while in the former all Bi atoms are in an octahedral or greater coordination geometry. [9]

The α-phase has no structural disorder. On the other hand the β-phase has two sites with very similar coordination environment, which have K/Bi disorder. The Bi8/K3 site (in the Bi_2Te_3-block) contains 62% Bi and 38% K while the K1/Bi9 site (in the NaCl-block) contains 38% Bi and 62% K (see Fig. 5.2). Recent better refinement gives 50%/50% occupancy for these two mixed sites. The high coordinate disordered Bi/K atoms and CdI_2-type channels serve to stitch the fragments together. Since Bi^{3+} and K^+ have similar sizes, this similarity in the coordination environment of the Bi8/K3 and K1/Bi9 sites explains the disorder between Bi and K atoms. Due to the K/Bi disorder the experimental positions of the atoms at the mixed sites determined by X-ray powder diffraction are some average positions making the atomic distance of K1-Se9 (2.85Å) and K3-Se4 (2.84Å) too short as compared to the atomic distances between K2-Se sites (where there is no disorder) ranging from 3.28-3.71Å. [9] This large difference is due to the fact that when Bi is present at the disordered site it will move closer to the Se4 and Se9 atoms thereby making the average distance between the disordered site and the Se shorter. Consequently there will be local relaxations of the K^+ ions at the disordered sites.

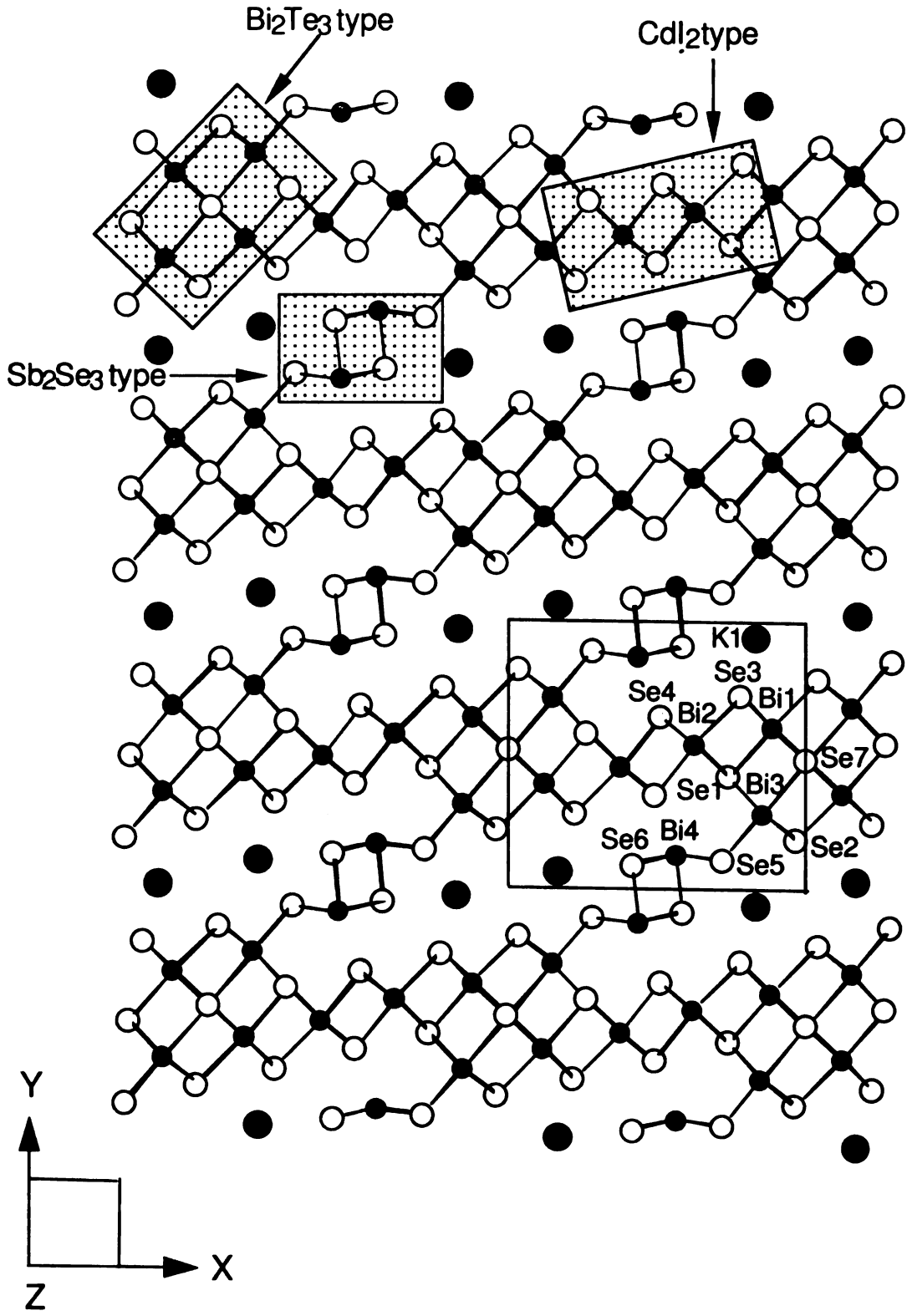

Figure 5.1: Projection of the crystal structure of $\alpha-K_2Bi_8Se_{13}$ viewed down the c-axis (z-axis). Bi_2Te_3-, CdI_2- and Sb_2Se_3- building blocks in the structure are highlighted by the shaded areas.

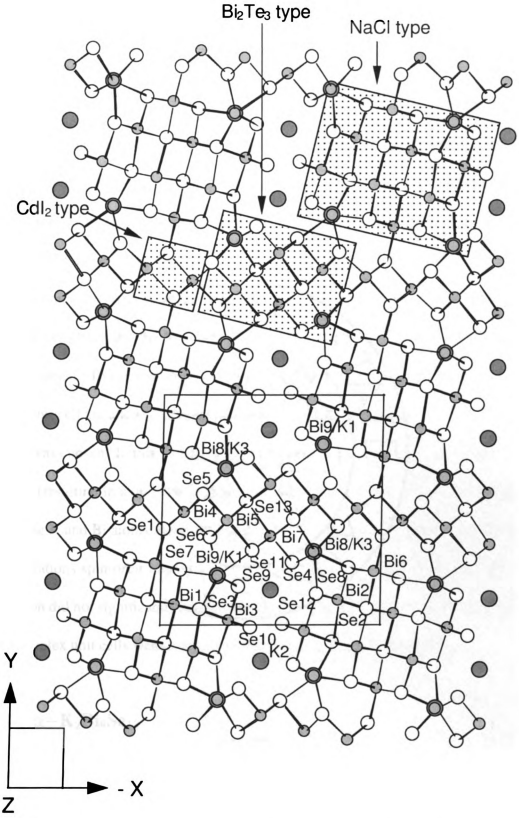

Figure 5.2: Projection of the crystal structure of $\beta-K_2Bi_8Se_{13}$ viewed down the c-axis (z-axis). Bi_2Te_3-, CdI_2- and NaCl- building blocks in the structure are highlighted by the shaded areas.

5.3 Electronic Structure and Effective Mass

Electronic structure calculations were performed using both the local density approximation (LDA) and the generalized gradient approximation (GGA) of Perdew, Burke and Ernzerhof [70] for the exchange and correlation potential. Before discussing the results of calculations, I will present the details of the optimization (atomic positions) procedure. Full optimization calculations including the shape and volume optimization and internal relaxation of all the atoms in the unit cell require a large amount of computational time for this complex compound (with 92 atoms in the unit cell). Therefore, only the volume optimization for the α-phase and the Supercell model of the β-phase (to be discussed later) have been performed. To see the effect of internal optimization (where positions of atoms inside the unit cell are allowed to relax) on the band structure, a simpler configuration of the β-phase was chosen. In this configuration we ignore the mixing of K and Bi atoms at the mix sites (resulting in a unit cell with smaller number of atoms) and allow for relaxations of both the K and Bi atoms along with their neighbouring Se atoms (Se4 and Se9). For all the calculations spin-orbit interaction (SOI) was included. Since this partially optimized calculation did not significantly change the band structure results, all other calculations for more complex unit cells were carried out only with volume optimizations.

5.3.1 $\alpha-K_2Bi_8Se_{13}$

The unit cell parameters of $\alpha-K_2Bi_8Se_{13}$(triclinic, space group P-1 with 23 atoms/ unit cell) are: a=26.108 a.u., b=22.858 a.u., c=7.872 a.u., α=89.98°, β=98.64°, γ=87.96°. [61] The corresponding Brillouin zone is shown in Fig. 5.3. The band structures along differ-

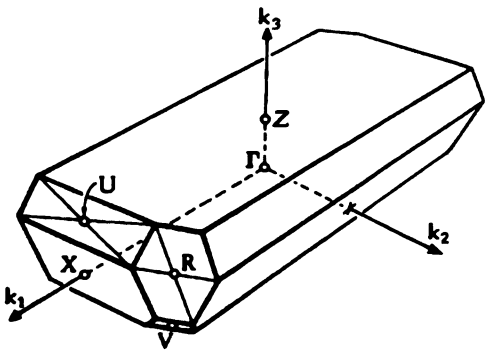

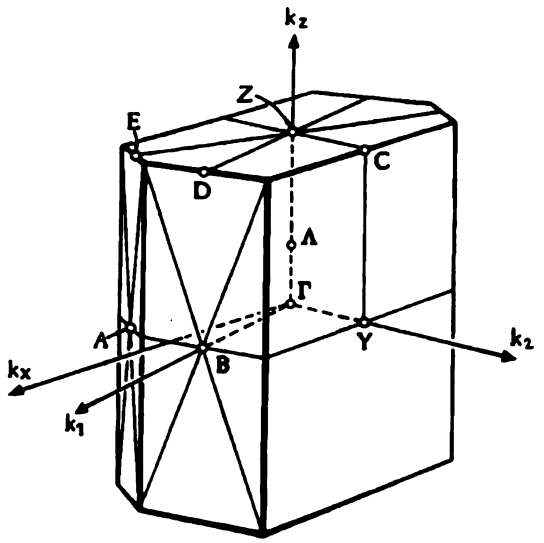

Figure 5.3: Brillouin zone of $\alpha-K_2Bi_8Se_{13}$ Figure 5.4: Brillouin zone of $\beta-K_2Bi_8Se_{13}$

ent symmetry directions at optimal volume V_{opt} are shown in Fig. 5.5. This compound is found to be an indirect band gap semiconductor. The effect of the SOI is to shift the conduction band down relative to the valence band and thereby decrease the band gap. Such reduction in the band gap caused by the SOI have been seen in other complex ternary systems, $CsBi_4Te_6$ [51] and $BaBiTe_3$. [50] The optimal volume V_{opt} for GGA calculations is 6% larger than experimental volume V_{exp}, whereas for LDA calculations V_{opt} is 2% smaller than V_{exp}. This is consistent with many previous calculations within LDA and GGA. [79, 88, 46] The values of the band gap without and with SOI for LDA/GGA calculations are given in Table 5.1. Excepting for GGA without SOI, the band gape values changed by less than 3%. The band gap values range between 0.37-0.47eV compared to the experimental value of 0.76eV. There can be two sources for this discrepancy; one is usual LDA/GGA band gap problem [2] and the other is that the measured gap is optical and hence a different gap than the indirect one was measured.

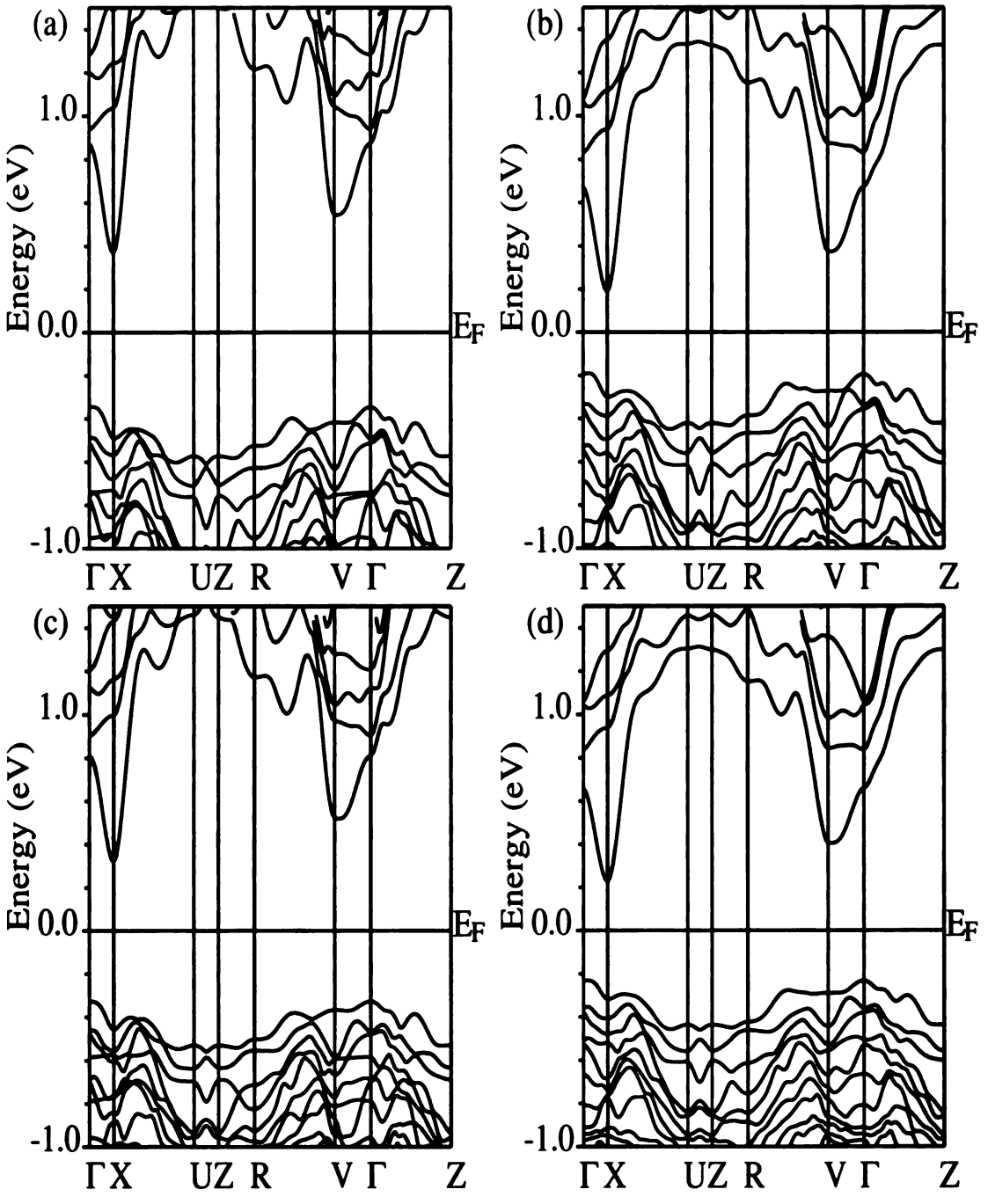

Figure 5.5: Band structure of $\alpha-K_2Bi_8Se_{13}$ at V_{opt} (a)LDA without SOI, (b)LDA with SOI, (c)GGA without SOI, and (d)GGA with SOI.

Table 5.1: Energy band gap values in eV corresponding to experimental volume V_{exp} and optimal volume V_{opt} for $\alpha-K_2Bi_8Se_{13}$.

	LDA		GGA		Experiment [61]
	V_{exp}	V_{opt}	V_{exp}	V_{opt}	
without SOI	0.71	0.71	0.82	0.65	0.76
with SOI	0.37	0.38	0.47	0.46	

Thermoelectric properties of this material are influenced by anisotropic effective masses (the *R* factor), which can lead to a high ZT value. [50, 51] The effective masses for both LDA and GGA at V_{opt} were obtained by calculating the values of energy close to the conduction band minimum (CBM) and the valence band maximum (VBM) while moving from the extremum points along the three orthogonal directions. We calculated energies for $\vec{k}$ values up to: $0.0625k_{1x}$, $0.0625k_{2y}$, and $0.03125k_{3z}$ where k_{1x}, k_{2y} and k_{3z} are the magnitudes of the projections of the reciprocal lattice vectors $\vec{k}_1$, $\vec{k}_2$, and $\vec{k}_3$ along the x, y and z directions respectively. The energy values were fitted to a quadratic polynomial. In general $\epsilon_{\vec{k}}$ can be expanded about an extremum point as :

$$\frac{2m_e}{\hbar^2}\epsilon_{\vec{k}} = \sum_{i,j} \lambda_{ij} k_i k_j; i,j = x,y,z \tag{5.1}$$

$$\lambda_{ij} = \frac{m_e}{m_{ij}}, \tag{5.2}$$

where λ_{ij} are the effective mass parameters (inverse of λ_{ij} is the effective mass tensor) and m_e is the free electron mass. In the present case the angles α and γ are close to 90° whereas the angle β differs appreciably from 90°. Thus we can assume λ_{xy} and λ_{yz} to be small and drop them from the expansion. The four remaining λ_{ij}'s are given in Table 5.2. As can be

Table 5.2: Effective mass parameters at V_{opt} for $\alpha-K_2Bi_8Se_{13}$

	LDA		GGA	
	VBM	CBM	VBM	CBM
λ_{xx}	1.78	6.16	1.31	5.57
λ_{yy}	0.98	1.15	0.99	1.16
λ_{zz}	1.29	9.29	1.15	8.56
λ_{xz}	0.71	0.13	0.84	0.25

seen in Table 5.2, the effective mass parameters of the VBM are fairly isotropic whereas those of the CBM are anisotropic with the smallest effective mass along the z-direction (c-axis). The differences in the effective mass parameter values within LDA/GGA are less than 36% and as expected (the effective mass tensor depend on the wave functions, whereas the energy in density functional theory depend on the charge density) these values are larger than the differences in the energy gap values which is $\sim$21% at V_{opt}.

Orbital character analysis reveals that Se1-7 and Bi4 atoms (see Fig. 5.1 for the numbering of different atoms in the unit cell) contribute to the highest valence band (HVB). This suggests a nearly 3-dimensional hole transport (in GGA which is supposed to be better, λ_{ij} vary between 0.84-1.31). On the other hand, Sb_2Se_3-type fragments do not contribute strongly to the lowest conduction band (LCB), which consists primarily of Bi1-3 p orbitals. This leads to a nearly 2-dimensional charge transport of the electrons confined to the Bi_2Te_3- and CdI_2-type layers (large variations in λ_{ij} from 0.25-8.56), suggesting better thermoelectric properties for the electron-doped systems through large $R=[\lambda_{zz}/(\lambda_{xx}\lambda_{yy})]^{1/2}$ factor defined in Chapter 1. [50]

5.3.2 $\beta-K_2Bi_8Se_{13}$

The unit cell parameters of $\beta-K_2Bi_8Se_{13}$ (monoclinic with space group P 2_1/m with 46 atoms/unit cell) are: a=33.055 a.u., b=34.886 a.u., c=7.946 a.u., and γ=90.49°. [9] The corresponding Brillouin zone is shown in Fig. 5.4. A proper electronic structure calculation for this compound should in principle incorporate the Bi8/K3 and K1/Bi9 mixed occupancy. *Ab initio* electronic structure calculations for disordered systems are still under development stage (KKR-CPA). [63] Therefore we have chosen two different ordered configurations with extreme occupancy of the Bi8/K3 and K1/Bi9 sites: Configuration I contains Bi8 atom at the Bi8/K3 site and K1 atom at the K1/Bi9 site, whereas Configuration II contains K3 atom at the Bi8/K3 site and Bi9 atom at the K1/Bi9 site.

Both before and after the inclusion of the SOI, Configuration I yields a semi-metal with several very flat bands along the ΓY and ABΓ directions of the Brillouin zone, (see Fig. 5.6) i.e. in the plane perpendicular to the z-axis also called the needle axis. Single crystal conductivity measurements show either a semi-metallic or a narrow-gap semi-conducting behavior. [9] Although the observed transport behavior appears to be consistent with band structure results, the measured optical gap of 0.59eV does not appear to be consistent with these results. An orbital analysis shows that the top of the "valence band" consists of Se9 p and Se10 p bands (Fig. 5.6 a, b) while the lowest two conduction bands have Bi8 p and Se4 p hybridized orbital character (Fig. 5.6 c, d). Se9 lies at the edge of the NaCl- fragment next to the K1 atom occupying K1/Bi9 site whereas the Se4 lies at the edge of the Bi_2Te_3-fragment next the Bi8 atom at the Bi8/K3 site. In this configuration Se9 atom has two K1 atoms as nearest neighbors whereas Se4 atom has two Bi8 atoms as nearest neighbors.

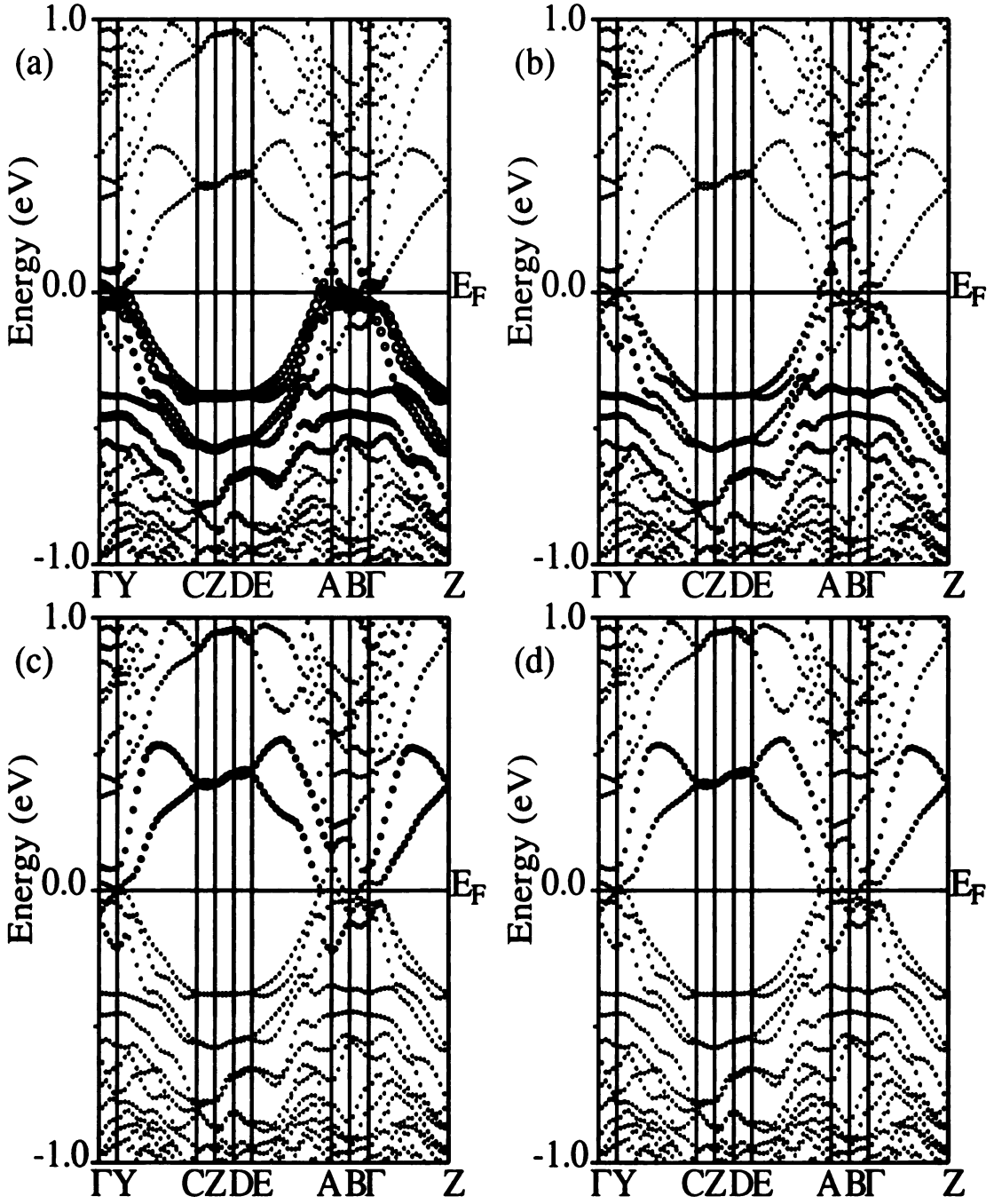

Figure 5.6: Band structure of $\beta-K_2Bi_8Se_{13}$-Configuration I with SOI. Orbital character of (a) Se9 p, (b) Se10 p, (c)Bi8 p, (d) Se4 p. The size of the circles is directly proportional to the strength of the orbital character.

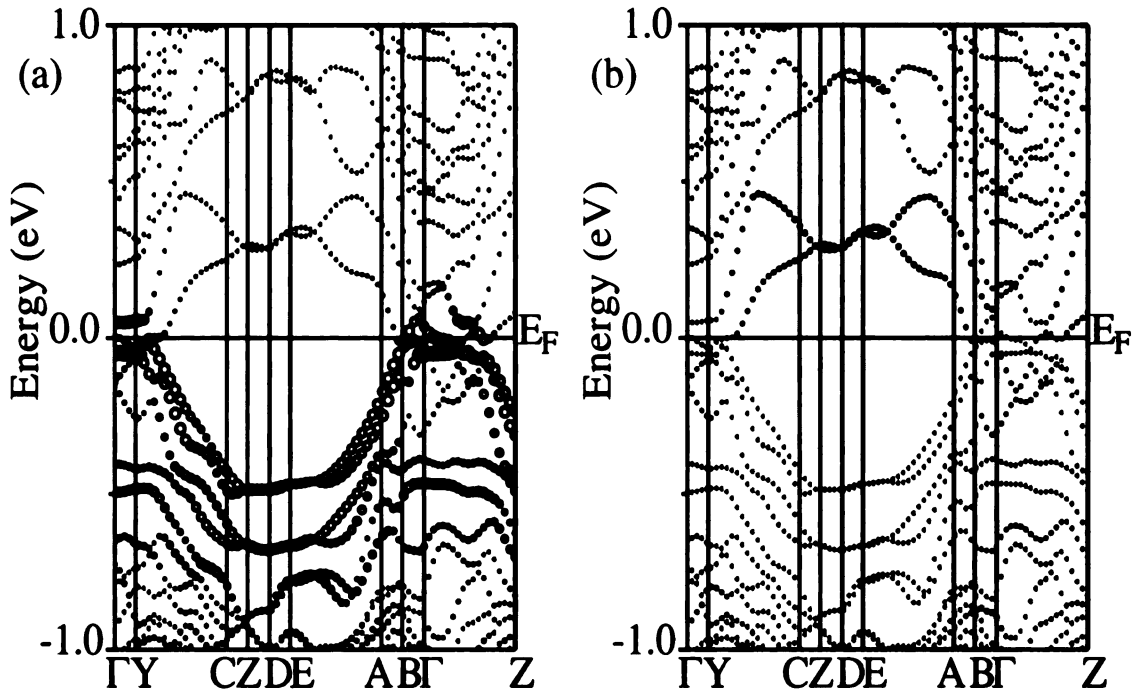

Figure 5.7: Band structure of $\beta-K_2Bi_8Se_{13}$-Configuration I with SOI for partially optimized calculations. Orbital character of (a) Se9 p, (b) Se4 p. The size of the circles is directly proportional to the strength of the orbital character.

The hybridization of Se4 p and Bi p states lowers the energy of Se4 p states, whereas the hybridization of Se9 p states with Bi p states is reduced since Se9 atom has two K1 atoms as nearest neighbors. As a result the Se9 p orbitals are not very well stabilized in energy and they float to the Fermi energy to give a semi-metallic behavior.

Since the experimental positions of the atoms at the mixed sites are some average positions, we performed volume optimization and internal relaxations (carried out only for the configuration I) of the atoms at mixed sites and their nearest neighbors (Se4 and Se9 atoms) in order to see the impact of the relaxation effects on the band structure results. V_{opt} for GGA calculations correspond to $\sim$4% increase from V_{exp}. The internal optimization calculation increases the K1-Se9 atomic distance to 3.21Å from 2.85Å whereas the Bi8-Se4 atomic distance of 2.88Å remains almost unchanged. In spite of the above

changes, the optimized calculations (Fig. 5.7 a, b) show the same semi-metallic behavior with band structure results very similar to those of the unoptimized calculation (Fig. 5.6 a, d). Therefore, our calculations for other configurations (discussed next) did not include internal relaxations.

In the case of Configuration II, before the inclusion of SOI, there is a direct gap of 0.38eV which appears promising $vis - \grave{a} - vis$ experiment. But after inclusion of SOI, the gap disappears and the band structure looks very similar to that of the Configuration I. Orbital character analysis shows that in this case the top of the "valence band has" Se4 p orbital character (instead of Se9 in Configuration I) (Fig. 5.8 a), while the lowest two conduction bands have Bi9 p and Se9 p (instead of Bi8 p and Se4 p) hybridized character (Fig. 5.8 b). In this configuration Se4 atom has two K3 atoms as nearest neighbors. As a result Se4 p orbitals now float up to the Fermi energy giving rise to a semi-metallic character.

Since both the configurations with extreme occupancy of Bi and K atoms at the mixed sites (Configuration I and II) show semi-metallic behavior, the observed semiconductor behavior of $\beta-K_2Bi_8Se_{13}$ has to originate from the mixed site occupancy. In order to incorporate the mixed occupancy we have chosen a 1x1x2 supercell (92 atoms/cell) with an alternative occupancy of K and Bi atoms at the mixed sites. In this ordered superlattice model both Se9 and Se4 atoms have one K and one Bi atoms as nearest neighbors. The LDA/GGA band structure results show that the system is an indirect gap semiconductor (Fig. 5.9). The effect of SOI is to decrease the energy band gap as has been seen in many Bi, Te, and Se narrow band gap semiconductors. [50, 51] V_{opt} for LDA calculations cor-

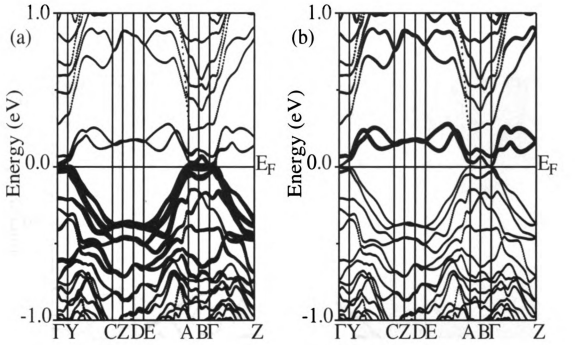

Figure 5.8: Band structure of $\beta-K_2Bi_8Se_{13}$-Configuration II with SOI. Orbital character of (a) Se4 p, (b) Bi9 p.

respond to ~4% decrease from V_{exp}, whereas V_{opt} for GGA calculations correspond to ~5% increase from V_{exp}. The VBM occurs at the A point (located at [0.5, 0.5, 0] in fractions of the primitive reciprocal lattice vector lengths) whereas the CBM is located at [0.4, 0.55, 0] for LDA and at [0.375, 0.575, 0] for GGA inside the Brillouin zone. The values of the energy band gap are given in Table 5.3 which range from 0.56-0.66eV without SOI and 0.32-0.44eV with SOI. As before the effect of volume relaxation on the band gap is quite small. The experimentally measured optical gap is 0.59eV. [9]

Orbital character analysis reveals that the states near the bottom of the CBM consist of Bi9 and Bi8 p orbitals strongly hybridized with the Se and Bi p orbitals of atoms close to the mixed sites whereas the states near the VBM have mostly hybridized Se10 and Bi3 p orbital character. The states near the VBM have small contribution from Se9 p orbitals and

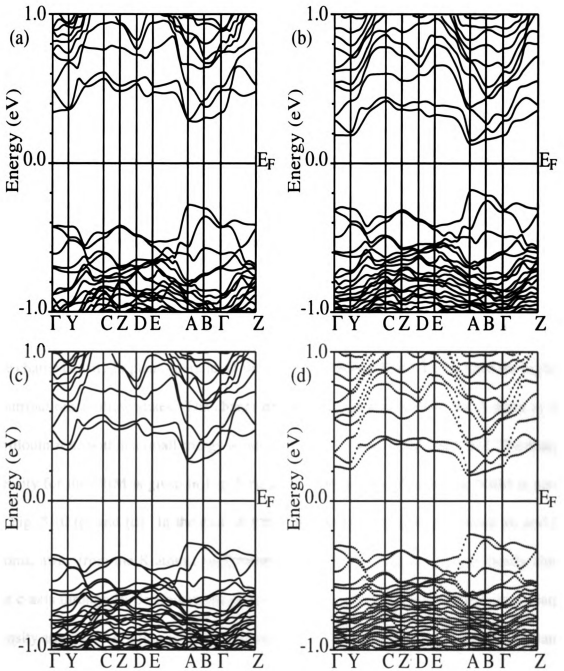

Figure 5.9: Band structure of $\beta-K_2Bi_8Se_{13}$-Supercell at V_{opt} (a)LDA without SOI, (b)LDA with SOI, (c)GGA without SOI, and (d)GGA with SOI.

Table 5.3: Energy band gap values in eV corresponding to experimental volume V_{exp} and optimal volume V_{opt} for $\beta-K_2Bi_8Se_{13}$-Supercell.

	LDA		GGA		Experiment [9]
	V_{exp}	V_{opt}	V_{exp}	V_{opt}	
without SOI	0.58	0.56	0.63	0.66	0.59
with SOI	0.33	0.32	0.39	0.41	

no contribution from Se4 p orbitals since the latter states are better stabilized in energy. Bi atoms at mixed sites stabilize the p orbitals of Se4 and Se9 atoms by lowering their energy. Therefore, this alternative K/Bi order at mixed sites along the c-axis (needle axis) is crucial for the gap formation.

In order to better understand the nature of the states near the CBM and VBM we plot the charge density in planes parallel to the z-axis containing atoms which have the highest contributions to these states. The charge densities were calculated for the A point in the Brillouin zone within a small energy window of 0.2eV around CBM and VBM. The charge density for the CBM is given in Fig. 5.10 (a) and (b) whereas that for the VBM is given in Fig. 5.10 (c) and (d). In the case of CBM the charge is distributed around Bi and Se atoms, away from the K atoms, suggesting that the charge transport occurs mostly along the c-axis through Bi-Se framework since in the plane perpendicular to the z-axis charge density around the K atoms is extremely small. The plot of charge density through the same plane as in Fig. 5.10 (b) for the VBM states (Fig. 5.10 c) shows that the atoms included in this plane have very small contributions to these states. The states near the VBM are antibonding, mostly localized around Se10, Bi3, Se3, and Se9 atoms (Fig. 5.10 d). The charge density plots reveal that the electron and the hole transport regions are separated in

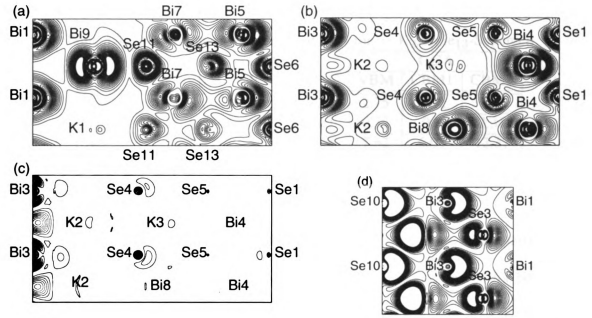

Figure 5.10: Charge density of $\beta-K_2Bi_8Se_{13}$-Supercell in planes parallel to the c-axis corresponding to (a), (b) CBM states and (c), (d) VBM states. The charge density is represented by closed lines from low charge density regions to high charge density regions in steps of $5x10^{-4}$ electrons/$Å^3$.

space.

The effective masses associated with the two LDA/GGA CBM at [0.4,0.55,0]/[0.375, 0.575, 0] (called CBM1) and at the A point (called CBM2) in the Brillouin zone together with the effective masses of VBM at the A point were calculated by dropping the λ_{xy} term in Eq. 5.1, since the angle γ is very close to 90°. The results are given in Table 5.4. As seen in the α-phase, the LDA/GGA differences of the effective mass parameters are larger than the differences in the energy band gap (~28%) at V_{opt}. The effective mass calculations show strong anisotropy in both the hole and electron effective masses with the smallest effective mass along the needle axis. As has been discussed before the value of *ZT* increases with the dimensionless parameter *B* defined in Chapter 1 and the *B* factor is directly proportional to the fraction $R=[\lambda_{zz}/(\lambda_{xx}\lambda_{yy})]^{1/2}$ of the effective mass parameters.

Table 5.4: Effective mass parameters at V_{opt} for $\beta-K_2Bi_8Se_{13}$-Supercell

	LDA			GGA		
	VBM	CBM1	CBM2	VBM	CBM1	CBM2
λ_{xx}	3.66	1.63	5.35	2.75	2.22	9.3
λ_{yy}	0.73	1.08	0.62	0.33	0.9	2.31
λ_{zz}	8.77	5.15	11.86	7.62	6.01	12.37
$(\frac{\lambda_{zz}}{\lambda_{xx}\lambda_{yy}})^{1/2}$	1.81	1.71	1.89	2.9	1.74	0.76

The values of R are also shown in Table 5.4. These values are greater than unity (except CBM2 within GGA) suggesting that $\beta-K_2Bi_8Se_{13}$ has a great potential for both p and n-type thermoelectric. The high effective mass anisotropy in the vicinity of the VBM and CBM explains the strong charge transport anisotropy found in this system. [45]

5.4 Summary

Electronic structure calculations show that the $\alpha-K_2Bi_8Se_{13}$ is an indirect band gap semiconductor with a LDA/GGA band gap of 0.38eV/0.46eV at the optimized volume V_{opt}. Direct band gaps of 0.65eV at the V point and 0.75eV at the X point in the Brillouin zone are found, in good agreement with the observed optical gap of 0.76eV. [61] On the other hand in $\beta-K_2Bi_8Se_{13}$, the atoms at the mixed sites are found to be very important in determining the electronic properties of this material. When the mixed sites are treated as fully occupied by K or Bi atoms (Configurations I and II) the system is a semimetal. Incorporation of mixed occupancy (through a supercell structure) results in an indirect gap semiconductor with a LDA/GGA band gap of 0.32eV/0.41eV at V_{opt}. Although the indirect gap (relevant in transport) has not been measured experimentally, we find two flat

bands along the ΓY direction separated by ~0.49eV for LDA and ~0.53eV for GGA. This is consistent with the observed direct gap of 0.59eV (optical). [9]

It is of interest to discuss the effect of disorder between K and Bi atoms at the mixed sites on the electronic band structure of $\beta-K_2Bi_8Se_{13}$. It is possible, that in the real system there exist regions close to Configuration I and II, which may create in-gap states. These states will then contribute to charge transport raising the value of electrical conductivity. This may be a plausible explanation for the higher observed value of electrical conductivity (σ=250 S/cm) in $\beta-K_2Bi_8Se_{13}$ as compared to the low value of electrical conductivity (σ=2 S/cm) in $\alpha-K_2Bi_8Se_{13}$.

The ability of the mixed K/Bi sites to achieve various degrees of ordering has been deduced from samples of $\beta-K_2Bi_8Se_{13}$ with different preparation and cooling history. Rapidly cooled samples exhibit a high enough K/Bi disorder to mask the presence of the band-gap (due to the in-gap states) and they also exhibit very high room temperature electrical conductivity (more than 1200 S/cm). Slowly cooled samples on the other hand (or annealing the rapidly cooled samples) have considerably fewer defects associated with the K/Bi disorder that result in readily observable band-gap of 0.59eV (spectroscopic) and significantly reduced electrical conductivity. Therefore a full exploration of the thermoelectric properties of this system will have to involve a careful control of the degree of disorder in the mixed K/Bi sites coupled with judicious doping. In addition, our calculations suggest that p-type samples could also be very interesting in that regard since they give a very high anisotropy factor $R=[\lambda_{zz}/(\lambda_{xx}\lambda_{yy})]^{1/2}$ associated with the valence band maximum. To date, p-type doping in $\beta-K_2Bi_8Se_{13}$ has not been observed but the electronic structure

results give plausible justification to pursue ways to achieve it.

Thermoelectric properties of $\beta-K_2Bi_8Se_{13}$ are also enhanced by the existence of some degree of K/Bi disorder which reduces the lattice thermal conductivity κ_{ph}. A value less than 1.28 W/mK for the total thermal conductivity has been seen [9] compared to 1.31 W/mK for $Bi_2Te_{3-x}Se_x$ alloys. The strong anisotropy in the electron effective mass combined with the low value of κ_{ph} make $\beta-K_2Bi_8Se_{13}$ to be an excellent candidate for room and high temperature thermoelectric materials.

Chapter 6

Electronic Structure of $AgPb_mSbTe_{2+m}$ (LAST-m), Complex Quaternary Systems

6.1 General Introduction

A novel class of quaternary compounds $AgPb_mSbTe_{2+m}$ denoted as LAST-m have attracted considerable attention during last two years because of their large figure of merit *ZT* (ZT$\sim$1.2 for LAST-12 and $\sim$2.2 for LAST-18 at 800K). [30] These compounds form in the rock-salt structure ($Fm\bar{3}m$ symmetry) similar to the binary PbTe, where Ag and Sb occupy Pb sites. One expects that by replacing two divalent Pb atoms by a monovalent Ag atom and a trivalent Sb atom, one will maintain the charge compensation and the resulting system will be a narrow band gap semiconductor. By controlling the Ag and Sb concen-

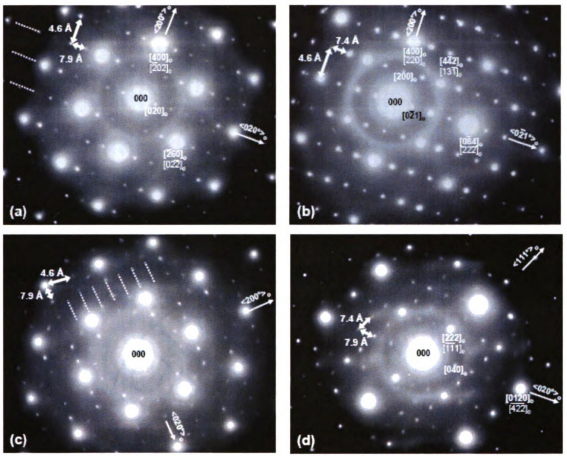

Figure 6.1: Electron diffraction pattern showing a lowering of the crystal symmetry from cubic to orthorhombic. They correspond to (a and c) $[111]_c$, (b) $[\bar{1}12]_c$ and (d) $[\bar{2}31]_c$ zone axis in face center cubic (fcc) symmetry (a_c=6.4Å). Superstructure spots can be indexed in orthorhombic symmetry according to $a_0 \sim$9.1Å, $b_0 \sim$15.8Å and $c_0 \sim$22.3Å unit cell. The corresponding zone axis are (a and c) $[001]_o$, (b) $[012]_o$ and (d) $[10\bar{1}]_o$. Indexations are given for both symmetries.

tration and their spatial ordering one can manipulate the bond strength and consequently their transport properties. Furthermore, having high symmetry structures, LAST-m systems are expected to maximize the degeneracy of the bands γ and by replacing Pb with Ag(Sb) atoms one expects to reduce the lattice thermal conductivity κ_{ph}, quantities which enter in the B factor defined in Chapter 1.

There are clear experimental evidences from single crystal X-ray diffraction (Fig. 6.1)

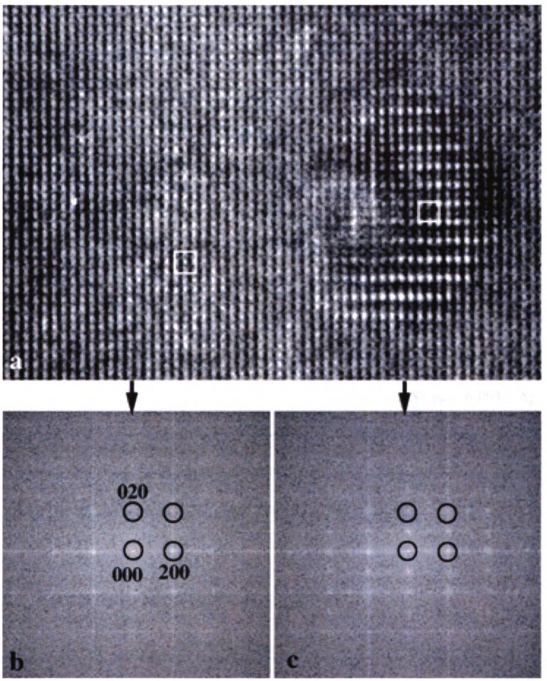

Figure 6.2: High resolution electron microscopy image from a LAST-18 sample (a), and the fast fourier transforms from the (b) PbTe matrix and (c) the Ag-Sb microscopic inhomogeneities. The electron beam is parallel to one of the [100] directions. The unit cells are indicated.

and high resolution electron microscopy (Fig. 6.2) that LAST-m systems are not simple solid solutions between $AgSbTe_2$ and PbTe phases. Rather, they exhibit microscopic inhomogeneities rich in Ag-Sb embedded into a PbTe matrix. These systems are example where quantum confinement (QC) concept can be achieved in bulk by controlling the formation of Ag-Sb microstructural arrangements. In addition, it is not correct to view the Ag and Sb atoms as dopants because they are present in large stoichiometric proportions (1 Ag(Sb) atom in 12 or 18 Pb atoms).

Given the close structural relationship of $AgPb_mSbTe_{2+m}$ to PbTe, a fundamental question is how the PbTe electronic structure gets modified by extensive substitution with Ag and Sb atoms and their microstructural arrangements. In order to address this question, I have carried out careful and systematic electronic structure calculations in $AgSbTe_2$ and PbTe the two end phases, Ag(Sb) single impurity in PbTe, Ag-Sb pair in PbTe, Ag-Sb chain, plain, and cluster microstructural arrangements in PbTe. The primary focus is to isolate some of the generic electronic structure features associated with the replacement of Pb by Ag and Sb and see how they influence the transport properties.

6.2 Electronic Structure of $AgSbTe_2$

$AgSbTe_2$ forms in the rock-salt structure (unit cell parameter a=6.06Å) similar to PbTe. The nature of chemical bonding in $AgSbTe_2$ and PbTe is mixed ionic-covalent. With decreasing ionicity one expects the rock-salt structure to become unstable toward a rhombohedral phase. In fact, a cubic to rhombohedral phase transition occurs at room temperature with ordering of Ag and Bi in $AgBiS_2$ and $AgBiSe_2$. For $AgSbSe_2$ and $AgSbTe_2$ early

experimental studies indicated that the disordered cubic structures persisted even at room temperature. [21] Recent careful experiments suggest long range complex ordering of Ag and Sb. [72] But the exact crystal structure is not known. In the absence of a detailed structural information from experiment we have taken several ordered structures and compared their energies using *ab initio* DFT.

In the simple ionic model $AgSbTe_2$ is charge balanced $Ag^{+}Sb^{+3}Te_2^{-2}$. For the cations, the fluctuating charge from the average +2 charge (Pb^{+2}) is -1 for Ag and +1 for Sb. We use the magnetic analogy (Ag=↑ and Sb=↓) for defining different ordered structures. These structures are antiferromagnetic (AF) type I, II, IIIA and IIIB (Fig. 6.3A,B,C, and D). In addition to these "antiferromagnetic" orders, other structures were chosen and named type 1-$AgSbTe_2$ (Fig. 6.3E), type 2-$AgSbTe_2$ (Fig. 6.3F). Type 2-$AgSbTe_2$ consists of alternating layers of Ag and Sb perpendicular to the [111] cubic direction. Since the type 2-$AgSbTe_2$ can be reduced to a smaller hexagonal unit cell with the c-axis parallel to the [111] cubic direction (Fig. 6.3G), the latter was used in this calculation. Also models in a 2x2x1 hexagonal unit cell consisting of mixed Ag/Sb layers perpendicular to the c-axis have been considered and are denoted as type 3-$AgSbTe_2$ (Fig. 6.3H).

Let's discuss the general features of the density of states (DOS) to see whether these compounds are narrow band gap semiconductors, semimetals or metals. DOS for type I AF structure shows semimetallic character with a pseudogap near the Fermi energy (Fig. 6.4A). The Ag d orbitals are located below the Fermi energy and they are fully occupied (Fig. 6.4B). In the (-5.0eV, 5.0eV) energy range the Ag s orbitals hybridize with Te p orbitals (Fig. 6.4C) . This suggests that Ag atoms are in an oxidation state which is less

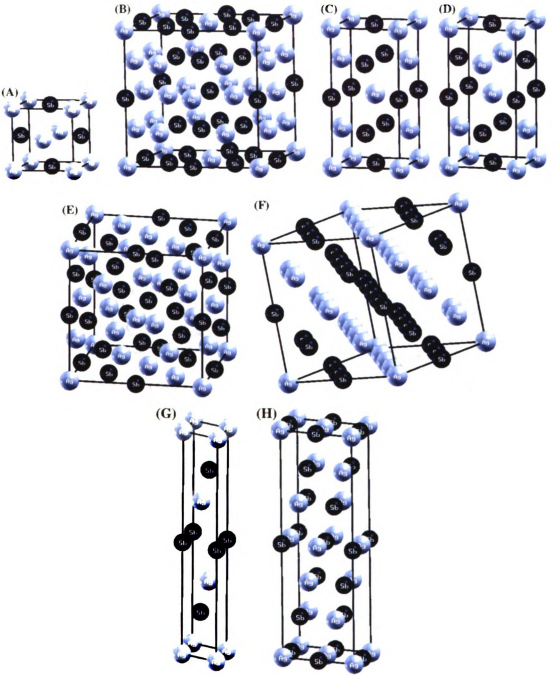

Figure 6.3: Unit cell lattices of ordered structures: (A) type I, (B) type II, (C) type IIIA, and (D) type IIIB AF order; (E) type 1-$AgSbTe_2$, (F) type 2-$AgSbTe_2$, (G) type 2-$AgSbTe_2$ in hexagonal symmetry, and (H) type 3-$AgSbTe_2$. For the sake of clarity Te atoms are not included.

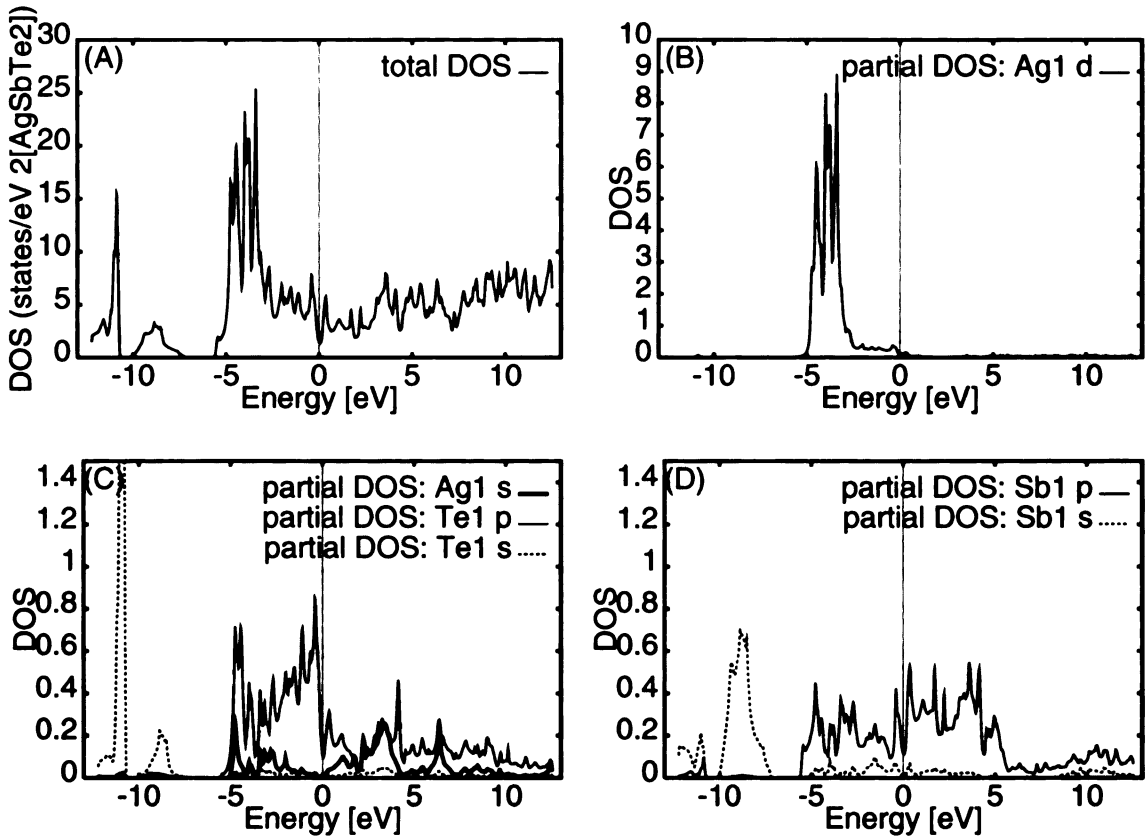

Figure 6.4: Density of states (DOS) for type I AF model structure.

than +1. The Te and Sb s states are very well stabilized in energy between -12eV and -8eV. These states do not mix with the p states of Te and Sb atoms (Fig. 6.4C,D). The Te and Sb p states, which lie in the range -5eV and 0eV hybridize with each other, indicating a strong covalent interaction between Te and Sb atoms. The overlap of the p states of Te and Sb gives a semimetallic band structure.

The DOS results for all other ordered structures show similar semimetallic behavior with low DOS near the Fermi energy. This is a result of the hybridization between the p states of Te and Sb atoms, which are very close in energy. In Fig. 6.5 we show only the total DOS of these different structures. The rapid increase in the DOS near the Fermi energy (both above and below) suggests that these systems will show large thermopower when the

chemical potential moves away from the minimum with doping.This observation is consistent with the large room temperature experimental value of thermopower S=266μV/K measured by Noda *et. al.* [64] Noda *et. al.* also measured electrical conductivity σ and thermal conductivity κ. These values are 147 S/cm and 1.07 W/mK respectively. The room temperature ZT for $AgSbTe_2$ is $\sim$0.29. In comparison, the best room temperature thermoelectric are Bi_2Te_3 alloy (ZT=1.14) and $(Bi_2Te_3)_m(Sb_2Te_3)_n$ superlattice systems (ZT=$\sim$1.4 and $\sim$2.4).

Even if all the different structures are semimetals with a pseudogap at the chemical potential it is important to find out which structure has the lowest energy. To compare the total energy E_{tot} of different ordered structures, volume optimization and force minimization up to 1mRy/a.u were performed. The total energies per formula unit f.u. (f.u.=$AgSbTe_2$) are given in Table 6.1.

The lowest energy E_0 correspond to type 1-$AgSbTe_2$ order (see Fig. 6.5D). E_{tot} of all the ordered structures studied are within the 0-0.2eV/f.u. energy range. These energies, except for the type 1-$AgSbTe_2$, are very close (0.131-0.203eV). This suggest that $AgSbTe_2$ can develop disorder without much difficulty at finite temperatures.

Table 6.1: Total energies of $AgSbTe_2$ ordered model structures.

Type	**atoms/cell**	**E_{tot}/f.u. (Ry)**	**E_{tot}-E_0 (eV)**
I AF	8	-50789.51675	0.161
II AF	64	-50789.51637	0.166
IIIA AF	16	-50789.519	0.131
IIIB AF	16	-50789.51658	0.164
1-$AgSbTe_2$	32	E_0=-50789.5286	0.0
2-$AgSbTe_2$	12	-50789.5137	0.203
3-$AgSbTe_2$	48	-50789.5178	0.147

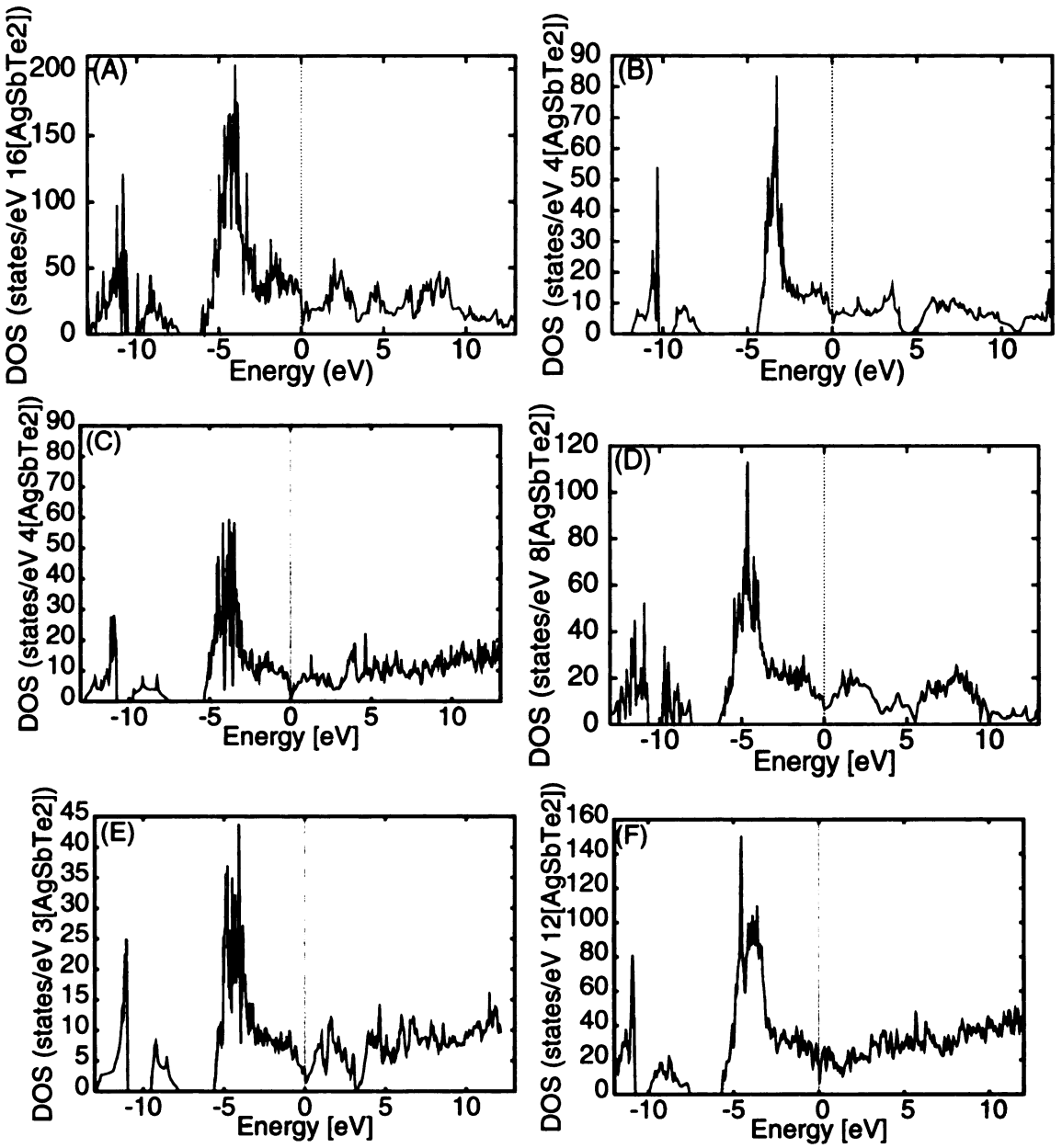

Figure 6.5: Total DOS of:(A) type II, (B) type IIIA, and (C) type IIIB AF structure; (D) type 1-$AgSbTe_2$, (E) type 2-$AgSbTe_2$, and (F) type 3-$AgSbTe_2$.

Experimental measurements in $AgSbTe_2$ give rather intriguing results. Electrical conductivity and Hall coefficient measurements in single crystal $AgSbTe_2$ by Gochev *et. al.* [22] in the temperature range 300-600K show a temperature dependence not typical for semiconductors. There is a minimum in the conductivity at T$\sim$500K. Fitting the data to an exponential in the range 500-600K gives an energy gap $E_g \sim 0.2$eV. Energy gaps ranging between 0.27-0.35eV have been obtained in earlier studies. Later measurements by Elsayed *et. al.* [17] in the range 600-700K gives $E_g \sim 0.218$eV for the solid state. Our theoretical calculations show that the different structural models we have investigated give a semimetal with a pseudogap near the chemical potential. Furthermore, the near proximity in energy of the different structures suggest there will be structural defects. These will give rise to localized states near the chemical potential which will control transport properties, particularly at low T. Careful low T (T<300K) experiments of σ and S are needed to sort things out. Whether one can understand these unusual electrical properties of $AgSbTe_2$ within a pseudogap picture needs further investigations.

6.3 Electronic Structure of PbTe

The rock-salt structure semiconductors PbS, PbSe, and PbTe are quite interesting, they show a series of electronic anomalies relative to the usual II-VI semiconductors (such as CdTe). For example, the direct gap occurs at the L point and the order of the band gap and valence band maximum energies in going from S to Te are anomalous. The band gap pressure coefficient is also anomalous, it is negative. Because of these peculiarities and their practical applications, there have been many electronic structure calculations in

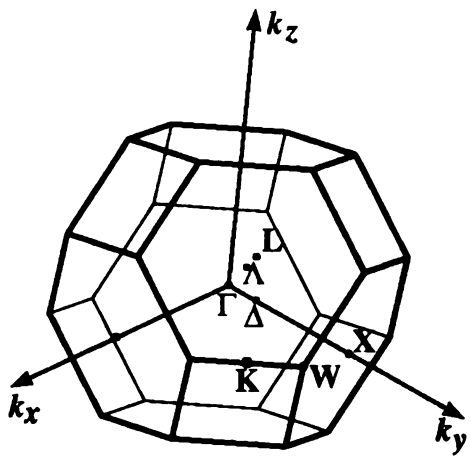

Figure 6.6: Face centred cubic (fcc) Brillowin zone of PbTe.

these compounds. [67, 60, 97, 99, 1, 47] Wei and Zunger [99] have recently carried out extensive electronic structure calculations using local density approximation (LDA) [29] as implemented through the linearized augmented plane-wave (LAPW) method. [85] They have argued that the above anomalous features can be ascribed to the occurrence of the Pb s-band below the top of the valence band, setting up coupling and level repulsion at the L point. Albanesi *et al* [1] have calculated the frequency dependent dielectric constant of PbSe and PbTe using the electronic structure (obtained with LAPW) within both LDA and generalized gradient approximation (GGA) [70]. They found a large dielectric constant for PbTe in agreement with experiment. [83, 89] I have carried out extensive all electron LAPW calculations within both LDA and GGA to confirm the findings of Wei and Zunger, to analyze the covalency between Pb and Te (by calculating the effective ionic charge) and to understand the bonding and antibonding nature of the electronic states near the fundamental gap.

The band structure results show that PbTe is a direct band gap semiconductor with a small gap value of ~0.09eV at the experimental volume V_{exp}. The volume optimization

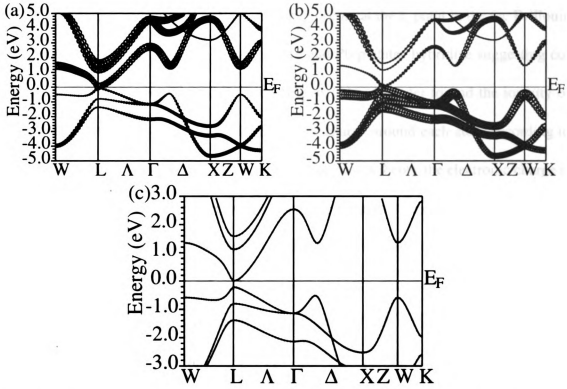

Figure 6.7: Band structure of PbTe at V_{exp} along different directions in the fcc Brillouin zone. Orbital character of : (a) Pb p and (b)Te p. The size of the circles is proportional with the orbital character. (c)Band structure of PbTe at V_{opt}.

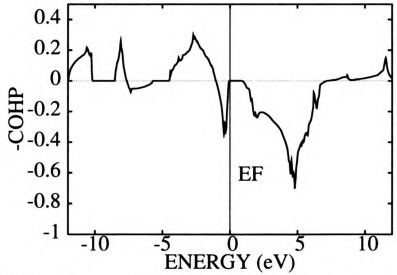

Figure 6.8: -COHP as a function of energy for PbTe without including spin-orbit interaction (SOI).

increases the gap to ~0.19eV (Fig. 6.7c). The GGA(LDA) optimal volume V_{opt} correspond to 5% increase(decrease) in V_{exp}. The gap occurs at the L point in the fcc Brillouin zone (Fig. 6.6). Orbital analysis shows that Te and Pb p states hybridize suggesting covalent interaction between Pb and Te atoms(Fig. 6.7a,b). In order to find the ionicity of Pb and Te atoms we have computed the electronic charge around each atom according to Bader's "Atoms in Molecules" theory. [3] According to this theory the electronic charge is calculated inside a volume centered around each atom. For each atom, the charge densities along different directions are calculated in order to find the points with minimum charge density. Then, the volume around each atom is found by connecting the points with minimum charge density. The results show an ionic state of $Pb^{+0.64}Te^{-0.64}$, which is much smaller than that of the pure ionic model $Pb^{+2}Te^{-2}$. Therefore in PbTe covalent interactions play an important role. The reduction in formal charges from 2(-2) to 0.64(-0.64) is consistent with the large dielectric constant of PbTe. A crystal orbital Hamilton population (COHP) analysis has been found to be a bond-detecting tool for solids and molecules. COHP partitions the band structure energy (in terms of the orbital pair contributions) into bonding, nonbonding and antibonding energy regions within a specified energy range. [15] In Fig. 6.8, -COHP is plotted as a function of energy. Positive values of -COHP describe bonding energy regions whereas negative values describe antibonding energy regions. As can be seen in Fig. 6.8 in the (-1,0)eV energy range (states near the top of the valence band), the electrons occupy antibonding states. Both the valence band maximum (VBM) and conduction band minimum (CBM) states at the L point are antibonding in nature (Note that in Fiq. 6.8, we have arbitrarily chosen Fermi energy E_F to be at the top of the valence

band).

6.4 Effect of Ag-Sb Microstructural Arrangements on Electronic Structure of LAST-m systems

6.4.1 Defects in PbTe

Defects (shallow and deep) in semiconductors are known to profoundly alter their electronic structure near the band gap and control their transport properties. Unlike shallow impurity levels, which are produced by long ranged Coulomb potential, deep levels are produced by the short-range atomic-like defect potential. [69] It is believed that shallow impurities primarily control the magnitude and type of conductivity (by controlling the type of carriers, electrons or holes, and their concentration) whereas deep defect levels primarily control the charge-carrier life-time. The detailed understanding of shallow defects in common semiconductors traces back to the classic work of Kohn and Luttinger and can be regarded as basically understood. [41, 68] However the problem of defects in narrow-gap semiconductors, particularly the physics underlying deep defect states is far from understood. LAST-m systems are particularly interesting because here both shallow defects caused by long-range Coulombic potential, deep defects formed by short range interactions and mixture of these may coexist.

The theory of deep defects in semiconductors in general and narrow band-gap semiconductors in particular has a long history. For substitutional defects in PbTe Lent *et. al.* [53] presented a simple chemical theory of s- and p- bonded substitutional impurities.

This theory naturally gave deep defect states near the fundamental band gap and also predicted resonant levels further away from the gap. The central idea of this theory is that due to large static dielectric constant of ($\sim 10^3$) [1], the Coulombic forces are screened out and local bonding considerations dominate the impurity state formation. The resulting defect states are referred to as deep defect states. Their location and character is determined mainly by the short range central cell defect potential. Because the fundamental band gaps of IV-VI semiconductors are so small ($\sim$0.2 eV), most of these defect energy levels can lie any where *vis-à-vis* the fundamental band gap. A careful *ab initio* electronic structure calculation is therefore needed to understand these defect states quantitatively.

To understand the basic physics underlying these deep defect states we present a simple chemical argument given by Lent *et. al.* If we start from pure PbTe and consider Cs-row impurities at the Pb site we can think of a Pb "defect" at the Pb-site which has an s-level in the valence band and p-levels in the conduction band. The conduction band is primarily Pb p-like and the Pb s states lie in the valence band. Making the defects more electropositive i.e. going from column-IV to Column-0, drives these defect levels up in energy until eventually the s-level crosses into the conduction band (between Column-0 and Column-I) to form the deep levels of the vacancy in the conduction band far above the conduction band minimum (CBM). Similarly by making the defects more electronegative (going from Column-IV to Column-VII) drives the energy levels down, so that the p-levels ultimately drop into the valence band. Lent *et. al.*'s calculations indicated that the defect p-levels cross the gap to the right of Column-VIII. They showed that Bi (trivalent) impurity gave a resonant p-like state (more than 0.5 eV above the CBM) which was partially occupied.

In contrast Cs impurities gave s-like deep defect states near the top of the valence band, which were partially occupied. In the following subsections we see how *ab initio* calculations which are self-consistent and incorporate the screening effects properly, quantitatively justify some of these empirical findings.

6.4.2 Models for Ag-Sb Microstructural Arrangement

First, calculations for isolated Ag and Sb impurity atoms in the PbTe lattice were performed in order to obtain a clear picture of their individual role in modifying the electronic structure of PbTe (Fig. 6.9a). These calculations were carried out using supercell models and the size of the supercell was chosen to minimize the impurity-impurity coupling within available computing resources. Then both Ag and Sb were introduced to simulate stoichiometries relevant to those of LAST-m compounds. Given that the exact crystal structure is not known, several plausible microstructural models were examined, all of which involved long range ordering of the atoms. In one model Ag and Sb atoms were placed in monolayers (Fig. 6.9b,c). In another model Ag and Sb atoms were placed along infinite chains running parallel to a crystallographic unit cell axis (e.g. c-axis)(Fig. 6.9d). In yet a third arrangement, the atoms were placed in the center of a 3x3x3 supercell to create a "$AgSbTe_2$ nanodot" embedded in a PbTe matrix (Fig. 6.9e). The chain and cluster models are in qualitative agreement with experimental transmission electron microscopy (TEM) observations of Ag-Sb ordering. [30] Although these arrangements capture much of the crystal physics in these materials, there are many more that could be considered which nevertheless should result in similar general conclusions.

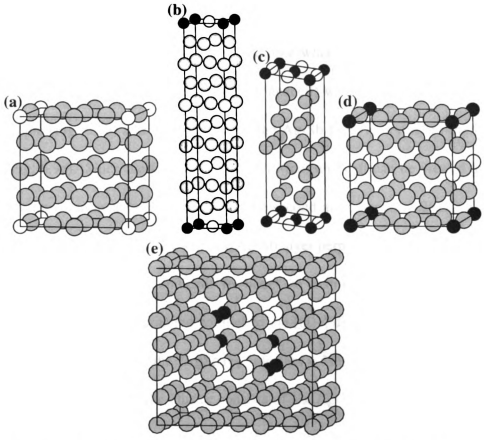

Figure 6.9: Unit cell models for (a) single Ag impurity atom in $AgPb_{31}Te_{32}$, (b) Ag-Sb layer perpendicular to [001] direction in $AgSbPb_{18}Te_{20}$, (c)Â Ag-Sb layer perpendicular to the fcc [111] direction in $AgSbPb_{10}Te_{12}$, (d) Ag-Sb chain parallel to the [001] direction in $AgSbPb_{30}Te_{32}$, and (e) Ag-Sb cluster in $AgSbPb_{16}Te_{18}$. For the reason of clarity we show only Pb fcc lattices with Pb in gray, Ag in white, and Sb in black colors.

To model the isolated Ag(Sb) and Ag-Sb pair impurities, 2x2x2 supercells with 64 atoms have been constructed. For the isolated case, Ag(Sb) were chosen at the origin of the supercell with a separation of two lattice constants (12.924Å) between the Ag(Sb) atoms (Fig. 6.9a). For the Ag-Sb pair, two arrangements have been considered (not shown in Fig. 6.9), one where the Ag and Sb are far apart (Sb at the origin and Ag at the center of the supercell) with a separation distance of $\sim$11.19Å and the other where the Ag and Sb are as close as possible (Sb at the origin and Ag at the next nearest neighbor site of Sb)

with a separation distance of ~4.57Å. For the structure where Ag-Sb layers are separated by several Pb layers two cases were considered, one where the Ag-Sb layer is normal to the [001] direction in a 1x1x5 supercell (40 atoms/cell) with the Ag-Sb layer located in the z=0 plane (Fig. 6.9b) and the other where the Ag-Sb layer is normal to the [111] direction (Fig. 6.9c). Since the face centered cubic (fcc) unit cell can be viewed along the [111] direction as a hexagonal unit cell, for the second arrangement a 2x2x2 hexagonal supercell (48 atoms/cell) was used with the Ag-Sb layer perpendicular to the c-axis which is the [111] direction of the fcc unit cell. To model the chains a 2x2x2 supercell was used, where the Ag-Sb chains are oriented parallel to the [001] direction (Fig. 6.9d) and separated by 12.924Å. Finally, for the "$AgSbTe_2$" clusters a 3x3x3 supercell (216 atoms/cell) has been constructed, where the cluster consists of six Ag-Sb pairs located at the center of the supercell with a minimum separation distance between two clusters of ~12.924Å (Fig. 6.9e).

6.4.3 Electronic Structure of Ag-Sb Microstructural Arrangements

The total DOS for isolated Ag atoms is shown in Fig. 6.10a. It can be seen that Ag introduces states near the top of the PbTe valence band (VB). Partial DOS analysis shows that these states consist mostly of p orbitals of the six nearest neighbor Te (Te2) atoms of Ag (Fig. 6.10b). These states are resonant with the VB and extend into the PbTe gap region. On the other hand the isolated Sb impurity introduces resonant states near the bottom of the PbTe conduction band (CB) (Fig. 6.10c) which extend nearly ~0.75 eV into the CB starting from the CB bottom. It also dramatically increases DOS near the CB bottom. Sb and

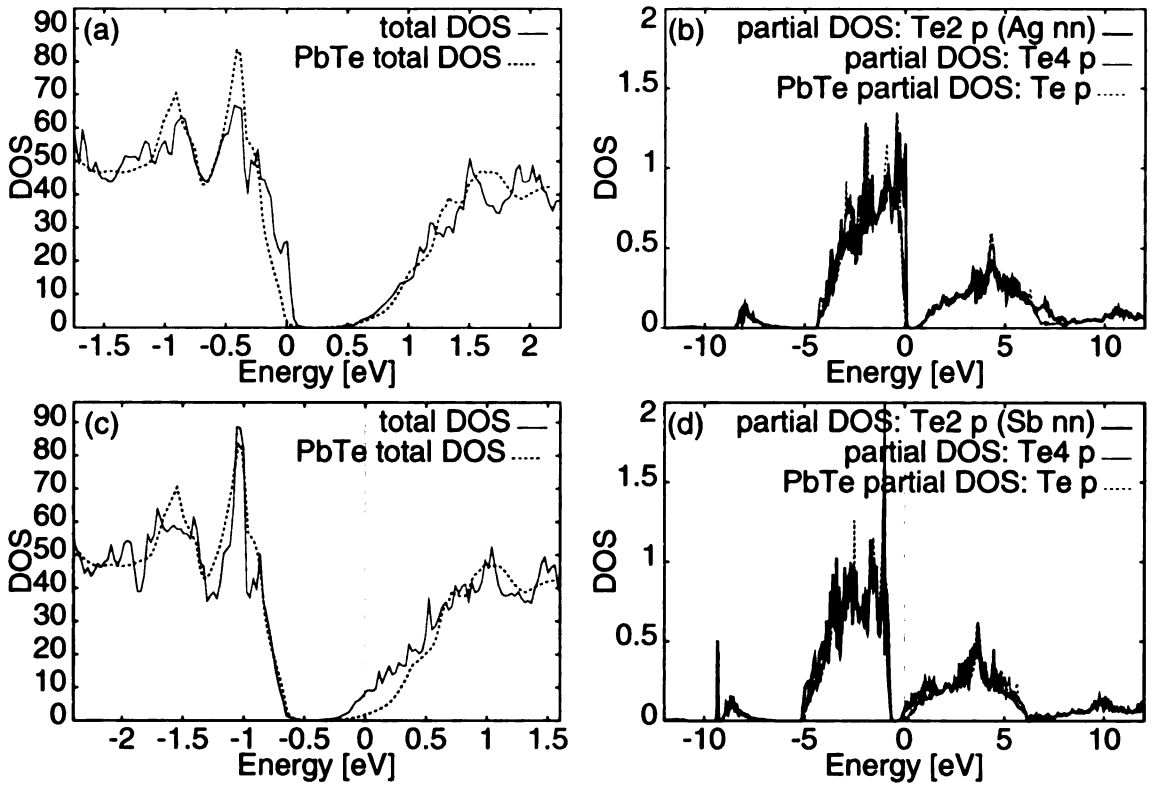

Figure 6.10: Total DOS of (a) Ag and (c) Sb single impurity atom in PbTe. For comparison the total DOS of bulk PbTe is shown in dashed line; (b) Partial p DOS of Te2 (Ag nearest neighbor), Te4 (away from Ag impurity), and Te in bulk PbTe; (d) Partial p DOS of Te2 (Sb nearest neighbor), Te4 (away from Sb impurity), and Te in bulk PbTe.

its Te nearest neighbors (Te2) atoms have the highest contribution to these resonant states (Fig. 6.10d). The Sb p states hybridize with Pb p and Te p states in the range (-0.25,2.5)eV. The interaction through hybridization between the Sb p and Te2 p resonant states with the Pb p states dramatically change the CB bottom Pb p states, which are pushed down in energy into the PbTe gap (see discussion of the band structure).

Bader analysis of the electronic charge for the single Ag impurity show ionic states of $Ag^{+0.23}$ and $Te2^{-0.56}$, whereas for Sb single impurity ionic states of $Sb^{+0.47}$ and $Te2^{-0.58}$ for the Ag(Sb) impurity and its nearest neighbors Te atoms. [3] These ionic states are very different from those assumed in the pure ionic model (Ag^{+1}, Sb^{+3} and Te^{-2}) suggesting

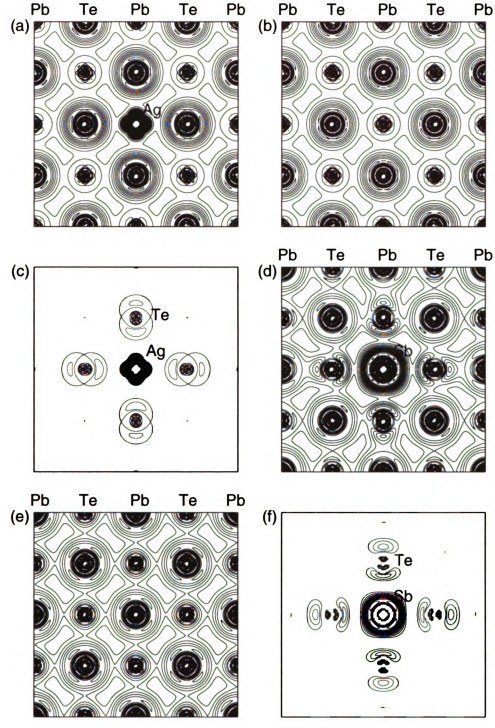

Figure 6.11: VB electronic charge density plots in plane perpendicular to [001] direction in the (-1,0.25)eV energy range for (a) Ag single impurity, (b) bulk PbTe, and (c) difference between Ag single impurity and bulk PbTe . CB electronic charge density plots in plane perpendicular to [001] direction in the (-0.5,2)eV energy range for (e) Sb single impurity, (b) bulk PbTe, and (c) difference between Sb single impurity and bulk PbTe . The charge density is represented by closed lines from low charge density regions (0 electrons/$\AA^3$) to high charge density regions (0.5 electrons/$\AA^3$) in steps of 0.01 electrons/$\AA^3$.

a strong covalent interaction between Sb and Te atoms. Also this analysis suggests some covalent interaction between Ag and Te atoms and screening of the Ag^+ ion. We also have plotted the valence band charge density in the (-1,0.25)eV energy range for the Ag single impurity, bulk PbTe and the difference between these two electronic charge densities (Fig 6.11a,b,c). Similarly for the Sb single impurity we have plotted the conduction band charge density in the (-0.5,2)eV energy range in comparison with the conduction band charge density of bulk PbTe and the difference between these valence charge densities (Fig 6.11d,e,f). Ag impurity in PbTe acts as p-type dopant which give the Fermi energy bellow the top of the VB (Fig. 6.10a), whereas Sb impurity acts as n-type dopant which gives the Fermi energy above the bottom of the CB (Fig. 6.10c). The energy ranges for the charge density plots are relative to the Fermi energies of the Ag and Sb impurities in PbTe. The charge density plots clearly show that the valence(conduction) electronic charge density associated with the Ag(Sb) single impurity is mostly localized on the Ag(Sb) impurity atom and its nearest neighbors Te atoms, consistent with the picture that these are deep defect levels. Both the VB states in the (-1,0.25)eV energy range and CB states in the (-0.5,2)eV energy range are antibonding states.

Results for isolated Ag-Sb pairs are consistent with the Ag(Sb) single impurity results in the sense that Ag introduces new states near the top of the VB, whereas Sb introduces new states near the bottom of the CB (Fig. 6.12). The latter interacts with the Pb p states near the bottom of the CB, thereby decreasing the PbTe gap. Both cases (Ag-Sb far apart and Ag-Sb next nearest neighbors, not shown in Fig. 6.9) show semiconducting behavior with a very small gap and a more rapidly increasing DOS near VB and CB extrema as

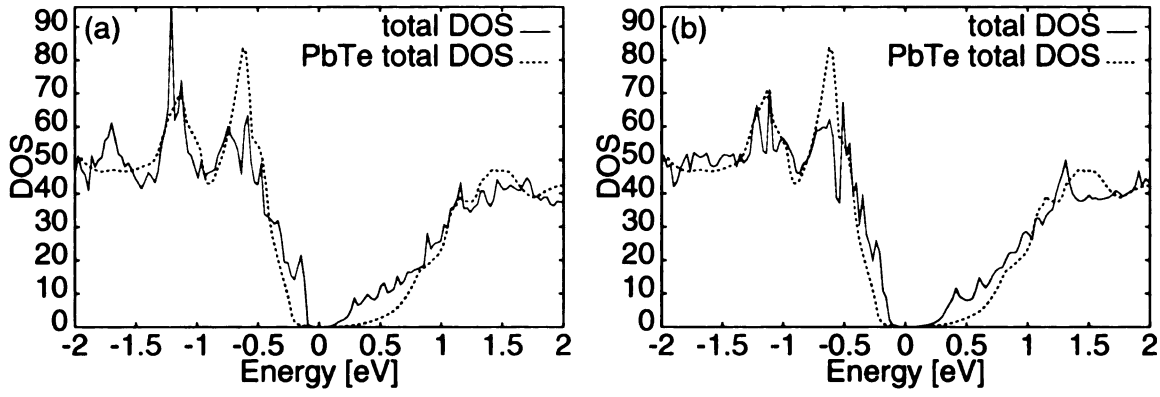

Figure 6.12: Total DOS of (a) Ag-Sb pair impurity with the Ag-Sb distance of ~11.19Å, and (b) Ag-Sb pair impurity with Ag-Sb distance of ~4.57Å, in PbTe. For comparison the total DOS of bulk PbTe is shown in dashed line.

compared to the DOS of PbTe. The specific features of the DOS in the gap region are very different for these two cases. Total energy comparison for $AgSbPb_{30}Te_{32}$ shows that these two structures are very close in energy, the case when Ag-Sb atoms are far apart has a slightly lower energy by ~20meV/(unit cell), indicating a covalency induced repulsion between Ag and Sb atoms.

It is interesting to compare the DOS results for different layered structures of Ag-Sb (Fig. 6.9b,c). When the Ag-Sb layer is perpendicular to the [001] direction, the states associated with the Ag-Sb layer completely fill the PbTe gap giving a semimetallic behavior (Fig. 6.13a), whereas the Ag-Sb layer perpendicular to [111] direction shows a semiconducting behavior (Fig. 6.13b). This indicates that the electronic structure of LAST-m systems and consequently their electronic properties are very sensitive to the microstructures. The Ag-Sb chain model shows semiconducting behaviour (Fig. 6.13c). This chain model has the same stoichiometry ($AgSbPb_{30}Te_{32}$) as the Ag-Sb pair impurity models. Total energy comparisons show that the chain model has a lower energy by 0.2eV/(unit cell) than the Ag-Sb pair impurity models, suggesting that Ag-Sb chain orderings along

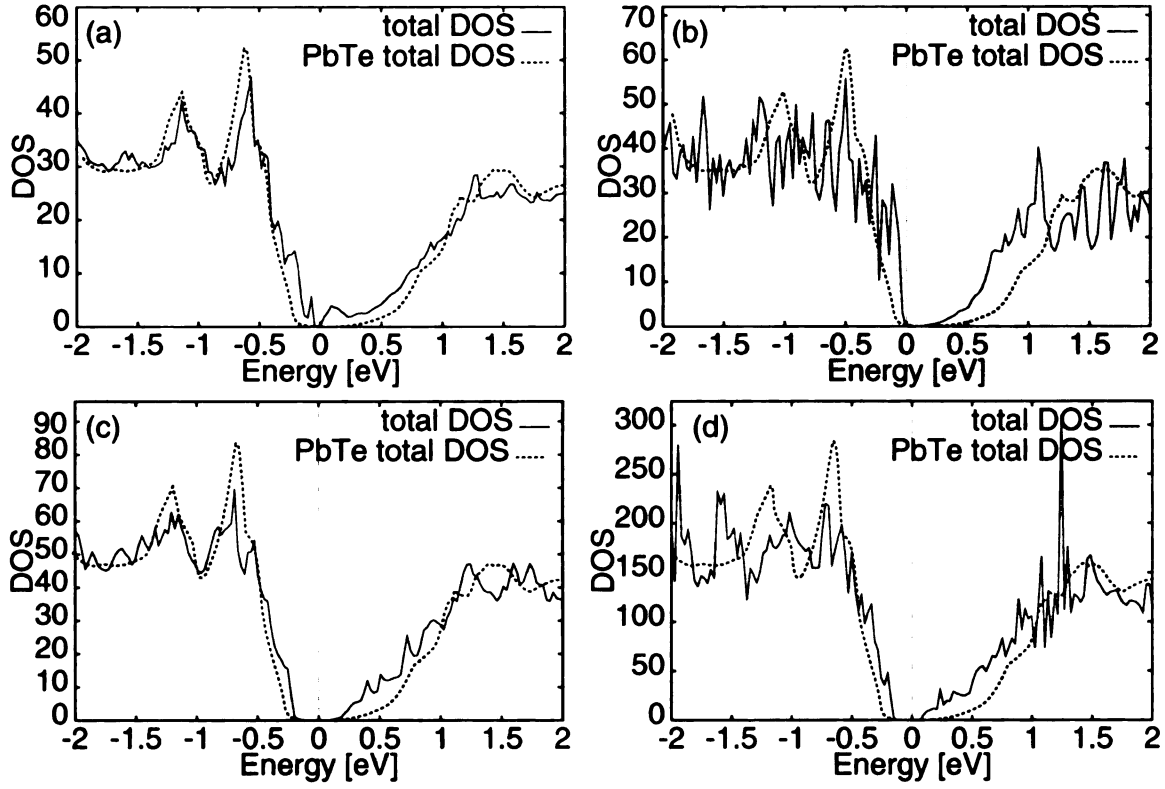

Figure 6.13: Total DOS of (a) Ag-Sb layer model perpendicular to [001] direction, (b) Ag-Sb layer model perpendicular to [111] direction, (c) Ag-Sb chain model, and (d) Ag-Sb cluster model. The total DOS of bulk PbTe is shown in dashed line.

[001] directions are favorable microstructures. This is consistent with some of the results of electron crystallographic studies which indicate the presence of Ag-Sb chains in the crystal. [30] The DOS results for the "$AgSbTe_2$" cluster model show also semiconductor behavior (Fig. 6.13d).

Next, we would like to see how the PbTe band structure ($\epsilon_{\vec{k}}$vs$\vec{k}$) is affected by the microstructural arrangements of Ag-Sb pairs. To see these differences we also plotted the PbTe band structure in the simple cubic (sc) Brillouin zone given in Fig. 6.14a. The band structures for bulk PbTe, Ag-Sb chain model, Ag-Sb pair impurity with the Ag-Sb distance of $\sim$11.19Å, and Ag-Sb layer model perpendicular to the [111] direction are shown in Fig. 6.15. In sc Brillouin zone the CBM and the VBM of bulk PbTe occur at the Γ point,

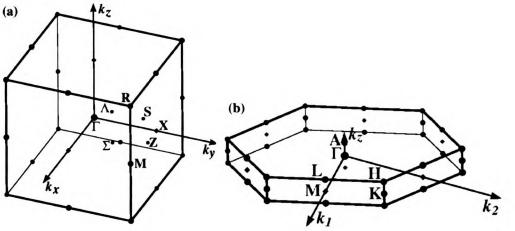

Figure 6.14: (a) Simple cubic Brillouin zone, (b) hexagonal Brillouin zone.

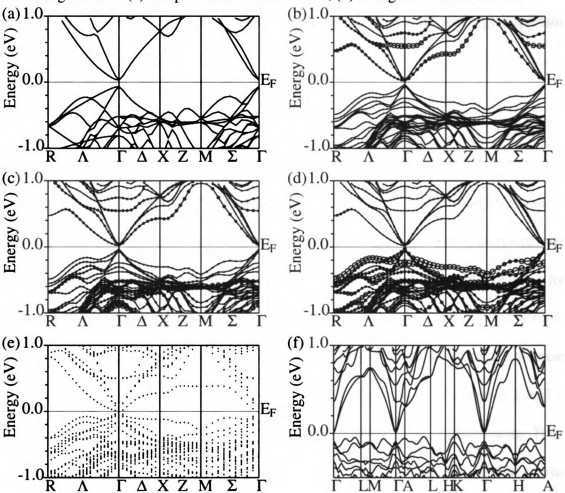

Figure 6.15: (a) Band structure in simple cubic Brillouin zone (see Fig. 6.14a) of (a) bulk PbTe, (b)-(d) Ag-Sb chain model; orbital character of (b) Sb p, (c) Te5 p (Sb nearest neighbor), and (d) Te6 p (Ag nearest neighbor), (e) Ag-Sb pair impurity with the Ag-Sb distance of ~11.19Å. Band structure in hexagonal Brillouin zone (see Fig. 6.14b) of (f) Ag-Sb layer model perpendicular to the [111] direction.

which is the same as the L point in the fcc Brillouin zone. For the Ag-Sb chain model and the Ag-Sb pair impurity model with the Ag-Sb distance of $\sim$11.19Å, the CBM and VBM occur at the Γ point. For Ag-Sb layer model perpendicular to the [111] direction, the CBM occurs at the Γ point, while the VBM occurs along the ΓK direction giving an indirect narrow band-gap semiconductor. Comparison of the chain model band structure (Fig. 6.14b) with that of PbTe (Fig. 6.14a) reveals that a new Sb resonant flat band appears at $\sim$0.6eV in the CB of PbTe. This new resonant band hybridize with the Pb p bands near the bottom of CB, which are pushed down in energy and having a flatter energy dispersion.

6.4.4 Summary

Ab initio electronic structure calculations give a clear picture of the deep defect states in PbTe when nominally divalent Pb ion is substituted by Ag (monovalent) and Sb (trivalent) ions. Supercell calculations for isolated Ag and Sb impurities and different microstructural arrangements of Ag-Sb show a generic feature; when Sb atoms replace Pb atoms, Sb hybridizes with neighboring Te atoms giving a very flat resonant band in the CB and forming strong covalent interactions. When Ag replaces Pb, the p states of Te which are the nearest neighbors of Ag are strongly perturbed. Therefore the electronic structure of LAST-m compounds depend sensitively on these Te p states perturbed by the Ag(Sb) atoms. These deep defect states appear near the top of the valence band (for monovalent Ag) and overlap with the PbTe conduction band (for trivalent Sb). In the latter case they are clearly resonant states.

We find that the details of the DOS near the band gap of LAST-m compounds depend

sensitively on the microstructural arrangements of Ag-Sb pairs in PbTe. The nature of the states near the top of the VB and bottom of the CB in these quaternary compounds is substantially different from those in PbTe. The common feature of these Ag-Sb arrangements is that they have a more rapidly increasing DOS near the gap as compared to bulk PbTe. Therefore, it is important to find out how these features in the DOS affect the electronic transport coefficients. It is well accepted that resonant structures in the DOS near Fermi energy, created by quantum size effects [27, 26, 28], superlattice engineering [98] or chemical means [58, 35, 36] are very desirable features because they could enhance the thermoelectric figure of merit ZT. This will be the subject of our studies in the next chapter.

Chapter 7

Electronic Transport in PbTe and $AgPb_mSbTe_{2+m}$ (LAST-m)

7.1 General Introduction

Electronic structure calculations of $AgPb_mSbTe_{2+m}$ (LAST-m) systems, described in the previous chapter, have revealed that these systems have an enhanced density of states (DOS) near the gap as compared to the bulk PbTe due to the appearance of distinct resonant states. Therefore, it is important to know how these features in the DOS affect the electronic transport properties such as electrical conductivity σ and thermopower S, the two quantities which define the power factor PF ($PF=\sigma S^2$). Also, it is important to understand why LAST-m systems show better thermoelectric properties than PbTe.

In order to answer the above questions and also to see how well the theory can describe quantitatively the transport coefficients, I have performed finite temperature elec-

tronic transport calculations in PbTe and LAST-m systems. These calculations were performed using Boltzmann transport equations and nonparabolic Kane model for the energy dispersion $\epsilon_{\vec{k}}$vs$\vec{k}$. [75] Also, the energy dispersion given by *ab initio* electronic structure calculations have been used in some transport calculations.

7.2 Boltzmann Transport Equation

The charge carriers in a metal or a semiconductor move under an applied external field and temperature gradient. We consider the situation where the carriers are accelerated by the fields, but lose their extra energy and momentum by scattering from lattice waves (phonons) and impurities. A standard method used to deal with this problem is to use Boltzmann transport equation. [104] This equation states that in a steady state situation, at any point in space $\vec{r}$ and for any value of the electronic wave vector $\vec{k}$, the net rate of change of $f_{\vec{k}}(\vec{r},t)$ is zero, where $f_{\vec{k}}(\vec{r},t)$ is the probability that an electron(hole) of wave vector $\vec{k}$ is at point $\vec{r}$ in the crystal. Then:

$$\left[\frac{\partial f_{\vec{k}}(\vec{r})}{\partial t}\right]_{diff.} + \left[\frac{\partial f_{\vec{k}}(\vec{r})}{\partial t}\right]_{field.} + \left[\frac{\partial f_{\vec{k}}(\vec{r})}{\partial t}\right]_{scatt.} = 0 \quad , \tag{7.1}$$

where the different contributions to the change are due the diffusion, external fields and scattering. As described above eq. 7.1 is valid for the steady-state, not for equilibrium ($f_{\vec{k}}(\vec{r},t)$=$f^0_{\vec{k}}(\vec{r},t)$) which holds in the absence of external fields. $f^0_{\vec{k}}(\vec{r})$ is the equilibrium single particle Fermi distribution function, the $\vec{r}$ dependence comes through the local temperature T($\vec{r}$). It is given by:

$$f^0_{\vec{k}}(\vec{r}) = \frac{1}{exp\left(\frac{\epsilon_{\vec{k}}-\mu}{K_B T(\vec{r})}\right)+1} \quad , \tag{7.2}$$

where $\epsilon_{\vec{k}}$ is the energy, μ is the chemical potential, K_B is the Boltzmann constant. For simplicity we will ignore the spin index and assume that each state $\vec{k}$ is two-fold spin degenerate since we do not consider magneto transport.

Assuming Liouville's theorem of the invariance of volume occupied in phase space, one finds that the number of carriers in the neighborhood of $\vec{r}$ at time t is equal to those in the neighborhood of $\vec{r} - t\vec{v}_{\vec{k}}$ at time zero:

$$f_{\vec{k}}(\vec{r}, t) = f_{\vec{k}}(\vec{r} - t\vec{v}_{\vec{k}}, 0) \quad . \tag{7.3}$$

The rate of change of the distribution function due to diffusion can be written as:

$$\left[\frac{\partial f_{\vec{k}}(\vec{r})}{\partial t}\right]_{diff.} = -\frac{\partial \vec{r}}{\partial t}\frac{\partial f_{\vec{k}}}{\partial \vec{r}(T)} = -\vec{v}_{\vec{k}}\frac{\partial f_{\vec{k}}}{\partial T}\nabla T \quad . \tag{7.4}$$

Using the definition of Fermi distribution function the derivative with respect to temperature in Eq. 7.4 can be rewritten as:

$$\frac{\partial f_{\vec{k}}}{\partial T} = \frac{exp\left(\frac{\epsilon_{\vec{k}}-\mu}{K_B T}\right)}{\left[exp\left(\frac{\epsilon_{\vec{k}}-\mu}{K_B T}\right)+1\right]^2}\frac{\epsilon_{\vec{k}}-\mu}{K_B T^2} = \left(-\frac{\partial f_{\vec{k}}}{\partial \epsilon_{\vec{k}}}\right)\frac{\epsilon_{\vec{k}}-\mu}{T} \quad , \tag{7.5}$$

and then the rate of change of the distribution function due to diffusion is given by:

$$\left[\frac{\partial f_{\vec{k}}(\vec{r})}{\partial t}\right]_{diff.} = \left(-\frac{\partial f_{\vec{k}}}{\partial \epsilon_{\vec{k}}}\right)\frac{\epsilon_{\vec{k}} - \mu}{T}\vec{v}_{\vec{k}}(-\nabla T) \quad . \tag{7.6}$$

By analogy to Eq. 7.3 we can apply Liouville's theorem in $\vec{k}$-space:

$$f_{\vec{k}}(\vec{r}, t) = f_{\vec{k}-\dot{\vec{k}}t}(\vec{r}, 0) \quad . \tag{7.7}$$

Considering only electric field $\vec{E}$ as the external field, the time rate of change of the Bloch wave vector $\vec{k}$ is given by:

$$\hbar\dot{\vec{k}} = e\vec{E} \quad . \tag{7.8}$$

The velocity of the electron in the state $\vec{k}$ is given by:

$$\hbar\vec{v}_{\vec{k}} = \frac{\partial \epsilon_{\vec{k}}}{\partial \vec{k}} \quad . \tag{7.9}$$

In Eqs. 7.8 and 7.9, e is electronic charge, m is free electron mass, and $\hbar = h/2\pi$ with h being the Planck constant. The rate of change of the distribution function due to the field can be written as:

$$\left[\frac{\partial f_{\vec{k}}(\vec{r})}{\partial t}\right]_{field} = -\frac{\partial \vec{k}}{\partial t}\frac{\partial f_{\vec{k}}}{\partial \vec{k}} = -\dot{\vec{k}}\frac{\partial f_{\vec{k}}}{\partial \epsilon_{\vec{k}}}\frac{\partial \epsilon_{\vec{k}}}{\partial \vec{k}} = -\frac{e\vec{E}}{\hbar}\frac{\partial f_{\vec{k}}}{\partial \epsilon_{\vec{k}}}\hbar\vec{v}_{\vec{k}} = e\left(-\frac{\partial f_{\vec{k}}}{\partial \epsilon_{\vec{k}}}\right)\vec{v}_{\vec{k}}\vec{E} \quad . \tag{7.10}$$

The effect of scattering on the change in the distribution function is more complicated. In this thesis only the relaxation time approximation was considered. In the relaxation time

approximation the rate of change of the distribution function due to scattering is given by:

$$\left[\frac{\partial f_{\vec{k}}(\vec{r})}{\partial t}\right]_{scatt.} = -\frac{f_{\vec{k}} - f^0_{\vec{k}}}{\tau_{\vec{k}}} = -\frac{g_{\vec{k}}}{\tau_{\vec{k}}} \quad , \tag{7.11}$$

where $g_{\vec{k}}$ is the difference between the steady-state and equilibrium distribution functions, and $\tau_{\vec{k}}$ is the relaxation time.

Using the Eqs. 7.6, 7.10, and 7.11, the the Boltzmann transport equation (Eq. 7.1) can be written as:

$$g_{\vec{k}} = e\left(-\frac{\partial f_{\vec{k}}}{\partial \epsilon_{\vec{k}}}\right)\vec{v}_{\vec{k}}\tau_{\vec{k}}\vec{E} + \left(-\frac{\partial f_{\vec{k}}}{\partial \epsilon_{\vec{k}}}\right)\frac{\epsilon_{\vec{k}} - \mu}{T}\vec{v}_{\vec{k}}\tau_{\vec{k}}(-\nabla T) \quad . \tag{7.12}$$

In order to find the expressions for electrical conductivity tensor $\overleftrightarrow{\sigma}$ and thermopower tensor $\overleftrightarrow{S}$, the microscopic and macroscopic Ohm's laws have to be used, which relate the current density to the applied electric field and temperature gradient. The microscopic Ohm's law is given by:

$$\vec{J} = \frac{1}{V}\sum_{\vec{k}} e f_{\vec{k}}\vec{v}_{\vec{k}} = \frac{1}{V}\sum_{\vec{k}} e g_{\vec{k}}\vec{v}_{\vec{k}} \quad , \tag{7.13}$$

since

$$\sum_{\vec{k}} e f^0_{\vec{k}}\vec{v}_{\vec{k}} = 0 \quad , \tag{7.14}$$

where V is the volume of the crystal in real space. From Eq. 7.12 and Eq. 7.13, the current density can be expressed as:

$$\vec{J} = \frac{1}{V}\sum_{\vec{k}} e^2 \left(-\frac{\partial f_{\vec{k}}}{\partial \epsilon_{\vec{k}}}\right) \tau_{\vec{k}} \vec{v}_{\vec{k}} \vec{v}_{\vec{k}} \vec{E} + \frac{1}{V}\sum_{\vec{k}} e \left(-\frac{\partial f_{\vec{k}}}{\partial \epsilon_{\vec{k}}}\right) \frac{\epsilon_{\vec{k}} - \mu}{T} \tau_{\vec{k}} \vec{v}_{\vec{k}} \vec{v}_{\vec{k}} (-\nabla T) \quad , \quad (7.15)$$

$$\equiv \frac{1}{V}\sum_{\vec{k}} e^2 \left(-\frac{\partial f_{\vec{k}}}{\partial \epsilon_{\vec{k}}}\right) \tau_{\vec{k}} \vec{v}_{\vec{k}} \vec{v}_{\vec{k}} \left(\vec{E} + \frac{1}{eT} \frac{\sum_{\vec{k}} \left(-\frac{\partial f_{\vec{k}}}{\partial \epsilon_{\vec{k}}}\right) (\epsilon_{\vec{k}} - \mu) \tau_{\vec{k}} \vec{v}_{\vec{k}} \vec{v}_{\vec{k}}}{\sum_{\vec{k}} \left(-\frac{\partial f_{\vec{k}}}{\partial \epsilon_{\vec{k}}}\right) \tau_{\vec{k}} \vec{v}_{\vec{k}} \vec{v}_{\vec{k}}} (-\nabla T) \right) \quad (7.16)$$

The macroscopic Ohm's law in the presence of an external electric field $\vec{E}$ and temperature gradient ∇T is given by:

$$\vec{J} = \overleftrightarrow{\sigma} \vec{E} + \overleftrightarrow{\sigma} \overleftrightarrow{S} (-\nabla T) = \overleftrightarrow{\sigma} \left(\vec{E} + \overleftrightarrow{S} (-\nabla T) \right) \quad . \quad (7.17)$$

Direct comparison of the two Ohm's laws in Eqs. 7.16 and 7.17 gives the expressions for the electrical conductivity and thermopower tensors:

$$\overleftrightarrow{\sigma} = \frac{e^2}{V}\sum_{\vec{k}} \left(-\frac{\partial f_{\vec{k}}}{\partial \epsilon_{\vec{k}}}\right) \tau_{\vec{k}} \vec{v}_{\vec{k}} \vec{v}_{\vec{k}} \quad (7.18)$$

$$\overleftrightarrow{S} = (\overleftrightarrow{\sigma})^{-1} \overleftrightarrow{A} \quad , \quad (7.19)$$

where $\overleftrightarrow{A}$ is given by:

$$\overleftrightarrow{A} = \frac{e}{VT}\sum_{\vec{k}} \left(-\frac{\partial f_{\vec{k}}}{\partial \epsilon_{\vec{k}}}\right) (\epsilon_{\vec{k}} - \mu) \tau_{\vec{k}} \vec{v}_{\vec{k}} \vec{v}_{\vec{k}} \quad . \quad (7.20)$$

Analogous to the current density equations, the microscopic and macroscopic heat density equations for $\vec{J}_Q$ can be written as:

$$\vec{J}_Q = \frac{1}{V}\sum_{\vec{k}} f_{\vec{k}}(\epsilon_{\vec{k}} - \mu)\vec{v}_{\vec{k}} = \frac{1}{V}\sum_{\vec{k}} g_{\vec{k}}(\epsilon_{\vec{k}} - \mu)\vec{v}_{\vec{k}} \tag{7.21}$$

$$\equiv \overleftrightarrow{\sigma}\overleftrightarrow{S}T\vec{E} + \overleftrightarrow{\kappa}_0(-\nabla T) \quad , \tag{7.22}$$

where $\overleftrightarrow{\kappa_0}$ is the electronic thermal conductivity tensor at constant $\vec{E}$ field ($\vec{E}$=0). Direct comparison of the two heat density equations gives the expression for the electronic thermal conductivity tensor at constant $\vec{E}$ field ($\vec{E}$=0):

$$\overleftrightarrow{\kappa}_0 = \frac{1}{VT^2}\sum_{\vec{k}}\left(-\frac{\partial f_{\vec{k}}}{\partial \epsilon_{\vec{k}}}\right)(\epsilon_{\vec{k}} - \mu)^2 \vec{v}_{\vec{k}}\vec{v}_{\vec{k}}\tau_{\vec{k}} \quad . \tag{7.23}$$

It should be pointed out that one is sometimes interested in constant $\vec{J}$ ($\vec{J}$=0) electronic thermal conductivity which requires solving simultaneously Eqs. 7.17 and 7.22 for $\overleftrightarrow{\kappa}$ with the constraint $\vec{J}$=0. This thermal conductivity is usually referred as $\overleftrightarrow{\kappa}_{el}$. [58]

7.3 Nonparabolic Kane Model for Energy Dispersion

In this section I will discuss a simple model for the band structure of PbTe. In narrow band-gap semiconductors (*i.e.* lead chalcogenides) the energy of an electron, measured from the band edge, is comparable with the energy gap E_g between the conduction and valence bands. Because of this, the dependence of the energy on crystal momentum is nonquadratic and the effective masses are functions of the energy. The nonparabolic Kane model was introduced to describe the nonparabolic dependence of energy on the crystal momentum $\vec{k}$. [75] In this model, the longitudinal effective mass m_l and the transverse effective mass

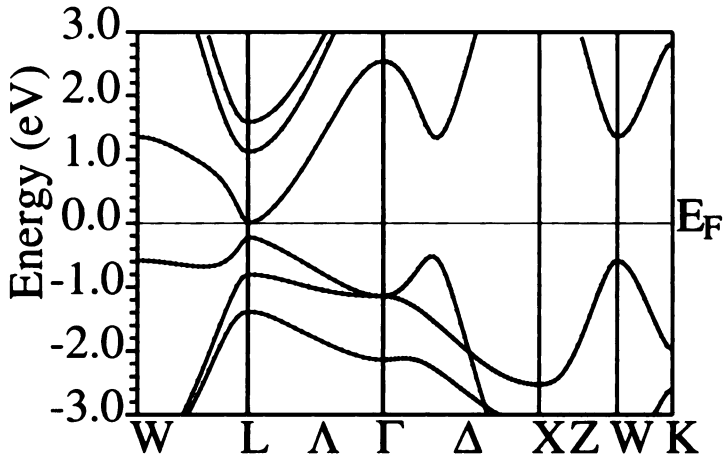

Figure 7.1: Band structure of PbTe in face centered cubic Brillouin zone.

m_t depend only on the interaction between the lowest conduction band and the highest valence band and the contributions of other bands are assumed to be small. In Fig. 7.1 the band structure of PbTe is shown. The conduction band minimum and the valence band maximum in PbTe occur at the L[1/2,1/2,1/2] point in units of the primitive face centered cubic reciprocal lattice $\vec{k}$ vectors. The longitudinal effective mass m_l is defined along the LΓ direction in the Brillouin zone, whereas the transverse effective mass m_t is defined along the perpendicular direction to LΓ. For the simple parabolic model the energy dispersion can be expressed as:

$$\epsilon_{\vec{k}} = \frac{\hbar^2}{2}\left(\frac{2k_t^2}{m_t} + \frac{k_l^2}{m_l}\right) \quad , \tag{7.24}$$

where $\epsilon_{\vec{k}}$ is the energy, k_l and k_t are the magnitudes of the longitudinal and transverse components of $\vec{k}$ (measured from the L point). In the Kane model the energy dispersion is given by:

$$\epsilon_{\vec{k}}\left(1+\frac{\epsilon_{\vec{k}}}{E_g}\right)=\frac{\hbar^2}{2}\left(\frac{2k_t^2}{m_t}+\frac{k_l^2}{m_l}\right) \quad . \tag{7.25}$$

In this model the effective masses and the mass anisotropy coefficient of electrons and holes are equal. The constant energy surfaces are ellipsoids and m_l and m_t have the same energy dependence.

7.4 Transport Coefficients in the Kane Model

In order to calculate the transport coefficients we have to compute different quantities appearing in Eqs. 7.18, 7.19, and 7.23, which include the carrier velocity $\vec{v}_{\vec{k}}$ and the relaxation time $\tau_{\vec{k}}$. For this, we change the discrete sums over $\vec{k}$ into integrals, the carrier velocity $\vec{v}_{\vec{k}}$ is calculated using the Kane model for the energy dispersion, and the relaxation time expressions for different scattering mechanisms are obtained within Kane model. These expressions are given in the section 7.5.

PbTe and LAST-m systems have cubic symmetry. Therefore, the components $\sigma_{\mu\nu}$ and $S_{\mu\nu}$ of the electrical conductivity and thermopower tensors can be express as:

$$\sigma_{\mu\nu}=\delta_{\mu\nu}\sigma \quad , \tag{7.26}$$

$$S_{\mu\nu}=\delta_{\mu\nu}S \quad , \tag{7.27}$$

where σ and S are related to the trace of $\overleftrightarrow{\sigma}$ and $\overleftrightarrow{S}$ tensors and they are given by:

$$\sigma = \frac{1}{3} Tr \overleftrightarrow{\sigma} \quad , \tag{7.28}$$

$$S = \frac{1}{3} Tr \overleftrightarrow{S} \quad . \tag{7.29}$$

$Tr \overleftrightarrow{\sigma}$ and $Tr \overleftrightarrow{S}$ are related to $\vec{v}_{\vec{k}} \vec{v}_{\vec{k}} = v_{\vec{k}}^2$ terms.

The Kane model energy dispersion Eq. 7.25 contains two types of effective masses and in order to simplify the calculations the fallowing substitutions can be made:

$$k_t^2 = \frac{m_t}{m_d'} k_t'^2 \quad , \tag{7.30}$$

$$k_l^2 = \frac{m_l}{m_d'} k_l'^2 \quad . \tag{7.31}$$

Using the new variables k_l' and k_t', Eq. 7.25 can be written as:

$$\epsilon_{k'} \left(1 + \frac{\epsilon_{k'}}{E_g} \right) = \frac{\hbar^2}{2m_d'} \left(2k_t'^2 + k_l'^2 \right) \equiv \frac{\hbar^2}{2m_d'} k'^2 \quad . \tag{7.32}$$

In terms of the new variable $\vec{k'}$ the expressions for $\overleftrightarrow{\sigma}$ and $\overleftrightarrow{S}$ are:

$$\overleftrightarrow{\sigma} = \frac{e^2}{V} \sum_{\vec{k'}} \left(-\frac{\partial f_{\vec{k'}}}{\partial \epsilon_{\vec{k'}}} \right) \tau_{\vec{k'}} \vec{v}_{\vec{k'}} \vec{v}_{\vec{k'}} \tag{7.33}$$

$$\overleftrightarrow{S} = (\overleftrightarrow{\sigma})^{-1} \overleftrightarrow{A} \quad , \tag{7.34}$$

where $\overleftrightarrow{A}$ is given by:

$$\overleftrightarrow{A} = \frac{e}{VT}\sum_{\vec{k'}}\left(-\frac{\partial f_{\vec{k'}}}{\partial \epsilon_{\vec{k'}}}\right)(\epsilon_{\vec{k'}} - \mu)\tau_{\vec{k'}}\vec{v}_{\vec{k'}}\vec{v}_{\vec{k'}} \quad . \tag{7.35}$$

Changing the sums into integrals, Eq. 7.34 for thermopower becomes:

$$\overleftrightarrow{S} = \frac{1}{eT}\frac{\int_0^\infty \left(-\frac{\partial f_{\vec{k'}}}{\partial \epsilon_{\vec{k'}}}\right)(\epsilon_{\vec{k'}} - \mu)\tau_{\vec{k'}}\vec{v}_{\vec{k'}}\vec{v}_{\vec{k'}}d^3\vec{k'}}{\int_0^\infty \left(-\frac{\partial f_{\vec{k'}}}{\partial \epsilon_{\vec{k'}}}\right)\tau_{\vec{k'}}\vec{v}_{\vec{k'}}\vec{v}_{\vec{k'}}d^3\vec{k'}} \quad . \tag{7.36}$$

Using Eq. 7.32, the infinitesimal unit volume in reciprocal space $d^3\vec{k'}$ can be expressed as:

$$d^3\vec{k'} = 4\pi k'^2 dk' = 4\pi\frac{2^{\frac{1}{2}}m_d'^{\frac{3}{2}}}{\hbar^3}\left[\epsilon\left(1+\frac{\epsilon}{E_g}\right)\right]^{\frac{1}{2}}\left(1+\frac{2\epsilon}{E_g}\right)d\epsilon \quad , \tag{7.37}$$

where we have dropped the suffix for the carrier energy $\epsilon_{\vec{k'}}$.

The carrier velocity defined in Eq. 7.9 is given by:

$$\vec{v}_{\vec{k'}} = \frac{1}{\hbar}\frac{\partial \epsilon}{\partial \epsilon_{\vec{k'}}} = \frac{\hbar}{m_d'}\frac{\vec{k'}}{1+\frac{2\epsilon}{E_g}} \quad . \tag{7.38}$$

Using the above equation, the $v^2_{\vec{k'}}$=$\vec{v}_{\vec{k'}}\cdot\vec{v}_{\vec{k'}}$ term in the transport equations can be expressed as:

$$v^2_{\vec{k'}} = \frac{2}{m_d'}\frac{\epsilon\left(1+\frac{\epsilon}{E_g}\right)}{\left(1+\frac{2\epsilon}{E_g}\right)^2} \quad . \tag{7.39}$$

Substituting Eqs. 7.37 and 7.39 into Eq. 7.36 and using Eqs. 7.27 and 7.29, the thermopower along the x-axis S_{xx} (S_{xx}=S) becomes:

$$S_{xx} = \frac{1}{eT} \frac{\int_0^\infty \left(-\frac{\partial f}{\partial \epsilon}\right)(\epsilon - \mu)\left[\epsilon\left(1+\frac{\epsilon}{E_g}\right)\right]^{\frac{3}{2}}\left(1+\frac{2\epsilon}{E_g}\right)^{-1}\tau_\epsilon d\epsilon}{\int_0^\infty \left(-\frac{\partial f}{\partial \epsilon}\right)\left[\epsilon\left(1+\frac{\epsilon}{E_g}\right)\right]^{\frac{3}{2}}\left(1+\frac{2\epsilon}{E_g}\right)^{-1}\tau_\epsilon d\epsilon} \quad , \tag{7.40}$$

where the relaxation time τ_ϵ is assumed to depend only on energy. Since S depends on the ratio of the two integrals (Eq. 7.36) the spin and band degeneracy γ factors cancel out in Eqs. 7.36 and 7.40.

Taking into account the spin degeneracy and the band degeneracy γ, the expression for the electrical conductivity $\overleftrightarrow{\sigma}$ can be rewritten as:

$$\overleftrightarrow{\sigma} = \frac{2\gamma e^2}{V}\sum_{\vec{k'}}\left(-\frac{\partial f_{\vec{k'}}}{\partial \epsilon_{\vec{k'}}}\right)\vec{v}_{\vec{k'}}\vec{v}_{\vec{k'}}\tau_{\vec{k'}} = \frac{2\gamma e^2}{V}\frac{V}{(2\pi)^3}\int_0^\infty \left(-\frac{\partial f_{\vec{k'}}}{\partial \epsilon_{\vec{k'}}}\right)\vec{v}_{\vec{k'}}\vec{v}_{\vec{k'}}\tau_{\vec{k'}} d^3\vec{k'} \quad , \tag{7.41}$$

and using Eqs. 7.37 and 7.39, $Tr\overleftrightarrow{\sigma}$ can be expressed as:

$$Tr\sigma = 2\gamma e^2 \frac{(2m'_d)^{\frac{1}{2}}}{\pi^2\hbar^3}\int_0^\infty \left(-\frac{\partial f}{\partial \epsilon}\right)\left[\epsilon\left(1+\frac{\epsilon}{E_g}\right)\right]^{\frac{3}{2}}\left(1+\frac{2\epsilon}{E_g}\right)^{-1}\tau_\epsilon d\epsilon \quad . \tag{7.42}$$

In order to compare the electrical conductivity with the measured experimental values along a specific crystallographic direction (*e. i.* x-axis), the component σ_{xx} has to be calculated. σ_{xx} (σ_{xx}=σ) is given by:

$$\sigma_{xx} = \frac{2}{3}\gamma e^2 \frac{(2m'_d)^{\frac{1}{2}}}{\pi^2\hbar^3} \int_0^\infty \left(-\frac{\partial f}{\partial \epsilon}\right) \left[\epsilon\left(1+\frac{\epsilon}{E_g}\right)\right]^{\frac{3}{2}} \left(1+\frac{2\epsilon}{E_g}\right)^{-1} \tau_\epsilon d\epsilon \quad . \tag{7.43}$$

The concentration of carriers n can be written as:

$$n = \frac{2\gamma}{V}\sum_{\vec{k'}} f_{\vec{k'}} = \frac{2\gamma}{V}\frac{V}{(2\pi)^3}\int \frac{d^3\vec{k'}}{exp\left(\frac{\epsilon_{\vec{k'}}-\mu}{K_B T}\right)+1} \quad , \tag{7.44}$$

and using Eq. 7.37 the concentration n can be expressed as:

$$n = \frac{2^{\frac{1}{2}}}{\pi^2\hbar^3}\gamma m_d'^{\frac{3}{2}} \int_0^\infty \frac{\left[\epsilon\left(1+\frac{\epsilon}{E_g}\right)\right]^{\frac{1}{2}}\left(1+\frac{2\epsilon}{E_g}\right)d\epsilon}{exp\left(\frac{\epsilon-\mu}{K_B T}\right)+1} \quad . \tag{7.45}$$

The expression $\gamma m_d'^{3/2}$ is defined as:

$$m_d^{3/2} = \gamma m_d'^{3/2} \quad , \tag{7.46}$$

where m_d is called density of states effective mass. The relation between the density of states effective mass and longitudinal and transverse effective masses can be deduced using the Eqs. 7.30, 7.31 and the following equation:

$$d^3\vec{k} = d^3\vec{k'} \quad , \tag{7.47}$$

which sets the equality between the infinitesimal volumes in reciprocal space. Then the density of states effective mass can be expressed as:

$$m_d = \gamma^{\frac{2}{3}} m'_d = \gamma^{\frac{2}{3}} \left(m_l m_t^2 \right)^{\frac{1}{3}} \quad . \tag{7.48}$$

The transport coefficients can be expressed in terms of generalized Fermi integrals:

$${}^n L_l^m(\mu, E_g) = \int_0^\infty \left(-\frac{\partial f}{\partial \epsilon} \right) (\epsilon)^n \left[\epsilon \left(1 + \frac{\epsilon}{E_g} \right) \right]^m \left(1 + \frac{2\epsilon}{E_g} \right)^l d\epsilon \quad . \tag{7.49}$$

In the case of constant relaxation time τ_ϵ=τ_0 independent of energy ϵ, the expressions for thermopower, electrical conductivity and concentration have a simplified form:

$$S_{xx} = \frac{K_B}{e} \left(\frac{{}^1 L_{-1}^{\frac{3}{2}}(\mu, E_g)}{{}^0 L_{-1}^{\frac{3}{2}}(\mu, E_g)} - \mu \right) \quad , \tag{7.50}$$

$$\sigma_{xx} = \frac{2}{3} \gamma e^2 \frac{(2m'_d)^{\frac{1}{2}} \tau_0}{\pi^2 \hbar^3} \left({}^0 L_{-1}^{\frac{3}{2}}(\mu, E_g) \right) \quad , \tag{7.51}$$

$$n = \frac{1}{3} \gamma \frac{(2m'_d)^{\frac{3}{2}}}{\pi^2 \hbar^3} \left({}^0 L_0^{\frac{3}{2}}(\mu, E_g) \right) \quad . \tag{7.52}$$

Note that in this limit S_{xx} is independent of the relaxation time and systems with large differences in σ_{xx} can have nearly the same S_{xx}.

7.5 Relaxation Times in the Kane Model

Different scattering mechanisms of charge carriers in lead chalcogenides have been intensively studied in many papers. [75, 77, 76, 103, 20] It is found that the dominant scattering

mechanisms are by point defects and by thermal phonons and their relative contributions to the scattering processes are summarized below.

At low temperatures (liquid helium), charge carriers are scattered mostly by charged vacancies. At low densities $n \leq 5\text{x}10^{18}$ cm^{-3}, scattering by Coulomb potential of the vacancies dominates, whereas for high carrier densities $n \geq 10^{19}$ cm^{-3}, the Coulomb potential gets screened out and scattering by the short range potential of vacancies dominates.

As the temperature increases, the relative importance of the charged vacancies in scattering mechanisms decreases as the scattering by thermal phonons increases. For temperatures above 300K the scattering by acoustic phonons and optical phonons (both polar and deformation potential) have the main contribution to the relaxation time.

Calculations for the transport coefficients are made at temperatures above 300K , at which all scattering mechanisms which are important in PbTe can be described in relaxation time approximation. The expressions for the dominant contributions to the relaxation time taking into account the band nonparabolicity in PbTe within the Kane model, have the following forms [77, 103, 20]:

I) Deformation potential of acoustic phonons (τ_a):

$$\tau_a = \frac{\tau_{0,a}(T)\left(\epsilon + \frac{\epsilon^2}{E_g}\right)^{-\frac{1}{2}}}{\left(1+2\frac{\epsilon}{E_g}\right)\left[(1-A)^2 - B\right]} \quad , \tag{7.53}$$

$$A = \frac{\frac{\epsilon}{E_g}(1-K_a)}{\left(1+2\frac{\epsilon}{E_g}\right)} \quad , \tag{7.54}$$

$$B = \frac{8\frac{\epsilon}{E_g}\left(1+\frac{\epsilon}{E_g}\right)K_a}{3\left(1+2\frac{\epsilon}{E_g}\right)^2} \tag{7.55}$$

$$\tau_{0,a}(T) = \frac{2\pi\hbar^4 C_l}{E_{ac}^2 K_B T (2m_{d0})^{\frac{3}{2}}} \quad , \tag{7.56}$$

where E_{ac} is the acoustic deformation potential coupling constant for the conduction band, C_l is a combination of elastic constants, K_a is the ratio of the acoustic deformation potential coupling constants for the valence and conduction bands $K_a = E_{av}/E_{ac}$ with the values K_a=1 for n-type PbTe and K_a=1.5 for p-type PbTe, and m_{d0} is the density of states effective mass for a single ellipsoid (γ=1).

II) Deformation potential of optical phonons (τ_o):

$$\tau_o = \frac{\tau_{0,o}(T)\left(\epsilon + \frac{\epsilon^2}{E_g}\right)^{-\frac{1}{2}}}{\left(1 + 2\frac{\epsilon}{E_g}\right)\left[(1-A)^2 - B\right]} \quad , \tag{7.57}$$

$$A = \frac{\frac{\epsilon}{E_g}(1 - K_o)}{\left(1 + 2\frac{\epsilon}{E_g}\right)} \quad , \tag{7.58}$$

$$B = \frac{8\frac{\epsilon}{E_g}\left(1 + \frac{\epsilon}{E_g}\right)K_o}{3\left(1 + 2\frac{\epsilon}{E_g}\right)^2} \tag{7.59}$$

$$\tau_{0,o}(T) = \frac{2\hbar^2 a^2 \rho(\hbar\omega_0)^2}{\pi E_{oc}^2 K_B T (2m_{d0})^{\frac{3}{2}}} \quad , \tag{7.60}$$

where a is the PbTe lattice constant, ρ is the PbTe density, ω_0 is the frequency of the optical phonons, K_o is the ratio of the optical deformation potential coupling constants for valence and conduction bands, $K_o = E_{ov}/E_{oc}$, which are taken to be the same as for acoustic phonons, K_a.

III) Polarization scattering by optical phonons (τ_{po}):

$$\tau_{po} = \frac{\hbar^2\left(\epsilon + \frac{\epsilon^2}{E_g}\right)^{\frac{1}{2}} F^{-1}}{e^2(2m_{d0})^{\frac{1}{2}} K_B T(\varepsilon_\infty^{-1} - \varepsilon_0^{-1})\left(1 + 2\frac{\epsilon}{E_g}\right)} \quad , \tag{7.61}$$

$$F = 1 - \delta\ln(1 + \delta^{-1}) - \frac{2\frac{\epsilon}{E_g}\left(1 + \frac{\epsilon}{E_g}\right)}{\left(1 + 2\frac{\epsilon}{E_g}\right)^2}\left[1 - 2\delta + 2\delta^2\ln(1 + \delta^{-1})\right] \quad , \tag{7.62}$$

$$\delta = (2kr_0)^{-2} \quad , \tag{7.63}$$

where ε_0 and ε_∞ are the static and high frequency permittivities, k is the carrier wave

vector and r_0 is the screening length of the optical phonons. The parameters k and r_0 are given by:

$$k^2 = \frac{2m_{d0}\left(\epsilon + \frac{\epsilon^2}{E_g}\right)}{\hbar^2} \quad , \tag{7.64}$$

$$r_0^{-2} = \frac{2^{\frac{5}{2}} e^2 m_d^{\frac{3}{2}}}{\pi \hbar^3 \varepsilon_\infty} \left({}^0L_1^{\frac{1}{2}}\right) \quad . \tag{7.65}$$

IV) Short range deformation potential of vacancies (τ_v):

$$\tau_v = \frac{\tau_{0,v}(T)\left(\epsilon + \frac{\epsilon^2}{E_g}\right)^{-\frac{1}{2}}}{\left(1 + 2\frac{\epsilon}{E_g}\right)\left[(1-A)^2 - B\right]} \quad , \tag{7.66}$$

$$A = \frac{\frac{\epsilon}{E_g}(1 - K_v)}{\left(1 + 2\frac{\epsilon}{E_g}\right)} \quad , \tag{7.67}$$

$$B = \frac{8\frac{\epsilon}{E_g}\left(1 + \frac{\epsilon}{E_g}\right)K_v}{3\left(1 + 2\frac{\epsilon}{E_g}\right)^2} \quad , \tag{7.68}$$

$$\tau_{0,v}(T) = \frac{\pi \hbar^4}{U_{vc}^2 m_{d0}(2m_{d0})^{\frac{1}{2}} N_v} \quad , \tag{7.69}$$

where N_v is the vacancy density, K_v is the ratio of the short range deformation potential coupling constants of vacancies for valence and conduction bands, $K_v = U_{vv}/U_{vc}$, which are taken to be the same as for acoustic phonons, K_a.

IV) Coulomb potential of vacancies (τ_C):

$$\tau_C = \frac{\varepsilon_0^2 (2m_{d0})^{\frac{1}{2}} \left(\epsilon + \frac{\epsilon^2}{E_g}\right)^{\frac{3}{2}}}{\pi (Ze^2)^2 N_v \left[\ln(1+\xi) - \xi/(1+\xi)\right] \left(1 + 2\frac{\epsilon}{E_g}\right)} \quad , \tag{7.70}$$

$$\xi = (2kr_v)^2 \quad , \tag{7.71}$$

where Ze is the vacancy charge, and r_v is the screening radius of the vacancy potential given by:

$$r_v^{-2} = \frac{4\pi e^2}{\varepsilon_0} D(\mu) \quad , \tag{7.72}$$

$$D(\mu) = \frac{2^{\frac{1}{2}} (m_{d0})^{\frac{3}{2}}}{\pi^2 \hbar^3} \left(\mu + \frac{\mu^2}{E_g}\right)^{\frac{1}{2}} \left(1 + 2\frac{\mu}{E_g}\right) \quad , \tag{7.73}$$

$D(\mu)$ being the density of states at the chemical potential.

The total scattering relaxation time τ_ϵ is expressed as:

$$\frac{1}{\tau_\epsilon} = \frac{1}{\tau_a} + \frac{1}{\tau_o} + \frac{1}{\tau_{po}} + \frac{1}{\tau_v} + \frac{1}{\tau_C} \quad . \tag{7.74}$$

We find that only the first three terms in the above sum contribute at temperatures above 300K. The values of the relaxation times at room temperature in the 1-200meV energy range are: τ_a=0.15-2.9$\times 10^{-12}$s, τ_o=0.18-2.0$\times 10^{-12}$s, τ_{po}=0.1-0.19$\times 10^{-12}$s, τ_v=2.4-44.7$\times 10^{-12}$s, and τ_C=5.2-1216.0$\times 10^{-12}$s; τ_v and τ_C are orders of magnitudes larger than τ_a, τ_o and τ_{po}. The parameters used to calculate the relaxation times were taken from Ref. [103] and they are given in Table 7.1. Experimentally one finds the energy gap E_g and

Table 7.1: Parameters used to calculate the relaxation times for PbTe and LAST-m systems at 300K.

Parameter	Unit of measurement	Value
m_l/m		0.24
ε_0		400
ε_∞		32.6
C_l	N/m^2	$0.71x10^{11}$
$\hbar\omega_0$	eV	0.0136
a	Å	6.461
ρ	g/cm^3	8.24
Z		0.14
E_{ac}	eV	15
E_{oc}	eV	26
U_{vc}	ergs cm^3	$3x10^{-34}$
K_a, K_o, K_v for n-type		1.0
K_a, K_o, K_v for p-type		1.5

the density of states effective mass m_d to be temperature dependent. [94, 101] This comes from strong electron-phonon coupling. In our transport calculations we have incorporated the T-dependent E_g and m_d using experimental data. As it will be discussed later in detail, we found that the temperature dependence of m_d was very important to have good agreement with measured values of the transport coefficients. Experimentally it is found that E_g increases linearly with temperature for $T \leq$400K and above 400K, it remains constant. [94] The temperature dependence of $E_g(T)$ is given by:

$$E_g = 0.19 + (0.42 \times 10^{-3})T, for T \leq 400K \quad , \tag{7.75}$$

$$E_g = 0.356, for T > 400K \quad . \tag{7.76}$$

The temperature dependence of m_d (see Eq. 7.48) comes primarily through the T-

dependence of the transverse effective mass m_t, which is also taken from experiment [101]:

$$\frac{m_t}{m} = 0.02459 + (8.659341 \times 10^{-5})T \quad , \tag{7.77}$$

where m is the bare electron mass.

7.6 Transport Coefficients Using *ab initio* Electronic Structure

In order to calculate the concentration n, the electrical conductivity σ_{xx} and thermopower S_{xx} using *ab initio* electronic structure results, the sums in Eqs. 7.44, 7.18, and 7.19 have to be generalized over the spin and band index:

$$n = \frac{2}{N_{\vec{k}} V} \sum_{n_i,\vec{k}} f_{\epsilon(n_i,\vec{k})} \quad , \tag{7.78}$$

$$\sigma_{xx} = \frac{2e^2}{3N_{\vec{k}} V} \sum_{n_i,\vec{k}} \left(-\frac{\partial f}{\partial \epsilon(n_i,\vec{k})} \right) \tau_{\epsilon(n_i,\vec{k})} v_{xx}(n_i,\vec{k}) v_{xx}(n_i,\vec{k}) \quad , \tag{7.79}$$

$$S_{xx} = \frac{1}{eT} \frac{\sum_{n_i,\vec{k}} \left(-\frac{\partial f}{\partial \epsilon(n_i,\vec{k})} \right) \left[\epsilon(n_i,\vec{k}) - \mu \right] \tau_{\epsilon(n_i,\vec{k})} v_{xx}(n_i,\vec{k}) v_{xx}(n_i,\vec{k})}{\sum_{n_i,\vec{k}} \left(-\frac{\partial f}{\partial \epsilon(n_i,\vec{k})} \right) \tau_{\epsilon(n_i,\vec{k})} v_{xx}(n_i,\vec{k}) v_{xx}(n_i,\vec{k})} \quad , \tag{7.80}$$

where n_i is the band index, and $N_{\vec{k}}$ is the number of $\vec{k}$ points chosen in the Brillouin zone. For relaxation times $\tau_{\epsilon(n_i,\vec{k})}$ we use the same energy dependence as given by the Kane model (see section 7.5). In the Eqs. 7.79, and 7.80 we have dropped the suffix $\epsilon(n_i,\vec{k})$ of

the distribution function $f_{\epsilon(n_i,\vec{k})}$.

Instead using the Eq. 7.9 for the velocities $\vec{v}(n_i,\vec{k})$, we calculate $\vec{v}(n_i,\vec{k})$ using the momentum matrix elements $\vec{p}(n_i,\vec{k})$:

$$\vec{v}(n_i,\vec{k}) = \frac{1}{m}\vec{p}(n_i,\vec{k}) = \frac{1}{m}\left\langle \psi(n_i,\vec{k})|\hat{\vec{p}}|\psi(n_i,\vec{k})\right\rangle \quad , \tag{7.81}$$

which are available in the optical properties package of WIEN2K program. [6]

7.7 Results and Discussions

7.7.1 PbTe Using Kane Model

In order to calculate electrical conductivity σ_{xx} and thermopower S_{xx} for a given concentration n at different temperatures, Eqs. 7.40, 7.43, and 7.45 have to be solved simultaneously, the common link being the chemical potential μ. We use the Mathematica program to solve these coupled equations.

As mentioned in the section 7.5 of this chapter, we have taken into account the temperature dependence of the energy gap E_g and density of states effective mass m_d which are given in Eqs. 7.75, 7.76 and 7.77. At high concentrations, $n \sim 10^{19}\text{cm}^{-3}$, which are required for a good thermoelectric, the n or p-type PbTe can be described using a single band model since at these concentrations contributions to transport comes primarily from a single type of carriers. First we give the results for n-type PbTe.

At concentration $n = 5 \times 10^{19}\text{cm}^{-3}$, using the values given in Ref. [103] for the acoustic and optical deformation potential coupling constants for the conduction band

(E_{ac}=15eV and E_{oc}=26eV), we underestimate the electrical conductivity at room temperature (Fig. 7.2a). The scattering from optical phonons is too strong. In order to fit the electrical conductivity data at room temperature we have to decrease the value of E_{oc} to 15eV (Fig. 7.2b). The results for electrical conductivity, thermopower and power factor PF=σS^2 using both sets of values for the deformation potential coupling constants are given in Fig. 7.2. Clearly, a reduced value E_{oc} gives a better fit to the high T data. After taking into account the temperature dependence of E_g and m_d we obtain excellent agreement with experiment for electrical conductivity and good agreement for thermopower.

In is interesting to explore how significant are the temperature dependence of E_g and m_d in the entire temperature range, a study which has not done before. For this we calculate σ, S and the power factor $S^2\sigma$ for a constant m_d using the values $m_l = 0.24m$ and $m_t = 0.024m$ for the longitudinal and transverse effective mass respectively. The results for both the sets of deformation potential coupling constants are given in Fig. 7.3. For constant m_d, the electrical conductivity is overestimated whereas the thermopower is underestimated. Also the temperature dependence of thermopower is not well described. Therefore the temperature dependence of m_d is very important to have a good agreement with experimental values of electrical conductivity and thermopower. It is important to note that one can have fortuitous good agreement for the power factor as shown in Fig. 7.3(e) even when σ and S are not very well reproduced individually. This suggests that in order understand correctly the temperature dependence of the power factor in PbTe systems, the temperature dependence of the electrical conductivity and thermopower have to be studied separately and understood.

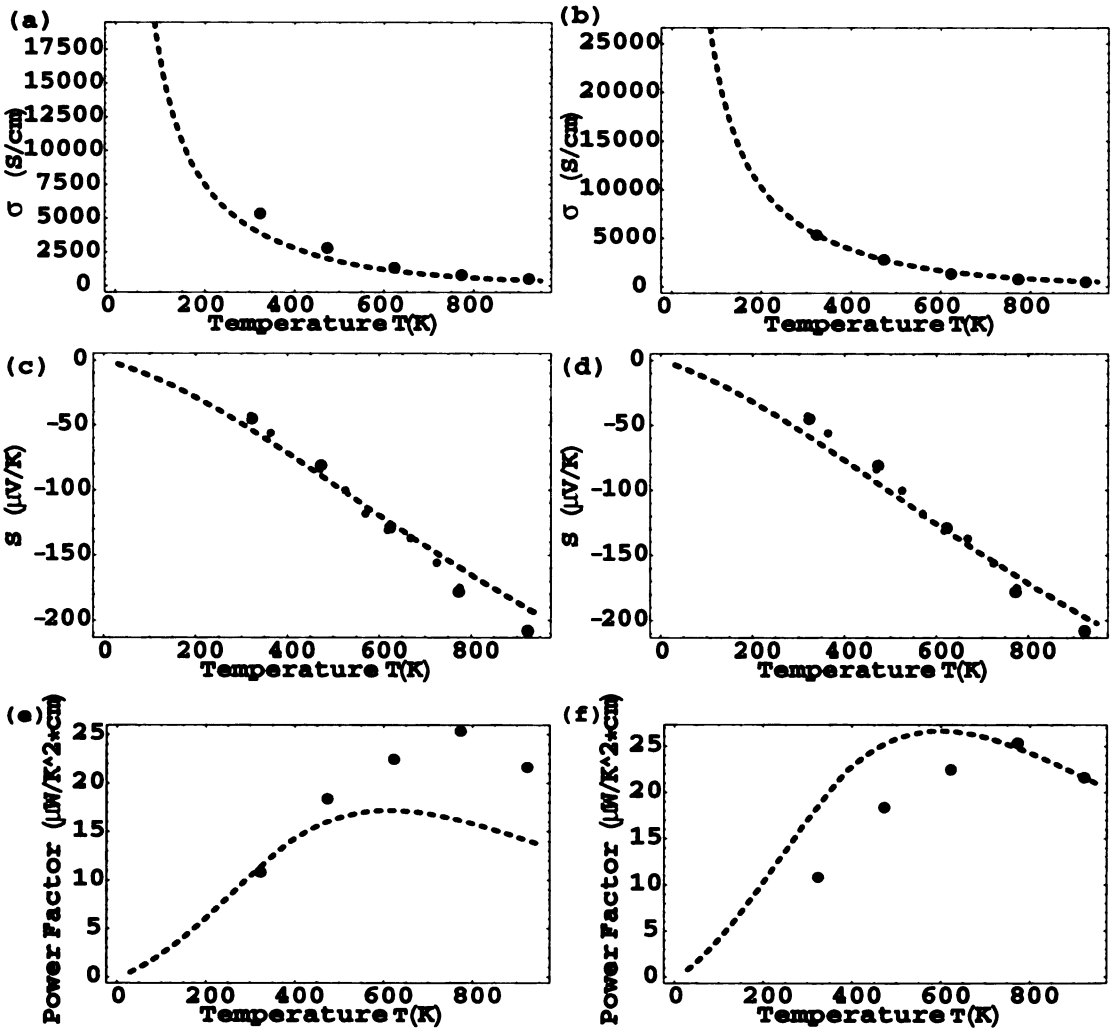

Figure 7.2: Temperature dependence of (a)Electrical conductivity, (c)Thermopower, and (e)Power factor for n-type PbTe at concentration $n = 5 \times 10^{19}\text{cm}^{-3}$ obtained using E_{ac}=15eV and E_{oc}=26eV values of the deformation potential coupling constants; Temperature dependence of (b)Electrical conductivity, (d)Thermopower, and (f)Power factor for n-type PbTe at concentration $n = 5 \times 10^{19}\text{cm}^{-3}$ using E_{ac}=15eV and E_{oc}=15eV. Theoretical values are shown as dashed lines and the experimental values are shown as black points from Ref. [16] and as gray points from Ref. [76].

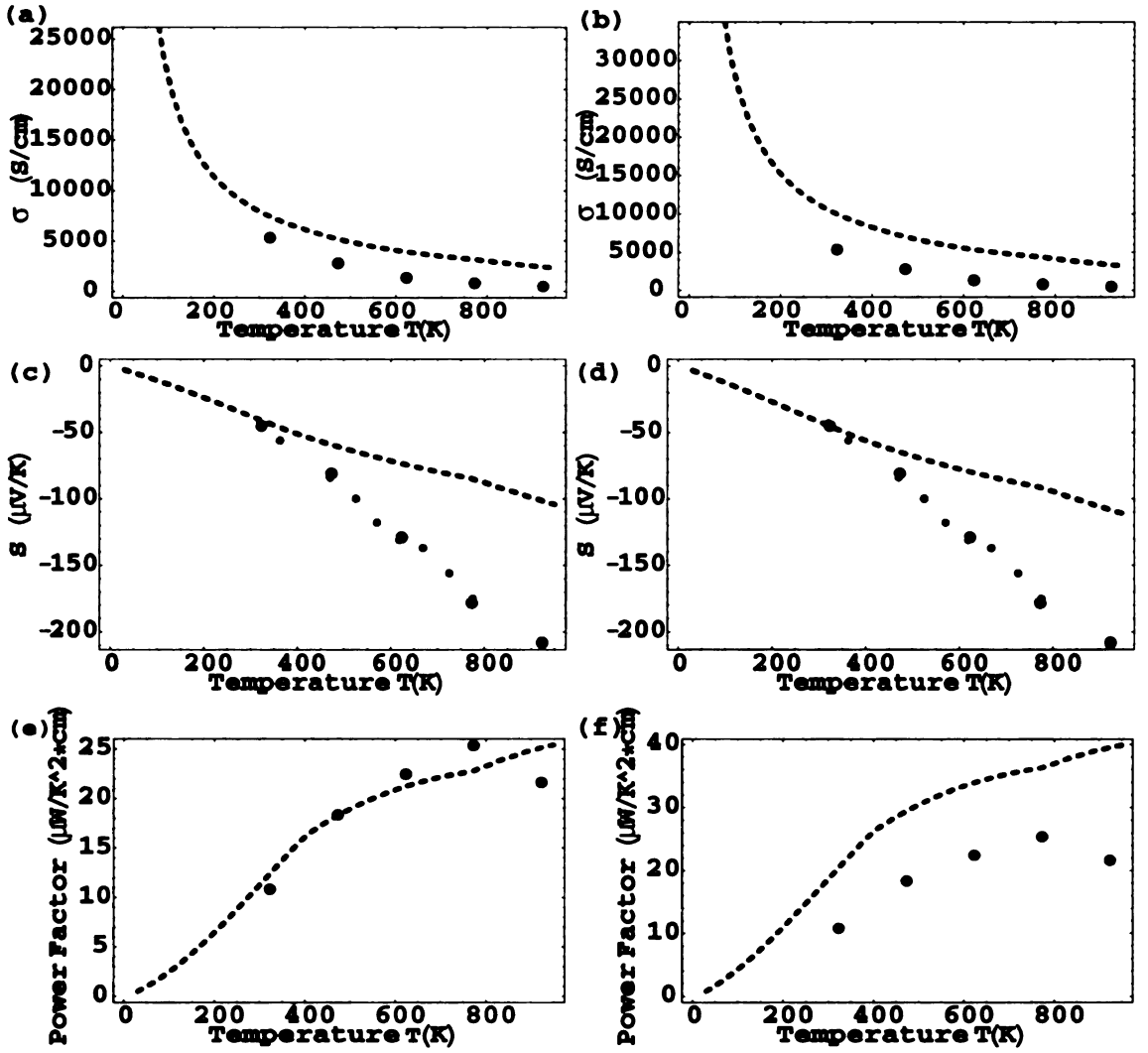

Figure 7.3: Temperature dependence of (a)Electrical conductivity, (c)Thermopower, and (e)Power factor for n-type PbTe at concentration $n = 5 \times 10^{19}\text{cm}^{-3}$ obtained using E_{ac}=15eV and E_{oc}=26eV values of the deformation potential coupling constants; Temperature dependence of (b)Electrical conductivity, (d)Thermopower, and (f)Power factor for n-type PbTe at concentration $n = 5 \times 10^{19}\text{cm}^{-3}$ using coupling constants values E_{ac}=15eV and E_{oc}=15eV. Theoretical values obtained using constant m_d are shown as dashed lines. Experimental values are shown as black points from Ref. [16] and as gray points from Ref. [76].

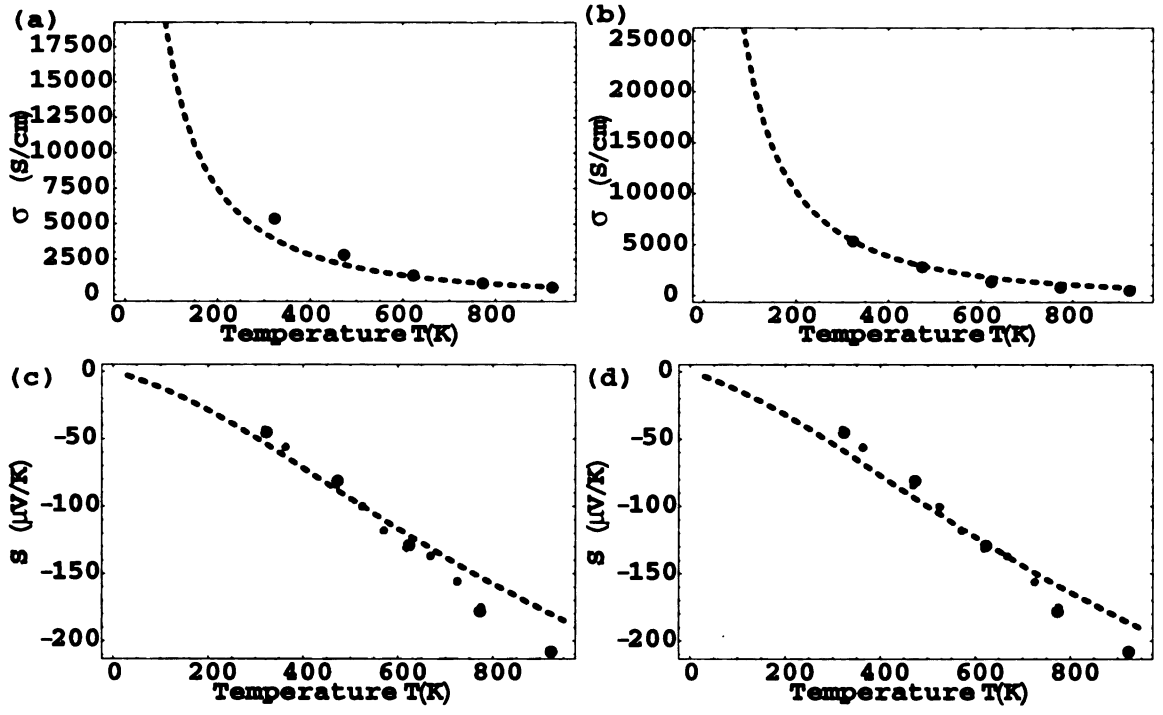

Figure 7.4: Temperature dependence of (a)Electrical conductivity, and (c)Thermopower for n-type PbTe at concentration $n = 5 \times 10^{19}\text{cm}^{-3}$ using E_{ac}=15eV and E_{oc}=26eV values of the deformation potential coupling constants; Temperature dependence of (b)Electrical conductivity, and (d)Thermopower for n-type PbTe at concentration $n = 5 \times 10^{19}\text{cm}^{-3}$ using coupling constant values E_{ac}=15eV and E_{oc}=15eV. Theoretical values obtained using temperature dependent E_g in the 0K-950K range are shown as dashed lines. Experimental values are shown as black points from Ref. [16] and as gray points from Ref. [76].

We have considered also the case where the energy gap E_g increases linearly with the temperature in the whole 0K-950K temperature range (instead of Eqs. 7.75 and 7.76). The results for the electrical conductivity and thermopower are given in Fig. 7.4. We can see that E_g temperature dependence is not very crucial to have good agreement with experiment at this high concentration, but it is important at low concentrations when carriers from the valence band can be excited into the conduction band across the band gap. For this case two band model (conduction and valence) has to be employed to calculate the transport coefficients.

To see whether the agreement between σ, S and $S^2\sigma$ and experiment obtained with

parameter values E_{ac}=15eV and E_{oc}=15eV (values chosen to match the value of σ at 300K for the concentration $n = 5 \times 10^{19}\text{cm}^{-3}$) persist at different concentrations, we have calculated these quantities at two other concentrations: $n = 2.4 \times 10^{19}\text{cm}^{-3}$ and $n = 1 \times 10^{20}\text{cm}^{-3}$. The results are shown in Fig. 7.5. For $n = 2.4 \times 10^{19}\text{cm}^{-3}$, the room temperature electrical conductivity is slightly underestimated, whereas for $n = 1 \times 10^{20}\text{cm}^{-3}$ this value is slightly overestimated. Over the entire 300K-950K temperature range the agreement for electrical conductivity with experiment is quite good, suggesting that E_{ac}=15eV and E_{oc}=15eV values of the deformation potential coupling constants describe well the scattering mechanisms in the $1 - 10 \times 10^{19}\text{cm}^{-3}$ concentration range. The thermopower is overestimated for both the concentrations; as a consequence the power factor is also overestimated.

7.7.2 PbTe Using *ab initio* Electronic Structure

In order to calculate the transport coefficients of n-type PbTe using *ab initio* density functional results the sums given in Section 7.6 were evaluated over the band index and $\vec{k}$ points. The carrier velocities were calculated using the momentum matrix elements. It was found that a very dense mesh of irreducible $\vec{k}$ points (more than 15000) have to be taken in the Brillouin zone in order to have good convergence for the values of the transport coefficients. This will require a tremendous amount of computational time and computer resources in the case of complex LAST-m systems, but for PbTe such calculations are feasible. For the relaxation time the same expressions were used as in the nonparabolic Kane model.

The calculated values for the electrical conductivity and thermopower at $n = 5 \times$

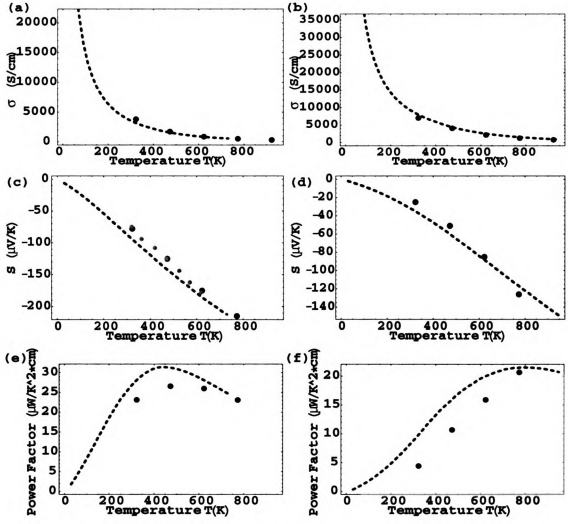

Figure 7.5: Temperature dependence of (a)Electrical conductivity, (c)Thermopower, and (e)Power factor for n-type PbTe at concentration $n = 2.4 \times 10^{19}\text{cm}^{-3}$; Temperature dependence of (b)Electrical conductivity, (d)Thermopower, and (f)Power factor for n-type PbTe at concentration $n = 10 \times 10^{19}\text{cm}^{-3}$. Theoretical values obtained using temperature dependent E_g and m_d and using E_{ac}=15eV and E_{oc}=15eV values for the deformation potential coupling constants are shown as dashed lines. Experimental values are shown as black points from Ref. [16] and as gray points from Ref. [76].

10^{19}cm^{-3} are shown in Fig. 7.6. One expects that *ab initio* energy dispersion should give better agreement with experiment as compared to the Kane model. In contrast the agreement is not as good. The electrical conductivity is overestimated (Fig. 7.6a) and the thermopower is underestimated (Fig. 7.6b). This is due to the fact that in *ab initio* calculations the temperature dependence of the density of states effective mass m_d can not be incorporated in the calculation of chemical potential using expression for concentration n (see Eqs. 7.78 and 7.45). For the same n, the *ab initio* results (Eq. 7.78) give a higher value of the chemical potential μ than that given by the Kane model (Eq. 7.45). This results in an increase in the electrical conductivity and decrease in the thermopower at a given temperature. To prove that not incorporating the temperature dependence of m_d in theoretical calculations is the reason of disagreement between the *ab initio* results and experiment, we have calculated the transport coefficients in the Kane model using constant values for m_d in the expression for concentration n (Eq. 7.45), but temperature dependent m_d in the expressions of relaxation times. These results are shown in Fig. 7.6a,b as continuous lines and they clearly show the overestimation of electrical conductivity and underestimation of thermopower. The zero temperature *ab initio* electronic structure calculations can not correctly describe the finite temperature transport coefficients in PbTe particularly when the band structure parameters such as E_g and m_d are strongly T-dependent. A finite temperature *ab initio* density functional theory is necessary to describe the transport properties of PbTe and LAST-m systems properly. Clearly this is not possible at the present time. Therefore in our transport calculations for the LAST-m systems we use only the energy dispersion given by the Kane model.

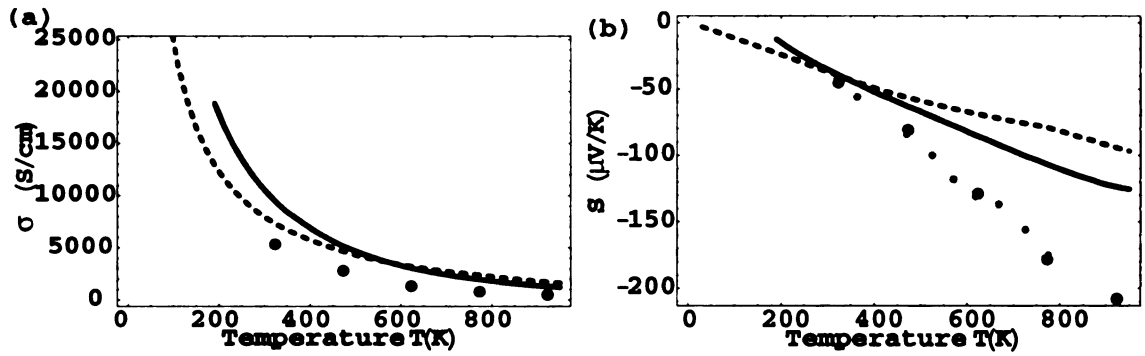

Figure 7.6: Temperature dependence of (a)Electrical conductivity and (b)Thermopower for n-type PbTe at concentration $n = 5 \times 10^{19}\text{cm}^{-3}$ and using E_{ac}=15eV and E_{oc}=15eV values of the deformation potential coupling constants. Theoretical values obtained using *ab initio* energy dispersion and temperature dependence of E_g and m_d are shown as dashed lines. Theoretical values obtained using nonparabolic Kane energy dispersion with constant m_d in the expression of n are shown as continuous lines. Experimental values are shown as black points from Ref. [16] and as gray points from Ref. [76].

7.7.3 LAST-m Using Modified Kane Model

To calculate the transport properties of LAST-m systems, we make use of the *ab initio* band structure results to construct an effective nonparabolic Kane model. Transport coefficient calculations were performed for the chain model of LAST-30 systems (Figs. 6.9d) through a qualitative analysis of the band structure results of the chain model and bulk PbTe. The band structure of PbTe and chain model in the simple cubic (sc) Brillouin zone are given in Figs. 6.15a,b. In sc Brillouin zone of PbTe, the conduction band minimum and the valence band maximum occur at the Γ point which is same as the L point in the face centered cubic (fcc) Brillouin zone. The lowest conduction band, which contributes to the transport in the fcc Brillouin zone is one-fold degenerate and the multiplicity of L point is four, whereas in sc Brillouin zone the lowest conduction band is four-fold degenerate and the multiplicity of Γ point is one.

More specifically, the lowest conduction band in sc Brillouin zone along the ΓX di-

rection is four-fold degenerate, whereas in the ΓR direction the first conduction band is one-fold degenerate and the second conduction band is three-fold degenerate. In the case of chain model these bands split and the first conduction band has mostly Sb orbital character (Fig. 6.15b). The lowest conduction band for the chain model has a flatter energy dispersion compared to PbTe. To simulate the chain model for the lowest conduction band, we have taken a heavier density of states effective mass m_d^{chain}, whereas for the other three conduction bands we have used the same m_d as for PbTe. Although we recognize that this approach can not quantitatively describe the chain model of LAST-30 systems since m_d for the other three conductions bands are not exactly the same as those of PbTe, the approach can qualitatively describe the transport properties in all LAST-m systems. This is a consequence of the electronic structure results, which show that all the Ag-Sb microstructural arrangements have an enhanced conduction band density of states (heavier m_d) near the band bottom as compared to PbTe (see subsection 6.4.3).

We have considered two values for the effective mass m_d^{chain} of the lowest conduction band. One is m_d^{chain}=1.5m_d and the other is m_d^{chain}=2.5m_d, where m_d is the density of states effective mass of PbTe. The results for concentration $n = 5 \times 10^{19}\text{cm}^{-3}$ (using E_{ac}=15eV and E_{oc}=15eV values of the deformation potential coupling constants) are given in Fig. 7.7. The chain model for m_d^{chain}=1.5m_d has a lower electrical conductivity and a higher thermopower compared to PbTe. As a result the power factor shows a small increase in the 0K-500K temperature range (Fig. 7.7a,c,e). Increasing the value of m_d^{chain} even more (m_d^{chain}=2.5m_d), the electrical conductivity of the chain model is further decreased, whereas the thermopower is increased. This gives an enhanced power factor in

the 0K-500K temperature range (Fig. 7.7b,d,f). These qualitative transport calculations show that LAST-m systems in the 0K-500K temperature range have a small increase in the power factor compared to PbTe. The enhancement of the power factor increases with the increasing m_d^{chain} values.

We have calculated the transport coefficients for a higher concentration ($n = 1 \times 10^{20}\text{cm}^{-3}$) for m_d^{chain}=2.5m_d. These results are shown in Fig 7.8. The power factor for this concentration shows an enhancement in the 0K-700K temperature range. This suggest that the temperature range for which the power factor of LAST-m systems show an enhancement relative to PbTe increases with concentration.

7.8 Summary

Transport calculations using Kane model for energy dispersion in PbTe show that the temperature dependence of the density of states effective mass m_d is very important to correctly describe the temperature dependence of the electrical conductivity and thermopower. Taking into account this temperature dependence and that of the energy band-gap, we see that the electrical conductivity has a strong T^{-3} temperature dependence (in agreement with experiment). [75]

Calculations for PbTe using *ab initio* electronic structure results for the energy dispersion overestimate the electrical conductivity and underestimate the thermopower at a given temperature. This is a consequence of the fact that in *ab initio* electronic structure results the temperature dependence of m_d can not be taken into account in the calculation of the chemical potential. This increases the chemical potential values for a given n and tem-

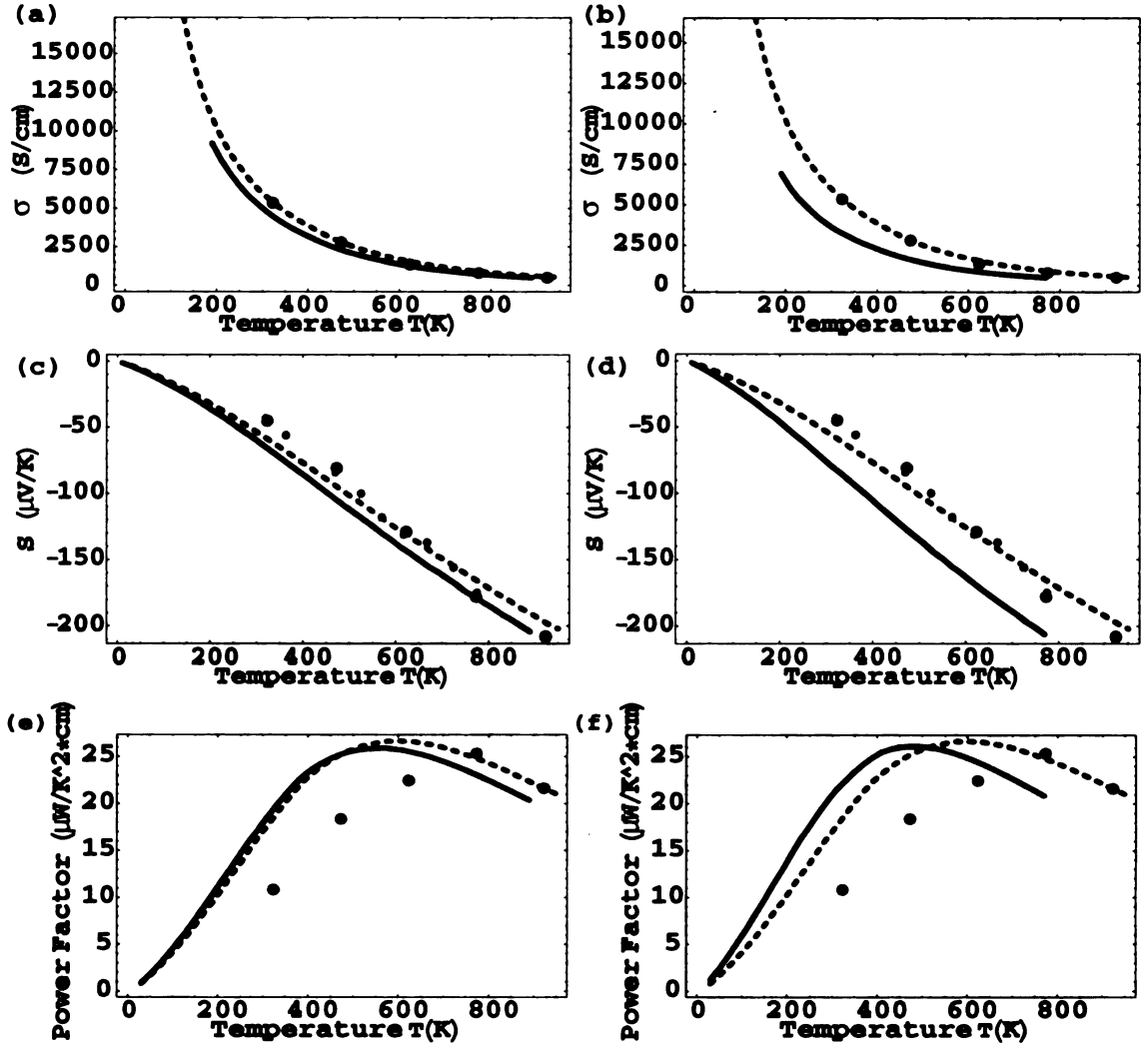

Figure 7.7: Transport coefficients at concentration $n = 5 \times 10^{19}\text{cm}^{-3}$ using temperature dependent E_g and m_d and E_{ac}=15eV and E_{oc}=15eV for the deformation potential coupling constants. Temperature dependence of (a)Electrical conductivity, (c)Thermopower, and (e)Power factor for m_d^{chain}=1.5m_d; Temperature dependence of (b)Electrical conductivity, (d)Thermopower, and (f)Power factor for m_d^{chain}=2.5m_d. Theoretical values for bulk PbTe are shown as dashed lines and for the chain model of LAST-30 as continuous lines. Experimental values are shown as black points from Ref. [16] and as gray points from Ref. [76].

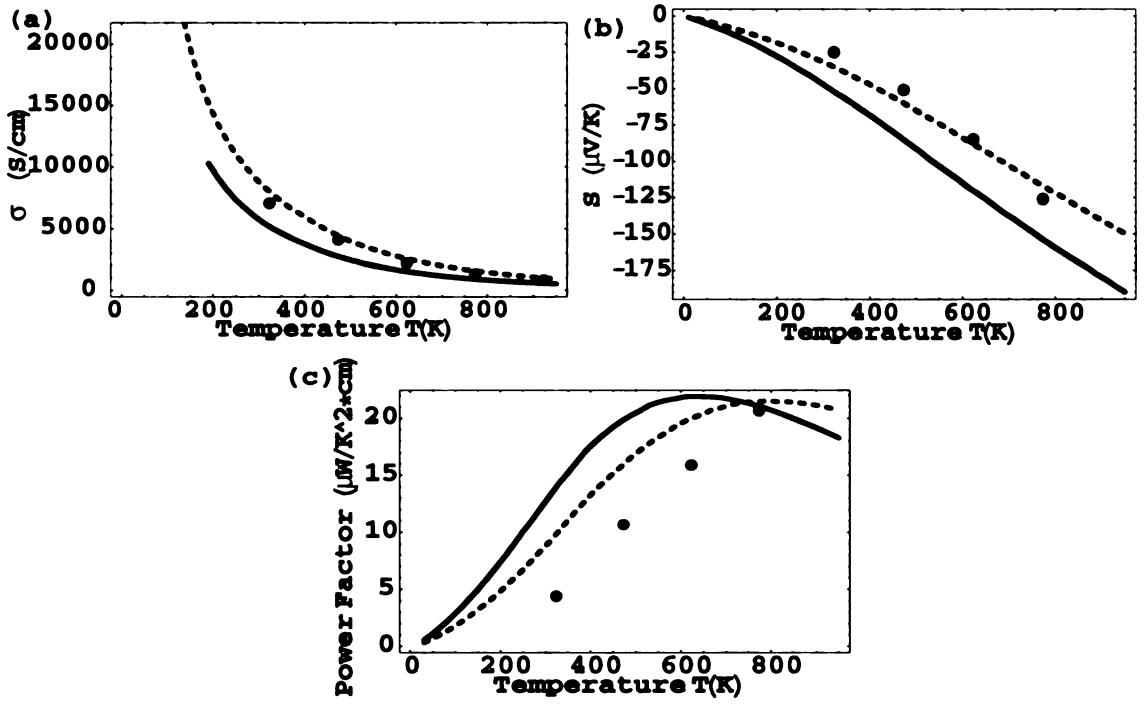

Figure 7.8: Transport coefficients at concentration $n = 1 \times 10^{20}\text{cm}^{-3}$ using temperature dependent E_g and m_d and E_{ac}=15eV and E_{oc}=15eV values of the deformation potential coupling constants. Temperature dependence of (a)Electrical conductivity, (c)Thermopower, and (e)Power factor for m_d^{chain}=2.5m_d. Theoretical values for bulk PbTe are shown as dashed lines and for the chain model of LAST-30 as continuous lines. Experimental values are shown as black points from Ref. [16] and as gray points from Ref. [76].

perature. This effect enhances the electrical conductivity and reduces the thermopower. Therefore, the zero temperature *ab initio* density functional theory (DFT) can not describe correctly the transport properties in PbTe when m_d and E_g are known to depend strongly on T. This may also be true for the LAST-m materials. A finite temperature DFT is necessary to capture the correct electronic transport in PbTe and related materials.

The qualitative transport calculations for LAST-m systems (chain model of LAST-30) show a small enhancement of the power factor relative to PbTe. This enhancement increases with increasing m_d values. The temperature range, for which this enhancement of the power factor is achieved, increases with increasing n.

The transport calculations reveal that the enhanced density of states (enhanced m_d) near the band gap of LAST-m systems as compared to that of PbTe seen in the electronic structure calculations can give rise to an increase in the power factor. However this increase is not large enough to increase *ZT* by a factor of 2 (as seen experimentally). Therefore, the reason why LAST-m systems have better *ZT* compared to PbTe is a combination of a small enhancement in the power factor and perhaps a strong reduction in the phonon thermal conductivity due to the formation of microstructures (seen in electron microscopy). [72]

Chapter 8

General Summary and Future Directions for Research

Electronic structure calculations reveal that the effect of quantum confinement QC resulting from surfaces on the electronic structure of binary layered Bi_2Se_3 and Bi_2Te_3 is the appearance of surface states. Our calculations clearly show the presence of finite in-gap surface states and a suppression of the top valence band antibonding states. These surface effects are a consequence of the strong influence of the interlayer bonding on the bulk electronic structure of these compounds, showing an important covalent contribution to the interlayer bonding besides the Van der Waals contribution. Our calculations are in very good agreement with scanning tunneling spectroscopy (STS) results. [95]

Electronic structure results in $(Bi_2Te_3)_m(Sb_2Te_3)_n$ superlattices (SL) show that the formation of SL give rise to a small increase in the electronic contribution to the figure of merit ZT as compared to bulk Bi_2Te_3 and Sb_2Te_3. The calculated values of the hole

mobility ratio μ_{cp}/μ_{ip} in the SL are in good agreement with the experimental values. [98] Our calculations show that the hole mobility ratio is very sensitive to the different types of SL, whereas the electron mobility ratio is less sensitive. This suggests that the valence band can be engineered through $(Bi_2Te_3)_m(Sb_2Te_3)_n$ SL structures.

Electronic structure calculations of complex ternary $K_2Bi_8Se_{13}$ system show that its electronic structure and consequently the thermoelectric properties are very sensitive to the difference in the two crystal structures $\alpha-K_2Bi_8Se_{13}$ and $\beta-K_2Bi_8Se_{13}$ of this system. $\alpha-K_2Bi_8Se_{13}$ has no structural disorder, whereas $\beta-K_2Bi_8Se_{13}$ has two sites with K/Bi mixed occupancy. While $\alpha-K_2Bi_8Se_{13}$ is an indirect band gap semiconductor, $\beta-K_2Bi_8Se_{13}$ shows semimetallic or semiconductor behavior. In $\beta-K_2Bi_8Se_{13}$ the atoms at the mixed sites are found to be very important in determining the electronic properties of this material. When the mixed sites are treated as fully occupied by K or Bi atoms the system is a semimetal. Incorporation of mixed occupancy results in an indirect gap semiconductor. Both phases of $K_2Bi_8Se_{13}$ have low symmetry where one tries to achieve high anisotropy $R=[\lambda_{zz}/(\lambda_{xx}\lambda_{yy})]^{1/2}$ ratios involving the effective mass parameters λ_{ij} (see Chapter 1). Effective mass calculations show that $\beta-K_2Bi_8Se_{13}$ has large R values compared to $\alpha-K_2Bi_8Se_{13}$. The high R values in $\beta-K_2Bi_8Se_{13}$ combined with a low value of the phonon thermal conductivity (due to K/Bi disorder) make $\beta-K_2Bi_8Se_{13}$ an excellent candidate for room and high temperature thermoelectric material.

Electronic structure results of the complex quaternary LAST-m systems reveal that their electronic structure is very sensitive to the Ag-Sb microstructural arrangements. The common feature of all these arrangements is that they have a more enhanced density of states

(DOS) near the gap as compared to PbTe. This feature is desirable because it could enhance the *ZT*. Transport calculations using nonparabolic Kane model for energy dispersion in bulk PbTe show that the temperature dependence of the density of states effective mass m_d is very important to have good agreement with experiment for electrical conductivity σ and thermopower S. The calculations for PbTe using *ab initio* electronic structure results for the energy dispersion overestimate σ and underestimate S at a given temperature. This is a consequence of the fact that in *ab initio* electronic structure results the temperature dependence of m_d can not be taken into account. Transport calculations for LAST-m systems show a small enhancement of the power factor relative to PbTe is possible. Although increase in the DOS can enhance the thermopower S, it tends to reduce electrical conductivity σ. However, the net effect is a small increase in the power factor. Therefore, we believe that the major contribution to the enhanced *ZT* of LAST-m systems compared to PbTe comes from a strong reduction in the phonon thermal conductivity due to the formation of microstructures (as seen in transmission electron microscopy). [72]

Electronic structure calculations within density functional theory (DFT) offer varieties of tools to determine the stability of compounds, their atomic geometries, their band structure and transport properties. Within DFT the stability of compounds (their total energies) are well predicted. Therefore, the theory can indeed help in predicting new compounds with new electronic properties. One can use these calculations not only to understand why already synthesized good thermoelectric materials show these properties, but also to search for new potential thermoelectric materials. In order to characterize the thermoelectric properties of a material, transport calculations for σ, S, and κ have to be performed.

Unfortunately, to perform such calculations one has to make approximations whose validity is not fully under control. By this it is meant that we do not have an estimate of the magnitude of the made errors. Such an approximation is the rigid band model, where the electronic band structure of doped semiconductors (requirement for a good thermoelectric) is assumed to be the same as for undoped semiconductors. Another approximation is to assume that the electronic band structure at finite temperature is the same as that at 0K. In this thesis, we show that this approximation can not be made for PbTe and LAST-m compounds and particularly for compounds with strong electron-phonon coupling. For such systems finite temperature DFT calculations are required. The other approximation is the relaxation time approximation made in describing the electronic scattering mechanisms. Future calculations of transport coefficients should improve upon this. Finally, we mention the problem of LDA/GGA in underestimating the gap band. [2] For small band gap semiconductors, which most good thermoelectrics are, this could be a problem in calculating the transport coefficients. Although methods like GW approximation have been developed in recent years, their applications to study the transport properties of complex materials is still in its infancy. One expects considerable theoretical effort to be put in this direction in the future. Therefore, we believe that for understanding transport properties of complex systems a very close interaction between theory and experiment is necessary.

BIBLIOGRAPHY

Bibliography

[1] E.A. Albanesi, C.M.I. Okoye, C.O. Rodriguez, E.L.P.Y. Blanca, and A.G. Petukhov. *Phys. Rev. B*, 61:16589, 2000.

[2] W.G. Aulbur, L. Jonsson, and J.W. Wilkins. *Solid State Physics*, volume 54. Academic Press, Orlando, 2000.

[3] R.F.W. Bader. *Atoms in Molecules - A Quantum Theory*. Oxford University Press, 1990.

[4] G. Binnig and H. Rohrer. *IBM J. Res. Develop.*, 30:355, 1986.

[5] J. Black and E.M. Conwell. *J. Phys. Chem. Solids*, 2:240, 1957.

[6] P. Blaha, K. Schwarz, and J. Luitz. *WIEN2K, An Augmented Plane Wave + Local Orbitals Program for Calculating Crystal Properties*. Karlheinz Schwarz, Techn. Universitat Wien, Austria, 2001.

[7] N.P. Blake, S. Latturner, J.D. Bryan, G.D. Stucky, and H. Metiu. *J. Chem. Phys.*, 115:8060, 2001.

[8] N.P. Blake and H. Metiu. *Chemistry, Physics and Materials Science of Thermoelectric Materials: Beyond Bismuth Telluride*. Kluwer Academic/Plenum Publishers, 2003.

[9] D.Y. Chung, K.S. Choi, L. Iordanidis, J.L. Schindler, P.W. Brazis, C.R. Kannewurf, B. Chen, S. Hu, C. Uher, and M.G. Kanatzidis. *Chem. Mater.*, 9:3060, 1997.

[10] D.Y. Chung, T. Hogan, P. Brazis, M. Rocci-Lane, C. Kannewurf, M. Bastea, C. Uher, and M.G. Kanatzidis. *Science*, 287:1024, 2000.

[11] D.Y. Chung, S. Jobic, T. Hogan, C.R. Kannewurf, R. Brec, J. Rouxel, and M.G. Kanatzidis. *J. Am. Chem. Soc.*, 119:2505, 1997.

[12] R.T. Delves, A.E. Bowley, D.W. Hazelden, and H.J. Goldsmid. *Proc. Phys. Soc.*, 78:838, 1961.

[13] F.J. Disalvo. *Science*, 285:703, 1999.

[14] M.S. Dresselhaus, Y.-M. Lui, O. Rabin, M.R. Black, S.B. Cronin, and G. Dresselhaus. *Chemistry, Physics and Materials Science of Thermoelectric Materials: Beyond Bismuth Telluride*. Kluwer Academic/Plenum Publishers, 2003.

[15] R. Dronskowski and P.E. Blochl. *J. Phys. Chem.*, 97:8617, 1993.

[16] B.A. Efimova, L.A. Kolomoets, Yu.I. Ravich, and T.S Stavitskaya. *Soviet Physics - Semiconductors*, 4:1653, 1971.

[17] S.N. Elsayed, A. Abdelghany, A.H. Abouelela, and N.H. Mousa. *Physics and Chemistry of Liquids*, 28:165, 1994.

[18] H. Eschrig, G. Seifert, and P. Ziesche. *Solid State Commun.*, 56:777, 1985.

[19] J.P. Fleurial *et. al. Proc. 15th Int. Conf. on Thermoelectrics*. IEEE, Piscataway, NJ, 1996.

[20] D.M. Freik, L.I. Nykyruy, and V.M. Shperun. *Semiconductor Physics, Quantum Electronics and Optoelectronics*, 5:362, 2002.

[21] S. Geller and J.H. Wernick. *Acta Cryst*, 12:46, 1959.

[22] D.K. Gochev, S.K. Decheva, and S.K. Dimitrov. *Dokladina Bolgarskata Akademiyana Naukite*, 26:619, 1973.

[23] K. Gofron, J.C. Campuzano, A.A. Abrikosov, M. Lindroos, A. Bansil, H. Ding, D. Koelling, and B. Dabrowski. *Phys. Rev. Lett.*, 73:3302, 1994.

[24] A. Gonis. *Theoretical Material Science*. Material Research Society, 2000.

[25] T. C. Harman, P.J. Taylor, D.L. Spears, and M.P. Walsh. *Proc. 18th Int. Conf. on Thermoelectrics*. IEEE, Piscataway, NJ, 1999.

[26] T.C. Harman, P.J. Taylor, M.P. Walsh, and B.E. LaForge. *Science*, 297:2229, 2002.

[27] D. Hicks and M.S. Dresselhaus. *Phys. Rev. B*, 47:12727, 1993.

[28] L.D. Hicks, T.C. Harman, and M.S. Dresselhaus. *Appl. Phys. Lett.*, 63:3230, 1993.

[29] P. Hohenberg and W. Kohn. *Phys. Rev.*, 136:B864, 1964.

[30] K.F. Hsu, S. Loo, F. Guo, W. Chen, J.S. Dyck, C. Uher, T. Hogan, E.K. Polychroniadis, and M.G. Kanatzidis. *Science*, 303:818, 2004.

[31] L.D. Ivanova, Yu.V. Granatkina, and Yu.A. Sidorov. *Inorg. Mater.*, 35:34, 1999.

[32] H. Jansen. *Phys. Rev. B*, 7:1912, 1988.

[33] A.F. Joffe. *Scientific. American*, 199:31, 1958.

[34] R. O. Jones and O. Gunnarsson. *Rev. Mod. Phys.*, 61:689, 1989.

[35] M.G. Kanatzidis. *Semiconductors and Semimetals*, 69:51, 2001.

[36] M.G. Kanatzidis. *Chemistry, Physics and Materials Science of Thermoelectric Materials: Beyond Bismuth Telluride*. Kluwer Academic/Plenum Publishers, 2003.

[37] A. Klein, S. Tiefenbacher, V. Eyert, C. Pettenkofer, and W. Jaegerman. *Phys. Rev. B*, 64:205416, 2001.

[38] D.D. Koelling and B.J. Harmon. *J. Phys. C*, 10:3107, 1977.

[39] H. Kohler. *Phys. Status Solidi B*, 73:95, 1976.

[40] H. Kohler. *Phys. Status Solidi B*, 74:591, 1976.

[41] W. Kohn. *Solid State Physics*, volume 5. New York, Academic, 1957.

[42] W. Kohn and L.J. Sham. *Phys. Rev.*, 140:A1133, 1965.

[43] J. Kubler and V. Eyert. *Electronic structure calculations, in: Electronic and Magnetic Properties of Metals and Ceramics*, volume 3A. VCH Verlagsgesellschaft, Weinheim, 1992.

[44] V.A. Kutasov, T.E. Svechnikova, and S.N. Chizhevskaya. *Fiz. Tverd. Tela*, 29:3008, 1987.

[45] T. Kyratsi, J.S. Dyck, W. Chen, D.Y. Chung, C. Uher, K.M. Paraskevopoulos, and M.G. Kanatzidis. *J. Appl. Phys.*, 92:965, 2002.

[46] M. Lach-hab, M. Keegan, D.A. Papaconstantopoulos, and M.J. Mehl. *J. Phys. Chem. Sol.*, 61:1639, 2000.

[47] M. Lach-hab, D.A. Papaconstantopoulos, and M.J. Mehl. *J. Phys. Chem. Sol.*, 63:833, 2002.

[48] P. Larson. *Phys. Rev. B*, 68:155121, 2003.

[49] P. Larson, V.A. Greanya, W.C. Tonjes, R. Liu, S.D. Mahanti, and C.G. Olson. *Phys. Rev. B*, 65:085108, 2002.

[50] P. Larson, S.D. Mahanti, and M.G. Kanatzidis. *Phys. Rev. B*, 61:8162, 2000.

[51] P. Larson, S.D. Mahanti, and M.G. Kanatzidis. *Phys. Rev. B*, 65:045205, 2002.

[52] P. Larson, S.D. Mahanti, S. Sportouch, and M.G. Kanatzidis. *Phys. Rev. B*, 59:15660, 1999.

[53] C.S. Lent, M.A. Bowen, J.D. Dow, R.S. Allgaiger, O.F. Sankey, and E.S. Ho. *Sol. State Commun.*, 61:83, 1987.

[54] A.H. MacDonald, W.E. Pickett, and D.D. Koelling. *J. Phys. C*, 13:2675, 1978.

[55] A.H. MacDonald and S.H. Vosko. *J. Phys. C: Solid State Phys.*, 12:2977, 1979.

[56] G. Mahan, B. Sales, and J. Sharp. *Phys. Today*, 50:42, 1997.

[57] G.D. Mahan. *Solid State Physics*, volume 51. Academic Press, Orlando, 1998.

[58] G.D. Mahan and J.O. Sofo. *Proc. Natl. Acad. Sci.*, 93:7436, 1996.

[59] S.D. Mahanti, P. Larson, D. Bilc, and H. Li. *Chemistry, Physics and Materials Science of Thermoelectric Materials: Beyond Bismuth Telluride.* Kluwer Academic/Plenum Publishers, 2003.

[60] G. Martinez, M. Schluter, and M.L. Cohen. *Phys. Rev. B*, 11:651, 1975.

[61] T.G. Mccarthy, S.P. Ngeyi, J.H. Liao, D.C. Degroot, T. Hogan, C.R. Kannewurf, and M.G. Kanatzidis. *Chem. Mater.*, 5:331, 1993.

[62] S.K. Mishra, S Satpathy, and O Jepsen. *J. Phys. Cond. Matt.*, 9:461, 1997.

[63] A. Mookerjee. *Electronic Structure of Alloys, Surfaces and Clusters.* Taylor and Francis, 2003.

[64] Y. Noda, K. Mizuno, Y.S. Kang, M. Niino, and I.A. Nishida. *J Japan Inst. Metals*, 63:1448, 1999.

[65] L. Nordstrom and D.J. Singh. *Phys. Rev. B*, 53:1103, 1996.

[66] J. Olivierfourcade, P.E. Lippens, J.C. Jumas, M. Womes, I. Lefebvre, M. Lanno, J.M. Esteva, and R. Karnatak. *European J. Sol. Stat. Inorg. Chem.*, 30:139, 1993.

[67] H. Overhof and U. Sossler. *Phys. Stat. Sol.*, 37:691, 1970.

[68] S.T. Pantelides. *Rev. Mod. Phys.*, 50:797, 1978.

[69] S.T. Pantelides. *Deep Centers in Semiconductors.* 2nd ed. Gordon and Breach, Yverdon, Switzerland, 1992.

[70] J.P. Perdew, K. Burke, and M. Ernzerhof. *Phys. Rev. Lett.*, 77:3865, 1996.

[71] J.P. Perdew and Y. Wang. *Phys. Rev. B*, 45:13244, 1992.

[72] E. Quarez, K.F. Hsu, R. Pcionek, N. Frangis, E.K. Polychroniadis, and M.G. Kanatzidis. *accepted to JACS*, 2005.

[73] A.K. Rajagopal. *J. of Phys. C*, 11:L943, 1978.

[74] A.K. Rajagopal and J. Callaway. *Phys. Rev. B*, 7:1912, 1973.

[75] Yu.I. Ravich, B.A. Efimova, and I.A. Smirnov. *Semiconducting Lead Chalcogenides*, volume 5. Plenum Press, New York-London, 1970.

[76] Yu.I. Ravich, B.A. Efimova, and V.I. Tamarchenko. *Phys. Status Solidi B*, 43:453, 1971.

[77] Yu.I. Ravich, B.A. Efimova, and V.I. Tamarchenko. *Phys. Status Solidi B*, 43:11, 1971.

[78] M. Richter. *J. Phys. D: Appl. Phys.*, 31:1017, 1998.

[79] M. Sahnoun, C. Daul, M. Driz, J.C. Parlebas, and C. Demangeat. *Computational Materials Science*, 33:175, 2005.

[80] J.J. Sakurai. *Advanced Quantum Mechanics*. Addision Wesley, 1967.

[81] T.J. Scheidemantel, C. Ambrosch-Draxl, T. Thonhauser, J.V. Badding, and J.O. Sofo. *Phys. Rev. B*, 68:125210, 2003.

[82] J.C. Shaffer, B. Vanpelt, C. Wood, J. Freeouf, K. Murase, and J.W. Osmun. *Phys. Stat. Sol. B*, 54:511, 1972.

[83] K.I. Shimizu, Y. Nisida, and S.I. Narita. *J. Phys. Soc. Japan*, 46:1797, 1979.

[84] B. Shoeder, A. Von Middendorff, H. Kohler, and G. Landwehr. *Phys. Status Solidi B*, 59:561, 1973.

[85] D. Singh. *Planewaves, Pseudopotentials, and the LAPW method*. Kluwer Academic, Boston, 1994.

[86] G.A. Slack and M.S. Dresselhaus. *Solid State Phys.*, 34:1, 1979.

[87] J.O. Sofo and G.D. Mahan. *Phys. Rev. B*, 58:15620, 1998.

[88] C. Stampfl and A.J. Freeman. *Phys. Rev. B*, 71:024111, 2005.

[89] W.E. Tennant. *Solid State Commun.*, 20:613, 1976.

[90] J. Tersoff and D.R. Hamann. *Phys. Rev. Lett.*, 50:1998, 1983.

[91] G.A. Thomas, D.H. Rapke, R.B. Van Dover, L.F. Mattheis, W.A. Surden, L.F. Schneemaper, and J.V. Waszczak. *Phys. Rev. B*, 46:1553, 1992.

[92] T. Thonhauser, T.J. Scheidemantel, J.O. Sofo, J.V. Badding, and G.D. Mahan. *Phys. Rev. B*, 68:085201, 2003.

[93] T.M. Tritt. *Science*, 272:1276, 1996.

[94] Y.W. Tsang and M.L. Cohen. *Phys. Rev. B*, 3:1254, 1971.

[95] S. Urazhdin, D. Bilc, S.D. Mahanti, and S.H. Tessmer. *Phys. Rev. B*, 69:085313, 2004.

[96] S. Urazhdin, D. Bilc, S.H. Tessmer, S.D. Mahanti, T. Kyratsi, and M.G. Kanatzidis. *Phys. Rev. B*, 66:161306(R), 2002.

[97] J.A. Valdivia and G.E. Barberis. *J. Phys. Chem. Sol.*, 56:1141, 1995.

[98] R. Venkatasubramanian, E. Siivola, T. Colpitts, and B. O'Quinn. *Nature*, 413:597, 2001.

[99] S.H. Wei and A. Zunger. *Phys. Rev. B*, 55:13605, 1997.

[100] R.G. Wyckoff. *Crystal Structures*, volume 2. John Wiley and Sons, New York, 1967.

[101] H. Yokoi, S. Takeyama, and N. Miura. *Phys. Rev. B*, 44:6519, 1991.

[102] S.J. Youn and A.J. Freeman. *Phys. Rev. B*, 63:085112, 2001.

[103] D.M. Zayachuk. *Semiconductors*, 31:173, 1997.

[104] J.M. Ziman. *Principles of The Theory of Solids*. Cambridge University Press, 1964.